

FEDERAL UNIVERSITY OF SÃO CARLOS  
EXACT AND TECHNOLOGY SCIENCES CENTER  
GRADUATE PROGRAM IN CHEMICAL ENGINEERING

KAMILLA MALVERDI BARCELOS

**DEVELOPMENT OF STABLE AND HIGH-PERFORMANCE POLYANILINE  
ACTIVATED CARBON ELECTRODES FOR CAPACITIVE DEIONIZATION  
DESALINATION**

SÃO CARLOS

2021

KAMILLA MALVERDI BARCELOS

**DEVELOPMENT OF STABLE AND HIGH-PERFORMANCE POLYANILINE  
ACTIVATED CARBON ELECTRODES FOR CAPACITIVE DEIONIZATION  
DESALINATION**

Ph.D. thesis presented to the Graduation Program in Chemical Engineering of the Federal University of São Carlos as part of the requirements to obtain the title of Ph.D. in Chemical Engineering, in the field of Research and Development of Chemical Processes.

Advisor: Prof. Dr. Luís Augusto Martins Ruotolo

SÃO CARLOS

2021

Barcelos, Kamilla Malverdi

Development of stable and high-performance polyaniline activated carbon electrodes for capacitive deionization desalination / Kamilla Malverdi Barcelos -- 2021.  
108f.

Tese de Doutorado - Universidade Federal de São Carlos,  
campus São Carlos, São Carlos

Orientador (a): Luís Augusto Martins Ruotolo

Banca Examinadora: Luís Augusto Martins Ruotolo,  
Ernesto Antonio Urquieta Gonzalez, Elisane Longhinotti,  
Alessandra Pereira da Silva, Nerilso Bocchi

Bibliografia

1. Deionização capacitiva . 2. Dessalinização da água. 3.  
Carvão ativado de polianilina . I. Barcelos, Kamilla  
Malverdi. II. Título.

Ficha catalográfica desenvolvida pela Secretaria Geral de Informática  
(SIn)

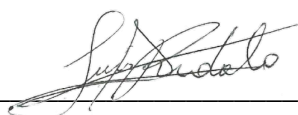
DADOS FORNECIDOS PELO AUTOR

Bibliotecário responsável: Ronildo Santos Prado - CRB/8 7325

UNIVERSIDADE FEDERAL DE SÃO CARLOS  
Centro de Ciências Exatas e de Tecnologia  
Programa de Pós-Graduação em Engenharia Química

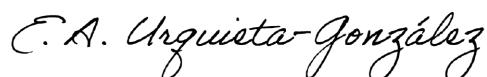
**Folha de aprovação**

Assinatura dos membros da comissão examinadora que avaliou e aprovou a Defesa de Doutorado da candidata Kamilla Malverdi Barcelos, realizada em 19/04/2021:



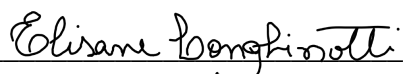
---

Prof. Dr. Luís Augusto Martins Ruotolo  
Orientador, UFSCar



---

Prof. Dr. Ernesto Antonio Urquieta Gonzalez  
UFSCar



---

Profa. Dra. Elisane Longhinotti  
UFC



---

Profa. Dra. Alessandra Pereira da Silva  
UNIFESP



---

Prof. Dr. Nerilso Bocchi  
UFSCar

*I dedicate this work to God for always assisting me, also to my parents Carlito Botazini Barcelos and Marta Malverdi Barcelos, and brother Carlito Botazini Barcelos Filho, for their love and support. You were essential for this achievement.*

## ACKNOWLEDGEMENT

First and foremost, I would like to thank the Federal University of São Carlos (UFSCar) and the Chemical Engineering Department (DEQ) for the opportunity to complete an excellent graduate program. The financial support of the Coordination for the Improvement of Higher Education Personnel (CAPES) was also essential for the realization of this work.

I am grateful to Prof. Dr. Adonay Rodrigues Loiola, Prof. Dr. Rogério Aparecido Davoglio, Prof. Dr. Ernesto Antonio Urquieta Gonzalez, Prof. Dr. Nerilso Bocchi, Prof<sup>a</sup>. Dr<sup>a</sup>. Elisane Longhinotti, and Prof<sup>a</sup>. Dr<sup>a</sup>. Alessandra Pereira da Silva for accepting to be members of my qualification and defense committees. Their contributions are insightful for the conclusion of this work.

I also wish to express my gratitude to the knowledge taught by my professors, especially the guidance, dedication, patience, and help provided by my advisor Prof. Dr. Luís A. M. Ruotolo over these past four years. Their immense knowledge and plentiful experience have contributed to the improvement of the project.

I wish to acknowledge the help provided by the technical and support staff of the DEQ. In addition, the analyzes performed by Jéssica A. Oliveira at Embrapa Instrumentation are appreciated.

I gratefully acknowledge my friends from the Laboratory for Environmental Technologies (LATEA), for their constant support, valuable discussions, advices, friendship, and “coffee times”.

I wish to express my deepest gratitude to my family, especially my parents Carlito B. Barcelos and Marta M. Barcelos, and brother Carlito B. Barcelos Filho, for all support, dedication, and prayers.

Finally, I am grateful to the Lord for everything and to all those who directly or indirectly assisted me to complete this work.

## RESUMO

A deionização capacitiva (DIC) surgiu como uma alternativa econômica para a dessalinização de água salobra (concentração de sal menor que  $10 \text{ g L}^{-1}$ ). Nos últimos anos, tem-se observado um avanço significativo em materiais de eletrodos em termos da capacidade de adsorção de sal (CAS) e eficiência de carga ( $Q_E$ ). No entanto, questões desafiadoras relacionadas à melhoria da cinética e estabilidade dos eletrodos em operações de longo prazo ainda persistem. Neste sentido, o principal objetivo desta tese foi o desenvolvimento de eletrodos estáveis de carvão ativado de polianilina (PAni) (PAC), com cinéticas de eletrossorção e dessorção otimizadas.

A comparação entre eletrodos *blade-casting* (DB) e *free-standing* (FS) de PAC dopado com p-toluenossulfonato (PAC/PTS) evidenciou os efeitos da porosidade interpartícula e da espessura dos filmes sobre as suas propriedades texturais e eletroquímicas e possibilitou entender como o ajuste da técnica de preparação dos eletrodos pode melhorar seus desempenhos na dessalinização, principalmente em termos das cinéticas de adsorção/dessorção. Embora os diferentes eletrodos apresentem desempenho semelhante em termos da capacidade de adsorção de sal gravimétrica, os eletrodos FS superam os DB em termos da capacidade de adsorção de sal volumétrica. Os filmes de carbono FS são mais compactos, sendo assim há uma maior quantidade de material eletroativo disponível para adsorção de sal. Portanto, se o custo do material não for uma restrição, a máxima quantidade de sal pode ser removida ao se utilizar células de dessalinização compactas construídas com eletrodo FS. Por outro lado, quando as cinéticas de eletrossorção e dessorção foram consideradas, o eletrodo DB apresentou desempenho superior, principalmente devido à sua maior porosidade interpartícula, a qual minimiza a distância de difusão iônica da solução *bulk* para a superfície interna, facilitando assim o acesso dos íons aos microporos. Esses resultados demonstraram que a cinética mais rápida proporcionada pela transferência de massa facilitada em filmes finos com alta porosidade interpartícula pode ser decisiva para a seleção do melhor eletrodo em aplicações de DIC, especialmente visando futuras aplicações em células de dessalinização *flow-through*.

Na sequência, diferentes estratégias foram estudadas com o objetivo de otimizar o desempenho e a estabilidade operacional a longo prazo dos eletrodos PAC/PTS. Adicionalmente, um novo carvão ativado de PAni dopado com sulfato (PAC/S) foi proposto para investigar a influência das diferentes propriedades químicas e texturais dos materiais sobre a estabilidade do eletrodo na dessalinização. Tratamentos químicos com etilenodiamina e (3-aminopropil) trietoxissilano foram utilizados para modificar os grupos superficiais químicos dos PACs e deslocar seus potenciais de carga zero ( $E_{PZC}$ ) para valores mais negativos e assim promover a assimetria entre os eletrodos. Ademais, as configurações simétricas e de DIC com membrana (MDIC) foram investigadas para comparação de desempenho. O controle da distribuição de potencial em células assimétricas foi

apontado como uma estratégia eficaz para suprimir as reações de oxidação do carbono, que são responsáveis pela queda na CAS, e melhorar a estabilidade a longo prazo. No entanto, o melhor desempenho foi alcançado com eletrodos PAC/PTS em uma configuração MDIC. Assim, o uso de membranas de troca iônica (MTI) em células de DIC provou ser um método viável para melhorar a capacidade de eletrossorção pela redução do efeito da expulsão de co-íons, além de inibir as reações faradáicas através da diminuição do transporte de espécies eletroquimicamente ativas através das MTI. Para essa configuração de célula, um valor notável de CAS ( $\sim 32 \text{ mg g}^{-1}$  a 1,2 V), juntamente com 100% de retenção do desempenho foram observados ao longo de 100 ciclos. Os resultados obtidos permitiram uma melhor compreensão de como mitigar reações faradáicas e melhorar a estabilidade a longo prazo dos eletrodos de PAC, fornecendo eletrodos promissores para aplicações em larga escala de DIC.



## ABSTRACT

Capacitive deionization (CDI) emerged as a cost-effective alternative for the desalination of brackish water (salt concentration lower than  $10 \text{ g L}^{-1}$ ). Significant progress in electrode materials in terms of salt adsorption capacity (SAC) and charge efficiency ( $Q_E$ ) has been performed in the last few years. However, there are still challenging issues concerning the improvements of the adsorption/desorption kinetics and the electrode stability for long-term operation. In this sense, the main goal of this thesis was the development of stable electrodes of polyaniline (PAni)-activated carbons (PAC) for long-term desalination, with optimized electrosorption/desorption kinetics.

The comparison between blade-casting (DB) and free-standing (FS) electrodes of p-toluenesulfonate-doped PAC (PAC/PTS) showed the effects of electrode interparticle porosity and thickness on their textural and electrochemical properties and enabled a better understanding of how tuning the preparation technique of the CDI electrodes can improve the desalination performance, especially in terms of adsorption/desorption kinetics. Although the different electrodes perform similarly in terms of gravimetric salt adsorption capacities, FS electrodes outperform the DB electrodes in terms of volumetric salt adsorption capacities. These carbon films were more compact, and a large quantity of electroactive material was available for salt adsorption. Therefore, if the material cost is not a limitation, the maximum amount of salt could be removed using compact CDI cells with FS electrodes. On the other hand, when the electrosorption and desorption kinetics are considered, the DB electrode presented superior performance, mainly due to its higher interparticle porosity that minimizes the distance of ion diffusion from the bulk solution to the inner surface, thus facilitating the access of the ions to the micropores. These results demonstrated that the faster kinetics provided by enhanced mass transfer in thin electrodes with high interparticle porosity can be decisive for the selection of the best electrode in CDI applications, specially aiming for future applications in flow-through CDI cells.

Sequentially, different strategies were studied in order to optimize the desalination performance and the long-term operation stability of PAC/PTS electrodes. Additionally, the new sulfate-doped PAni-activated carbon (PAC/S) was proposed to investigate the influence of chemical and textural properties of the electrodes on the desalination stability. Chemical treatments with ethylenediamine and (3-aminopropyl)triethoxysilane were used to change the chemical surface groups and the potentials of zero charge ( $E_{PZC}$ ) to more negative values of the materials and promote asymmetry between the electrodes. Symmetric and membrane CDI (MCDI) configurations were also investigated for performance comparison. The control of the potential distribution in asymmetric cells was pointed out as an effective strategy to suppress the carbon oxidation reactions responsible for the SAC loss and improve the long-term stability. However, the best performance and long-term stability

were achieved using PAC/PTS electrodes in the MCDI configuration. The use of ion-exchange membranes (IEM) had proved to be a feasible method to improve the electrosorption capacity by reducing the effect of co-ion expulsion and inhibit the faradaic reactions by limiting the transport of the electrochemically active species across the IEM. For this cell configuration, a remarkable value of *SAC* ( $\sim 32 \text{ mg g}^{-1}$  at 1.2 V), along with 100% of performance retention was observed over 100 cycles. Our findings enable a better understanding of how to mitigate faradaic reactions and improve the long-term stability of PAC electrodes, thus providing promising electrodes for large-scale CDI applications.

## SUMÁRIO

CHAPTER 1 .....	1
INTRODUCTION .....	1
1.1. Desalination technologies.....	1
1.2. CDI technology .....	4
1.3. Improvements of CDI.....	6
1.4. Underlying the background .....	10
1.5. Objectives.....	13
1.6. Thesis outline .....	14
CHAPTER 2 .....	15
INSIGHTS ON THE ROLE OF INTERPARTICLE POROSITY AND ELECTRODE THICKNESS ON CAPACITIVE DEIONIZATION PERFORMANCE FOR DESALINATION...	15
2.1. Introduction .....	15
2.2. Materials and Methods .....	17
2.2.1. Materials.....	17
2.2.2. Activated carbon and electrode preparation .....	17
2.2.3. Characterizations .....	19
2.2.3.1. Textural characterizations .....	19
2.2.3.2. Electrochemical characterizations .....	20
2.2.4. Desalination.....	21
2.3. Results and Discussion.....	22
2.3.1. Textural characterizations .....	23
2.3.2. Electrochemical characterizations .....	27
2.3.3. Electrosorption .....	31
2.4. Conclusions .....	36
CHAPTER 3 .....	37
EFFICIENT AND STABLE OPERATION OF CAPACITIVE DEIONIZATION ASSESSED BY ELECTRODE AND MEMBRANE ASYMMETRY .....	37
3.1. Introduction .....	37
3.2. Experimental .....	39
3.2.1 Materials.....	39
3.2.2 PANi and AC syntheses, surface treatments, and electrode preparation .....	39
3.2.3 Characterization.....	40
3.2.3.1 Materials.....	40

3.2.3.2 Electrochemical .....	41
3.2.4 Electrosorption performance .....	42
3.3. Results and discussion.....	44
3.3.1 PAC characterization.....	45
3.3.2 Electrochemical characterizations .....	48
3.3.3 Electrosorption: Symmetric and asymmetric electrode configurations .....	52
3.3.4 Long-term desalination.....	58
4. Conclusions .....	66
CHAPTER 4 .....	67
CONCLUSIONS AND SUGGESTIONS FOR FUTURE WORKS .....	67
REFERENCES.....	69

## TABLES LIST

<b>Table 2.1.</b> Thicknesses, interparticle porosities, and contact angles of the electrodes. ....	23
<b>Table 2.2.</b> Electrode characteristics obtained from the N <sub>2</sub> adsorption-desorption isotherms: $SSA_{BET}$ , $SSA_{DFT}$ , volume of pores ( $V_T$ ), volume of micropores ( $V_{mic}$ ), volume of mesopores ( $V_{mes}$ ), and percentage of mesopores ( $\%V_{mes}$ ). ....	26
<b>Table 2.3.</b> EIS parameters obtained from the Nyquist plots and the modified Randle equivalent circuit. ....	29
<b>Table 2.4.</b> Total masses of active material ( $m_E$ ) and electrosorption performance parameters $SAC_M$ , $SAC_V$ , $Q_E$ , and $\eta$ for the different electrodes. ....	31
<b>Table 2.5.</b> Electrode $OSR$ values, considering an operational time of one day.....	34
<b>Table 3.1.</b> Polymerization ( $Y_{PAni}$ ), carbonization ( $Y_C$ ), activation ( $Y_A$ ) and overall ( $Y_0$ ) yields for PAC/S and PAC/PTS. ....	45
<b>Table 3.2.</b> Textural analysis: specific surface area ( $SSA_{BET}$ and $SSA_{DFT}$ ), total pore ( $V_T$ ), micropore ( $V_{mic}$ ) and mesopore ( $V_{mes}$ ) volumes, and percentage of mesopores ( $\%V_{mes}$ ). ....	47
<b>Table 3.3.</b> EDX elemental analysis .....	48
<b>Table 3.4.</b> EIS parameters obtained from the Nyquist plots and the modified Randle equivalent circuit. ....	51
<b>Table 3.5.</b> Electrosorption performance parameters ( $SAC$ , $Q_E$ , and $\eta$ ) for the different CDI cell configurations. Electrolyte: 1080 mg L <sup>-1</sup> NaCl; $E_{cell}$ : 1.2 V (adsorption) and 0.0 V (desorption). ...	55
<b>Table 3.6.</b> $OSR$ values, considering the operational time of one day. ....	57
<b>Table 3.7.</b> Long-term electrosorption performance for the cell configurations achieving desalination stability.....	60
<b>Table 3.8.</b> $E_{PZC}$ values of the positive electrodes before and after the long-term operation using the different asymmetric and MCDI configurations. ....	63
<b>Table 3.9.</b> $SAC$ and $Q_E$ values reported in the literature using carbon materials as CDI electrode. .	65

## FIGURES LIST

<b>Fig. 1.1.</b> Desalination technologies: Multi-stage flash distillation (a) [13]; reverse osmosis (b) [14]; and electro dialysis (c) [12].	3
<b>Fig. 1.2.</b> Scheme of a CDI device: electrosorption (a) and regeneration (b).	5
<b>Fig. 1.3.</b> The number of citations (a) and publications (b) per year in CDI. The research papers were retrieved from the Web of Science database (Access on January 2021).	6
<b>Fig. 1.4.</b> Schematic view of a membrane capacitive deionization (MCDI) [79] (a), flow-electrode capacitive deionization (FCDI) [78] (b), and inverted capacitive deionization (i-CDI) [51] (c) cells.	9
<b>Fig. 1.5.</b> Scheme of the co-ion effect for symmetric (a) and asymmetric configurations (b and c). $E_0$ is the short-circuit potential, and $E_-$ and $E_+$ are the potentials applied to the cathode and anode, respectively [119].	13
<b>Fig. 2.1.</b> Doctor-blade device.	19
<b>Fig. 2.2.</b> Blade-casting (a) and free-standing (b) electrodes.	19
<b>Fig. 2.3.</b> Schematic illustrations of the CDI cell (a) and the desalination setup (b).	21
<b>Fig. 2.4.</b> SEM images of the cross-sectional areas of the DB-320 (a), DB-402 (b), FS-282 (c), and FS-359 (d) electrodes. Top views of the DB-320 (e) and FS-282 (f) electrodes. Cross-sectional views of the DB-320 (g), DB-402 (h), FS-282 (i), and FS-359 (j) electrodes.	24
<b>Fig. 2.5.</b> Binarized black and white SEM micrographs produced using Image-Pro Plus 7. Cross-sectional views of DB-320 (a), DB-402 (b), FS-282 (c), and FS-359 (d). Top views of DB-320 (e) and FS-282 (f).	25
<b>Fig. 2.6.</b> Nitrogen adsorption-desorption isotherms (a) and pore size distributions (b) of the PAC/PTS and the DB-320, DB-402, FS-282, and FS-359 electrodes.	26
<b>Fig. 2.7.</b> Percentage losses of SSA (a) and $V_T$ (b) after electrode preparation.	27
<b>Fig. 2.8.</b> (a) Cyclic voltammograms acquired at $25 \text{ mV s}^{-1}$ and (b) GCD profiles obtained at $1 \text{ A g}^{-1}$ . Electrolyte: $1 \text{ mol L}^{-1} \text{ NaCl}$ .	28
<b>Fig. 2.9.</b> GCD capacitance vs. $SSA_{BET}$ for the DB and FS electrodes.	28
<b>Fig. 2.10.</b> (a) Nyquist plots and (b) plots of capacitance against frequency (inset: modified Randle equivalent circuit). Electrolyte: $1.0 \text{ mol L}^{-1} \text{ NaCl}$ ; potential: $0.0 \text{ V}$ ; AC amplitude: $10 \text{ mV}$ .	29
<b>Fig. 2.11.</b> EIS capacitance vs. $R_{CT}$ for the DB and FS electrodes.	30
<b>Fig. 2.12.</b> Desalination performances (a) and the electrosorption responses $m_R$ , $SAC_M$ , and $SAC_V$ (b) for the different electrodes. $E_{cell}$ : $1.2 \text{ V}$ (adsorption) and $0.0 \text{ V}$ (desorption); $632 \text{ mg L}^{-1} \text{ NaCl}$ . The error bars were calculated considering the electrosorption/desorption cycles at the steady state desalination (achieved after 5 cycles).	31

<b>Fig. 2.13.</b> Fluctuation of pH during the desalination cycles. Electrolyte: 632 mg L <sup>-1</sup> NaCl; $E_{cell}$ : 1.2 V (adsorption) and 0.0 V (desorption). .....	33
<b>Fig. 2.14.</b> ASAR as a function of $SAC_M$ for the different electrodes. ....	34
<b>Fig. 3.1.</b> CDI cell. ....	42
<b>Fig. 3.2.</b> SEM micrographs of the as-synthesized PACs, PACs after the chemical treatments, and YP-80F. ....	46
<b>Fig. 3.3.</b> Nitrogen adsorption-desorption isotherms at -196 °C (a) and pore size distribution (b). Inset: cumulative pore volume. ....	47
<b>Fig. 3.4.</b> Electrochemical characterizations of PAC and YP-80F electrodes: (a) CV recorded at 5 mV s <sup>-1</sup> ; (b) CV capacitance against scan rate; (c) GCD profiles recorded at 0.25 A g <sup>-1</sup> ; (d) GCD capacitance against specific currents; (e) Nyquist plots, and (f) modified Randle equivalent circuit. Electrolyte: 1 mol L <sup>-1</sup> NaCl. ....	50
<b>Fig. 3.5.</b> CV and GCD (a) capacitance vs. $SSA_{DFT}$ , and $A_0$ as a function of $V_T$ (b) and $V_{mes}$ (c) for PAC and YP-80F electrodes. ....	51
<b>Fig. 3.6.</b> CDI and MCDI performances of different symmetric and asymmetric electrode configurations using PAC/S (a) and PAC/PTS (b) electrodes. Electrolyte: 1080 mg L <sup>-1</sup> NaCl; $E_{cell}$ : 1.2 V (adsorption) and 0.0 V (desorption). ....	52
<b>Fig. 3.7.</b> (a) Normalized capacitance vs. electrode potential for PAC and YP-80F electrodes and (b) potential distribution of the symmetrical and asymmetrical CDI and MCDI configurations. $E_0$ is the short-circuit potential. $E_-$ and $E_+$ indicate the potential in the cathode and anode, respectively. The potentials were determined considering the electrosorption/desorption cycles at steady state. ....	53
<b>Fig. 3.8.</b> Schematic illustrations of the CDI cell used by Zornitta and Ruotolo [111] (a) and in this work (b). ....	55
<b>Fig. 3.9.</b> $SAC$ and $Q_E$ throughout the desalination cycles operated at different $E_{cell}$ for PAC/S(-)  (+sPAC/S (a), PAC/PTS(-)  (+Y P-80F (c), and MCDI PAC/PTS (e) configurations. Electrode potential distributions for PAC/S(-)  (+sPAC/S (b), PAC/PTS(-)  (+Y P-80F (d), and MCDI PAC/PTS (f) configurations. Electrolyte: 1080 mg L <sup>-1</sup> NaCl. The standard deviation regarding the potential limits is 5%. ....	59
<b>Fig. 3.10.</b> Cyclic voltammograms recorded at 5 mV s <sup>-1</sup> for sPAC/S (a), YP-80F (b), PAC/S (c), and PAC/PTS (d) electrodes without the use of IEMs, and for PAC/PTS using IEMs in the anodic (e), and cathodic (f) regimes. Electrolyte: 1 mol L <sup>-1</sup> NaCl. ....	61
<b>Fig. 3.11.</b> $R$ -value against the vertex potential for PAC/S, sPAC/S, PAC/PTS, and YP-80F (a), and for PAC/PTS using IEMs (b). ....	62

## NOMENCLATURE

$A_0$	Admittance	[mS s <sup>1/2</sup> ]
ASAR	Average salt adsorption rate	[mg/g s]
$C_1$	Capacitance at the electrolyte/electrode interface obtained from EIS	[F/g]
$C_2$	Capacitance developed inside the micropores of the carbon electrode obtained from EIS	[F/g]
$C_{GCD}$	Average capacitance obtained from charge-discharge	[F/g]
$C_{CV}$	Average capacitance obtained from CV	[F/g]
$C_{EIS}$	Average capacitance obtained from EIS	[F/g]
$C_S$	Specific capacitance	[F/g]
$D_c$	Converted deionization capacity	[mg/g]
$D_{H_3O^+}$	Diffusion coefficient of hydronium	[m <sup>2</sup> /s]
$D_{OH^-}$	Diffusion coefficient of hydroxyl	[m <sup>2</sup> /s]
e	Charge of the electron	[C]
$E_-$	Potential in the cathode	[V]
$E_+$	Potential in the anode	[V]
$E_{cell}$	Cell potential	[V]
$E_{cell-regeneration}$	Cell potential of regeneration	[V]
$E_o$	Short-circuit potential	[V]
$E_{PW-}$	Limiting potentials for reduction	[V]
$E_{PW+}$	Limiting potentials for oxidation	[V]
$E_{PZC}$	Potential of zero charge	[V]
$F$	Faraday constant	[C/mol]
$I$	Current	[A]
$I_d$	Discharge current	[A]
$k_B$	Boltzmann constant	[m <sup>2</sup> kg/s <sup>2</sup> K]
$k_e$	Electrosorption kinetics	[1/s]
$k_d$	Desorption kinetics	[1/s]
$m_E$	Total mass of active material in both electrodes	[g]
$m_{sr}/m_R$	Mass of salt removed	[mg]
$N_A$	Avogadro constant	[1/mol]
OSR	Optimized salt removal	[mg/g day]
OSR <sub>M</sub>	Optimized salt removal by mass	[mg/g day]
OSR <sub>V</sub>	Optimized salt removal by volume	[mg/g cm <sup>3</sup> ]
$Q_E$	Charge efficiency	[%]
$Q_{neg}$	Cathodic charge	[C]
$Q_{pos}$	Anodic charge	[C]
$R$	Faradaic Fraction	[-]
$R_{CT}$	Charge transfer resistance	[Ω]
$R_Ω$	Ohmic resistance	[Ω]
SAC	Salt adsorption capacity	[mg/g]
SAC <sub>M</sub>	SAC normalized by mass	[mg/g]



$SAC_V$	SAC normalized by volume	[mg/cm <sup>3</sup> ]
$SSA$	Specific surface area	[m <sup>2</sup> /g]
$SSA_{BET}$	SSA calculated by the Brunauer-Emmett-Teller equation	[m <sup>2</sup> /g]
$SSA_{DFT}$	SSA calculated by the 2D-NLDFT heterogeneous surface model	[m <sup>2</sup> /g]
$t_e$	Electrosorption time	[min]
$t_d$	Desorption time	[min]
$t_{op}$	Optimized electrosorption time	[s]
$V_{mes}$	Volume of mesopores	[cm <sup>3</sup> /g]
$V_{mic}$	Volume of micropores	[cm <sup>3</sup> /g]
$V_T$	Total pore volume	[cm <sup>3</sup> /g]
$W$	Warburg element	[ $\Omega/s^{1/2}$ ]
$Y_A$	Yield of activated carbon	[-]
$Y_C$	Yield of carbonized carbon	[-]
$Y_0$	Total yield	[-]
$Y_{PAni}$	Polymerization yield	[-]

**SYMBOLS**

$\eta$	Specific energy consumption	[J/mg]
$\nu$	Scan-rate	[mV/s]
$\omega$	Angular frequency	[rad/s]
$\sigma$	Conductivity	[ $\mu$ S/cm]
$\varepsilon$	Interparticle porosity	[-]
$\zeta$	Electrode thickness	[ $\mu$ m]
$\theta$	Contact angle	[ $^{\circ}$ ]

## ABBREVIATIONS

AC	Activated carbon
AEM	Anion-exchange membrane
APTES	(3-aminopropyl)triethoxysilane
BET	Brunauer-Emmett-Teller
CDI	Capacitive deionization
CEM	Cation-exchange membrane
CV	Cyclic voltammetry
DB	Electrodes produced by the doctor-blade method
ED	Electrodialysis
EDL	Electric double layer
EDX	Energy-dispersive X-ray
EIS	Electrochemical impedance spectroscopy
ePAC/PTS	p-toluenesulfonate-doped PAC treated with ethylenediamine
ePAC/S	Sulfate-doped PAC treated with ethylenediamine
FCDI	Flow-electrode capacitive deionization
FDI	Faradaic deionization
FS	Free-standing electrodes
GCD	Galvanostatic charge-discharge
HPTS	p-toluenesulfonic acid monohydrate
i-CDI	Inverse capacitive deionization
IEM	Ion-exchange membranes
MCDI	Membrane capacitive deionization
MED	Multi-effect distillation
MSF	Multi-stage flash distillation
NLDFT	Non-local density functional theory
NMP	n-Methylpyrrolidone
PAC	Polyaniline activated carbon
PAC/PTS	p-toluenesulfonate-doped PAC
PAC/S	Sulfate-doped PAC
PAni	Polyaniline
PAni/PTS	Polyaniline doped with p-toluenesulfonic acid
PAni/S	Polyaniline doped with sulfuric acid
PTFE	Polytetrafluoroethylene
PVDF	Polyvinylidene fluoride
PSD	Pore size distribution
PSW	Potential stability window
RO	Reverse osmosis
SEM	Scanning electron microscopy
sPAC/PTS	p-toluenesulfonate-doped PAC treated with APTES
sPAC/S	Sulfate-doped PAC treated with APTES

# CHAPTER 1

## INTRODUCTION

Water is one of the key resources for human development. Estimates suggest that its use has been increasing worldwide by about 1% per year since the 1980s, driven by a combination of population growth, socio-economic development, and evolving consumption patterns. However, this rising demand coupled with the diminishing water supply due to climate change and contamination are exacerbating water scarcity in many world regions. In this context, over 2 billion people live in countries that are subject to high water stress, and about 4 billion experience conditions of severe water scarcity during at least one month of the year [1,2]. Accordingly, three out of ten people (2.1 billion people) did not use a safely managed drinking water service in 2015, and this number tends to increase as the demand grows and the effects of climate change intensify [2].

Even in Brazil, where 8% of the planet's water reserves are present, issues related to this resource have also become extremely relevant. This growing concern is result of drought episodes experienced in highly populated areas and the unequal distribution of water in the national territory. For instance, about 80% of water resources are available in the Amazon basin, where the population is small compared to other areas, and the water demand is lower [3].

This scenario in Brazil and worldwide demonstrates that conventional approaches relying on rainfall and river runoff are no longer sufficient to meet human demands in drought areas. Therefore, non-conventional water resources, such as desalinated water, are expected to play a key role in reducing the water demand-supply gap.

### 1.1. Desalination technologies

The desalination process removes salts from saline or brackish water to produce water that meets the quality requirements of different human uses. Typically, the separation of pure water from a saline solution is driven by either thermal-, pressure-, or electrochemical-based gradients [4].

The first desalination plants predominantly utilized thermal desalination (distillation). Countries in the Middle East pioneered the design and implementation of seawater thermal desalination, first using the multi-effect distillation (MED) and later using the multi-stage flash (MSF) distillation. The last one became more used between the two distillation techniques due to its reliability and simplicity [5,6].

The MSF process is based on a series of flash chambers where steam is generated from saline feedwater at a progressively reduced pressure (Fig. 1.1(a)). The evaporated water is condensed by

heat exchange with a series of closed pipes where the seawater to be desalinated is preheated. Collector trays are used to gather the condensate, which is obtained as pure water. The brine solution is partly recirculated to obtain a higher water recovery, and partly rejected to the sea [5]. Advances in this technology, such as the use of membrane distillation may prolong its lifetime. Furthermore, the feedwater warming by the heat from the evaporated water reduces the overall energy demand of the process. However, the energy requirement remains high and makes this technology only feasible in countries where the energy cost is not an obstacle.

Reverse osmosis (RO) is a pressure-driven separation process. High pressure is used to force a saline stream through a membrane only permeable for water, resulting in brine and purified water streams (Fig. 1.1(b)). The separation is promoted by applying a pressure higher than the osmotic pressure of the saline stream. Furthermore, the pre-treatment of feedwater is essential to protect the membrane, increase salt retention, and reduce the energy costs of this desalination process [7].

Typically, the RO systems have a recovery rate between 33% and 98%, depending on the quality of feedwater, pressure applied, and configuration [8]. Commercial interest in RO technology is increasing globally due to the continuous advances in membrane materials, process design, feed pre-treatment, and energy recovery [9]. However, the major concerns about the RO technology is related to the high energy consumption and membrane replacement costs [10].

The electrodialysis (ED) is also a membrane-based separation process, but in this case, the ions are driven through ion-selective membranes under the influence of an electric field developed between two electrodes (Fig. 1.1(c)). When a high voltage is applied between the electrodes, hydronium and hydroxyl ions are formed on the anode (Eq. 1.1) and cathode (Eq. 1.2), respectively. Based on the principle of electroneutrality, a counterbalance is established, and the sodium cations migrate through the cation-exchange membranes (CEM), while the chloride anions move through the anion-exchange membrane (AEM). This movement causes an increase in the concentration of ions in some compartments (brine streams), while it decreases in the adjacent ones (diluted streams) [11].



In general, the ED has a high recovery rate and can remove 75% to 98% of total dissolved solids from feedwater. Furthermore, it is possible to clean the membranes reducing fouling and incrustation by reversing the polarity in reverse ED [7]. However, the process is not economically competitive with other technologies for desalination when the water concentration is higher than 6000 mg L<sup>-1</sup> of dissolved solids [11,12].

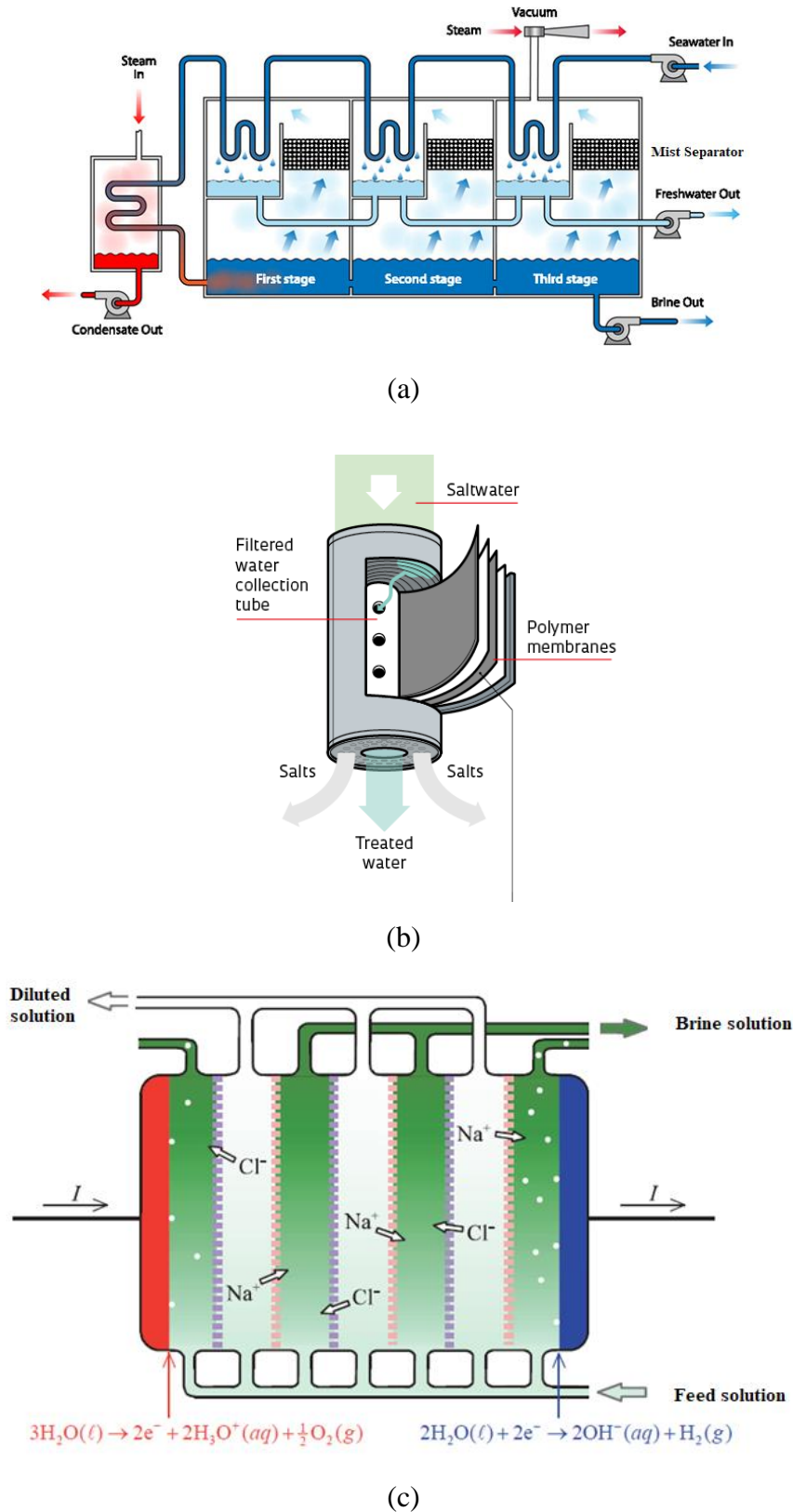


**Fig. 1.1.** Desalination technologies: Multi-stage flash distillation (a) [13]; reverse osmosis (b) [14]; and electrodialysis (c) [12].

Nowadays, according to Jones et al. [6], 15,906 desalination plants are in operation on the planet, with the capacity to produce around 95 million  $\text{m}^3/\text{day}$  of desalinated water. The majority of

desalination facilities are located in high-income countries, accounting for the majority of the global desalination capacity. Therefore, almost half of the global desalination capacity is located in the Middle East and North Africa region (48%), with Saudi Arabia, the United Arab Emirates, and Kuwait being the major producers in the region and globally. Among the desalination technologies, RO is the predominant process employed, accounting for 84.5% of the total number of operational desalination plants, and producing 69% of the total global desalinated water. The thermal technologies, MSF and MED, despite being relatively few in numbers, produce 18% and 7% of the desalinated water, respectively. The electrodialysis corresponds to 5.9% of total plants, but produces only 2% of the volume of desalinated water.

In the Brazilian context, there are some RO units employed for water desalination. For instance, a small-scale RO system at Fernando de Noronha archipelago produces about 720 m<sup>3</sup>/day of water and meets 40% of the archipelago's water requirement. In addition, some communities in the Brazilian semiarid region also depend on the RO systems to obtain potable water. However, most of these desalinators do not work properly due to the misuse and lack of resources for adequate maintenance [14].

Although the continued improvements in energy recovery systems, membrane technologies, and coupling desalination plants with renewable energy sources allowed the reduction of energy consumption, and capital and operational costs of the current desalination technologies [13,15,16], the high energy consumption, membrane costs, and difficulty of operation and maintenance are still drawbacks. Therefore, the search for strategies to further reduce the costs of the current technologies and the development of new technologies are still required to spread the use of desalination to produce drinking water.

In this scenario, recently a new technology called Capacitive Deionization emerged as a promising alternative to desalinate water.

## 1.2. CDI technology

Capacitive deionization (CDI) has emerged in the last few years as a promising technology for the desalination of brackish water (salt concentration lower than 10 g L<sup>-1</sup>). This process can reduce the energy costs of desalination and become competitive with other well-established technologies [11,17].

The CDI process is based on the ion storage in the electrical double layers (EDLs) formed on the pore surface of carbon electrodes when a low potential difference or current is applied. A representation of the most common CDI configuration is shown in Fig. 1.2. In the electrosorption process (Fig. 1.2(a)), ions are attracted and stored in the oppositely-charged electrode, reducing the

concentration of salt in the treated solution. After some time, the accessible pore volume is completely saturated with electrosorbed ions and the maximum storage capacity of the electrodes is reached. Therefore, in order to regenerate the electrodes and restore their initial ion uptake capacity, the ions are desorbed from the carbon pores into a waste brine stream by reversing the applied voltage or short-circuiting the system (Fig. 1.2(b)). Ideally, without the presence of faradaic reactions, this process is purely physical and potentially enables CDI devices to have a long service life [18].

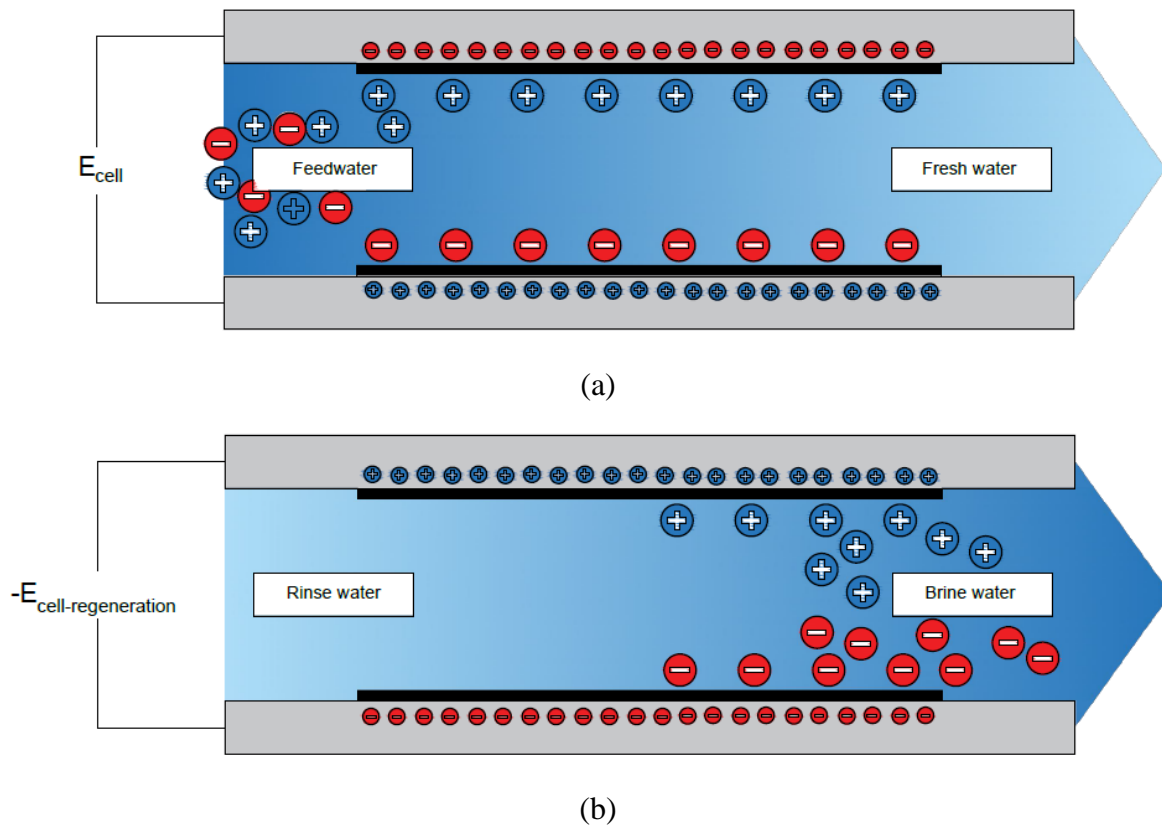


**Fig. 1.2.** Scheme of a CDI device: electro sorption (a) and regeneration (b).

The relatively low voltage ( $<2.0$  V) and the absence of hydraulic pressure are the main advantages of the CDI process, which result in the reduction of operating and energy costs [19]. Besides, as CDI is a capacitive technology, part of the energy invested for the electro sorption process can be recovered through electrode regeneration, which reduces even more the total energy consumption [20,21].

The salt content of the deionized effluent of RO systems generally is extremely low, making it unpalatable and unhealthy. Therefore, the effluent has to be hardened. For CDI systems, this problem does not occur since the process allows to control the deionized effluent quality. Furthermore, CDI is less susceptible to biofouling (biological growth) and scaling (precipitation of salts) when compared to the RO process [22,23].



High water recoveries (about  $> 80\%$ ) for brackish water treatment are also achieved in this process [24]. Although the CDI is a significantly less mature technology than reverse osmosis, multi-effect distillation, multi-stage flash distillation, and electrodialysis, studies have shown the strong potential of CDI to become a competitor with these technologies, especially for small desalination devices or plants to desalinate brackish water.

### 1.3. Improvements of CDI

The first studies on CDI date to the mid-1960s and early 1970s. Its concept was firstly introduced by Caudle et al. [25], who used porous electrodes of activated carbon in a water desalination system. Later, studies of the A. M. Johnson's group brought fundamental contributions to understand the basic factors governing CDI [26–28]. Studies directed at developing novel electrode materials and semi pilot-sized devices for water desalination were performed, but mainly because of the instability of the electrodes, particularly the anode, these studies were discontinued. In 1996, Farmer et al. [29] developed at Lawrence Livermore National Laboratory a type of carbon aerogel with characteristics suitable for CDI application. However, only in 2009 (Fig. 1.3), the number of studies on capacitive deionization began to grow exponentially, mainly due to the development of new electrode materials and the establishment of new research groups in this area. Most of these studies have focused to improve electrode materials characteristics, explore new cell architectures, and optimize operational conditions in order to increase the salt adsorption capacity ( $SAC$ ) and charge efficiency ( $Q_E$ ) of CDI operations [30,31].

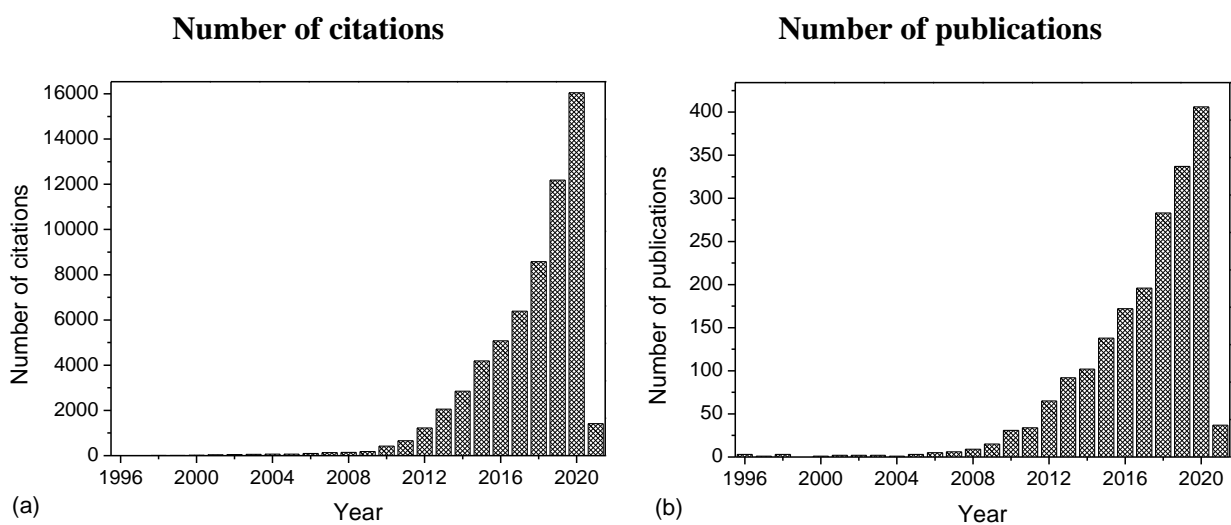


**Fig. 1.3.** The number of citations (a) and publications (b) per year in CDI. The research papers were retrieved from the Web of Science database (Access on January 2021).

Electrode material development is fundamental for achieving high desalination capacity and removal efficiency. A suitable CDI electrode material should have the following properties: (1) high specific surface area (SSA) available for electrosorption; (2) proper pore size distribution; (3) high electronic conductivity; (4) fast response of the entire surface area to electrosorption/electrodesorption cycles; (5) good wettability (or hydrophilicity); (6) chemical and electrochemical stability over a wide range of pH values and ability to tolerate frequent voltage changes; and (7) low-cost, abundance, and environmentally friendly [18]. Taking into account these requirements, carbon-based materials are largely used for CDI.

Among the various forms of carbon investigated for CDI are the carbon nanotubes [32,33], graphene [34–36], carbon aerogels [37–40]; carbon cloths [41], carbon sponges [42], activated carbons [43], and carbide-derived carbons [44]. Although most of these materials present promising results in terms of salt adsorption capacity, some are difficult to synthesize and not cost-effective, such as carbon nanotubes and graphene. Thus, recent studies have been devoted to the production of low-cost CDI electrodes. In this sense, activated carbons from different biowastes, such as coconut shells [45], wood [46], sugarcane bagasse [47], and sugarcane bagasse fly ashes [48] are being prepared recently.

The electrosorption performance depends strongly on the surface chemistry of the electrodes. In this sense, approaches were performed to modify the surface of carbon materials already used in CDI. For instance, Liu et al. [49] modified three-dimensional graphene by attaching amine and sulfonic functional groups. These functional groups acted as ion-selective functional coatings to minimize the co-ions expulsion effect and increased the wettability of the electrodes. Consequently, the modified materials reached better performance regarding capacity and rate of the deionization. The introduction of oxygen surface groups (hydroxyl, carboxyl, and carbonyl species) in the carbon matrix was reported to be also beneficial for the process of electrosorption, mainly due to the increase of wettability [50] and the displacement of the potential of zero-charge of the electrode [51]. In this context, Zornitta et al. [52] and Lado et al. [53] demonstrated that the high content of surface oxygen groups due to the activation with KOH of polyaniline and sugarcane bagasse fly ash led to expressive SAC enhancement. Loading the carbon materials with metal oxides was also performed to improve CDI performance, e.g. TiO<sub>2</sub>, CeO<sub>2</sub>, Fe<sub>2</sub>O<sub>3</sub> and Mn<sub>3</sub>O<sub>4</sub> [54], ZnO [55–58]; MnO<sub>2</sub> [59,60], and TiO<sub>2</sub> [61].

Despite these improvements in carbon-based materials, the intrinsically limited double-layer charge-storage capacities of porous carbon electrodes (desalination capacity for NaCl between 15-25 mg g<sup>-1</sup>) has recently encouraged the use of battery materials for water desalination [62]. In this sense, Faradaic reactions replace the non-Faradaic process of ion electrosorption for reversible electrochemical desalination processes [63]. Two-dimensional materials of transition-metal carbides

(MXenes) [64–66] and transition-metal dichalcogenides [67,68] have been used to remove chloride ions from saline water. Other intercalation-type battery electrodes have been used exclusively for the removal of cations, such as sodium manganese oxide [69], sodium iron phosphate [70], nickel hexacyanoferrate [71,72], vanadium oxide [73], and titanium disulfide [74]. Faradaic deionization (FDI) has achieved desalination capacities superior to those obtained for pure CDI, which can be attributed to the higher specific capacity of faradaic materials and their high selectivity for cations or anions, which avoids the co-ions repulsion effect. On the other hand, one of the primary challenges for the FDI technology is the low desalination rates, which are characteristic of battery materials [75,76]. The major rate-limiting factors are the low electrical conductivities of many battery materials, the activation energy barriers for the reactions, and the slow solid-state ion transport [62].

In addition to studies on electrode materials, efforts have been devoted to developing new CDI cell configurations, such as the membrane CDI (MCDI) [77], flow-electrode CDI (FCDI) [78], and inverted CDI (i-CDI) [51]. MCDI is the most important improvement to conventional CDI, which was developed by affixing ion-exchange membranes (IEMs) adjacent to the carbon electrodes. An anion-exchange membrane (AEM) and a cation-exchange membrane (CEM) are placed adjacent to the positive electrode and negative electrodes (Fig. 1.4(a)), respectively.

In a typical CDI process, the counterions are adsorbed in the electrical double layers (EDLs) formed within the micropores of the porous carbon electrodes, and the contribution of the macropores to the EDL is negligible [79]. In MCDI, during the electrode polarization, the co-ions that are expelled from the micropores are blocked by the membrane and cannot leave the electrode region. Hence, these co-ions remain stored in the macropores and due to charge neutrality requirements, the counterions accumulate in the macropores, thus resulting in higher removal of counterions from the electrolyte [79,80]. In addition, the ion-exchange membranes block the co-ions from getting re-adsorbed by the other electrode in the regeneration step when the applied voltage is reversed, thus improving the adsorption capacity of electrodes in the next cycle [20]. In general, the prevention of co-ion repulsion, the high concentration of co-ions in the macropores (which provides a driving force for the attraction of counterions), and the reduction of the concentration of dissolved oxygen at the electrode region have positive effects on the use of membranes that improve the salt adsorption capacity, charge efficiency and stability of carbon electrodes [79,81,82].

The flow-electrode capacitive deionization (FCDI), firstly reported by Jeon et al. [83], employs as electrode suspended carbon materials, which flow between an ion-exchange membrane (AEM and CEM) and a current collector (Fig. 1.4(b)). This cell configuration allows a substantial increase in the quantity of carbon electrodes available for ion adsorption and, thus, delivers a larger desalination capacity than conventional MCDIs [78]. The FDIC also enables continuous desalination, and the ion desorption is done externally by mixing the carbon electrode particles effluent from both

anode and cathode. Thus, only the ion adsorption is performed inside the FCDI cell, a feature that makes this configuration particularly suitable for large-scale industrial applications. However, efforts are needed to enhance the electronic charge transfer between the current collector and the flow-electrode to achieve better FCDI performance [78,84].

In 2015, Gao et al. [51] proposed the use of the i-CDI system to overcome the problem of oxidation of the anode in an aqueous solution. In this system, the desalination is mainly achieved by a spontaneously formed EDL at a chemically-modified surface of a carbon electrode without an external power source. Hence, the fixed charges at an electrode surface are used to spontaneously adsorb ions during the adsorption step and an applied voltage from an external power source is used to desorb ions during the regeneration step (Fig. 1.4(c)).

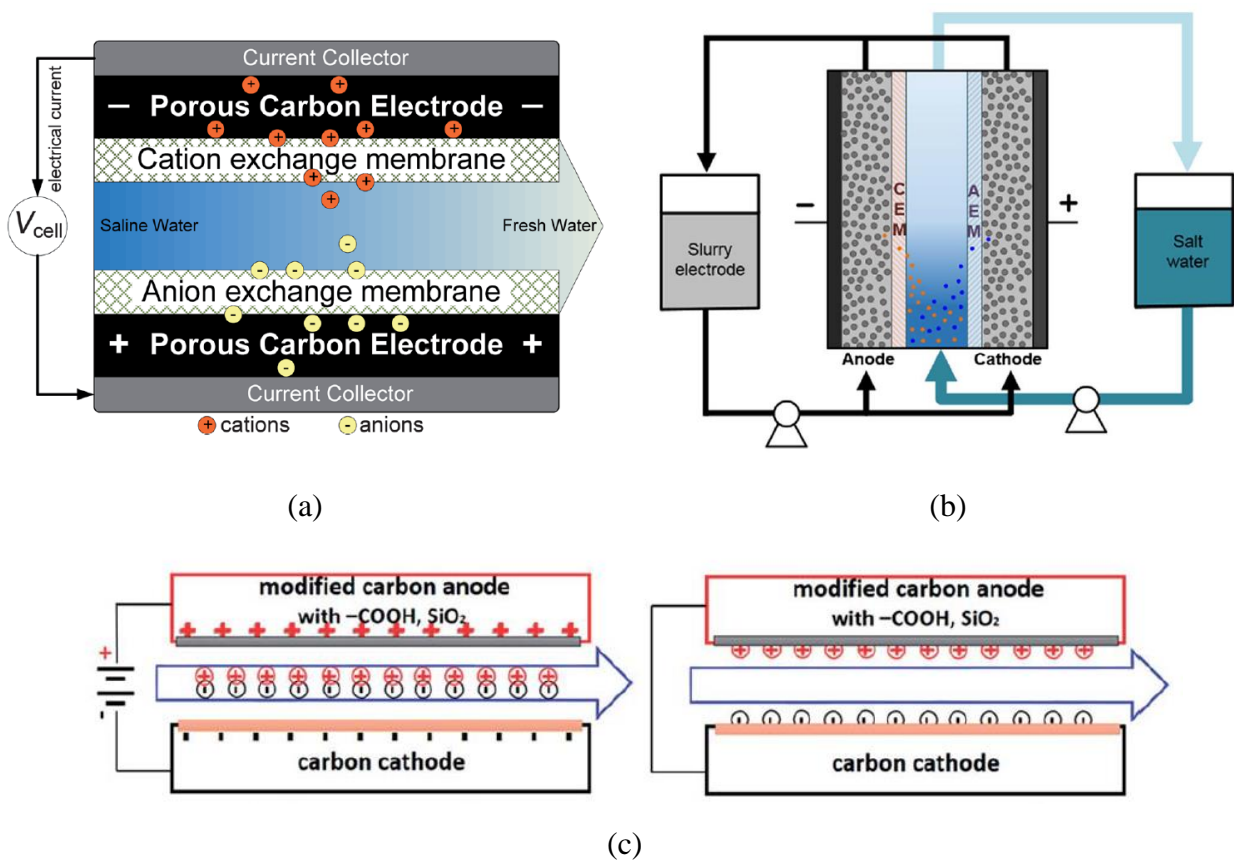


**Fig. 1.4.** Schematic view of a membrane capacitive deionization (MCDI) [79] (a), flow-electrode capacitive deionization (FCDI) [78] (b), and inverted capacitive deionization (i-CDI) [51] (c) cells.

As discussed so far, a significant progress in terms of materials used as CDI electrodes and cell configurations has been performed. The knowledge base of CDI was created and the effectiveness of this technology for water desalination was demonstrated in many studies. However, some challenging issues must be overcome in order to become CDI effective for application, such as the improvements of the adsorption/desorption kinetics and electrode stability for long-term operation.

## 1.4. Underlying the background

Recently, studies have been reported the improvement of CDI performance with the use of nitrogen-doped activated carbons as electrode material [19,85–87]. This improvement is mainly ascribed to the combination of the EDL capacitive charging derived from carbon and pseudocapacitive reactions from nitrogen functional groups [88]. Furthermore, the presence of these functionalities also enables the enhancement of wettability, conductivity, and electro-active surface area [19,42,85,89].

One of the usual approaches to introduce nitrogen-groups into porous carbon frameworks is the post-treatment with ammonia [90]. However, this method can lead to a low nitrogen content, inferior pore structures, and poor thermal stability [91]. To overcome these drawbacks, the direct carbonization of nitrogen-containing carbon precursors, such as glucosamine hydrochloride [92,93], polyacrylonitrile [94,95], polyaniline [96–98], and polypyrrole [99] were successfully performed.

Among N-containing precursors, polyaniline (PAni) is a low-cost polymer that can be easily synthesized, besides its stability and graphite similar structure that facilitates the introduction of nitrogen-containing active sites inside the carbon matrix, reaching a high N-content (~15 wt.%) [100,101]. In addition, the polymer properties can be easily customized by changing the doping anion during the polymerization process [102]. Hence, these features encourage the application of polyaniline as precursor for the synthesis of activated carbon.

Depending on the synthesis process and activation method, polyaniline-activated carbon (PAC) presents high specific surface area [103,104], high capacitance [88,96], good wettability [88], and long-term stability [96,100]. Thus, PAC has already been used for different applications, such as adsorption [97,103], supercapacitors [96,100,102,105–110], and electrocatalysts [98,108].

The use of PAC for CDI was reported for the first time by Zornitta et al. [52], which demonstrated that this activated carbon can be successfully employed as an electrode material for desalination. The authors demonstrated that the properties (conductivity, surface groups, and pore structure) and the desalination performance of PAC change when PAni is doped with different anions, such as chloride ( $\text{Cl}^-$ ), p-toluenesulfonate ( $\text{PTS}^-$ ), dodecylbenzene-sulfonate ( $\text{DBS}^-$ ) and polystyrenesulfonate ( $\text{PSS}^-$ ). Although  $\text{PTS}^-$ -doped PAC (PAC/ $\text{PTS}$ ) presented lower specific surface area and mesopore ratio, the best salt adsorption capacity ( $SAC$ ) and charge efficiency ( $Q_E$ ) was obtained using this electrode due to its higher polar surface group content. After that, other studies were carried out in order to improve  $SAC$  and  $Q_E$  of PAC/ $\text{PTS}$  electrodes by employing ion-exchange membranes and asymmetric configurations [111]. Chemical and textural properties were also optimized by changing the PAni carbonization and KOH activation conditions [112]. Although impressive improvements have been made on PAC/ $\text{PTS}$  electrode, increasing the  $SAC$  from 14.9 to

22.2 mg g<sup>-1</sup>, some issues related to the use of polyaniline-activated carbon for CDI desalination are not yet clear and/or must be optimized.

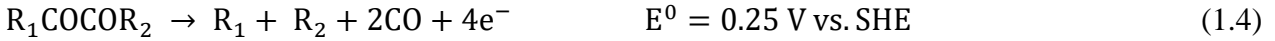
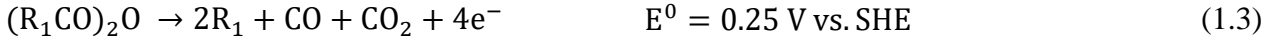
Besides the salt adsorption capacity, the kinetics improvement is also of paramount importance to optimize the CDI performance of activated carbons electrodes, since affects the number of adsorption/desorption cycles, thus determining the amount of salt removed in a given operational time [111]. It is known that electrosorption and desorption kinetics depend significantly on textural properties since they impact the mass transport. More specifically, the pore size distribution of the AC affects the internal mass transfer within the particle, while the interparticle porosity and flow patterns through the electrode influence the external mass transfer. Considering the inner porosity, although the micropores (<2 nm) are the main ion adsorption sites [44], their reduced dimensions limit the mass transport. Nevertheless, the kinetics can be improved by the presence of mesopores (2–50 nm), which provide a smaller resistance pathway for ion transport [113–115]. In this context, efforts have been devoted to developing new electrode materials that present a wide porosity to take advantage of the merits of each pore system and improve the adsorption/desorption kinetics [116,117]. Additionally, the ion-buffering reservoirs formed inside interparticle porosity can minimize the distance of ion diffusion from the bulk solution to the inner surface, also facilitating the access of the ions to the micropores.

Despite their importance, the influence of porosity on kinetic aspects is poorly explored in literature. Therefore, considering that the AC pore size distribution can be modified during the electrode preparation, a comprehensive and systematic study of the textural and electrochemical properties of electrodes prepared by different techniques was proposed. This work is expected to enable to tune the electrode preparation technique, in order to optimize the CDI desalination process in terms of salt adsorption capacity and adsorption/desorption kinetics.

The long-term stability is also an important parameter to ensure the application feasibility of polyaniline-activated carbons for CDI. Considering that during the long-term operation, the lifetime of carbon electrodes can be shortened and their desalination performance reduced due to possible faradaic processes [118,119], a study of electrode stability is mandatory. Among the faradaic reactions (e.g. carbon oxidation, water oxidation, and dissolved oxygen reduction), the stability loss is mainly attributed to the oxidation of the carbon anode, which forms oxygen functional groups into the carbon surface, shifting the potentials of zero charge ( $E_{PZC}$ ) of the electrode to more positive values and aggravating the co-ion expulsion effect [51,63,118,120]. In addition, the increase of electrode resistivity and decrease of surface area and pore volume have also been associated with the oxidation of carbon electrodes [81,121–123].

In recent work, Zornitta et al. [119] suggested that the oxidation reactions of the surface functional groups (Eqs. 1.3 and 1.4; [124]), which occur at low electrode potentials, contribute to the

lower stability of lignin-derived activated carbon. This issue shows the importance of studying the stability of polyaniline-activated carbon electrodes, which tend to present a high content of surface oxygen groups, including hydroxyl, carboxyl, and carbonyl species, resulting from the KOH activation process [112].



To suppress the oxidation reactions and improve the long-term stability, some strategies can be adopted. Studies reported the improvement of the desalination performance using asymmetric electrodes due to the  $E_{PZC}$  shifting, which maximizes the effective electrode potential used to adsorb ions and reduces the co-ion expulsion [51,81], and the introduction of additional attractive forces to remove the ions from the electrolyte [125]. These strategies improved the  $SAC$  and  $Q_E$  and could also be used to improve the long-term stability of carbon electrodes.

To better understand the positive effects of using asymmetric electrodes on long-term stability, Fig. 1.5 provides a comparison of the symmetric (Fig. 1.5(a)) and asymmetric (Fig. 1.5(b) and (c)) configurations. Fig. 1.5(a) shows the case in which symmetrical electrodes (with a negative surface charge, as most of the KOH-activated carbons) have a higher  $E_{PZC}$  value than the short-circuit potential ( $E_0$ ). In this configuration, part of the applied potential at the positive electrode is used for electrosorption of counterions (anions), while the other part is also consumed for co-ion expulsion. On the other hand, at the negative electrode, most of the potential contributes toward the electrosorption of counterions (cations). In the configuration shown in Fig. 1.5(b), the  $E_{PZC}$  values of the two electrodes are located within their corresponding polarization window, so part of the applied potential at both electrodes is used for co-ion expulsion, and a diminished useful adsorption potential is observed. The most desirable configuration for the CDI process is shown in Fig. 1.5(c). The electrode with  $E_{PZC}$  value in the positive window is placed on the negative side, and the electrode with  $E_{PZC}$  value in the negative windows is placed on the positive side. In this case, the co-ion expulsion effect becomes less significant and most of the potential is beneficial for electrosorption of counterions. In addition, the electropositivity and electronegativity of anode and cathode surface, respectively, can also contribute to the adsorption of anions in the anode and cations in the cathode. Hence, the use of chemical treatments to tune the chemical surface charge of the activated carbon and creating asymmetric electrodes seems to be a promising strategy to minimize the effect of co-ion expulsion, which is aggravated by the  $E_{PZC}$  positive shifting during long-term CDI operation.

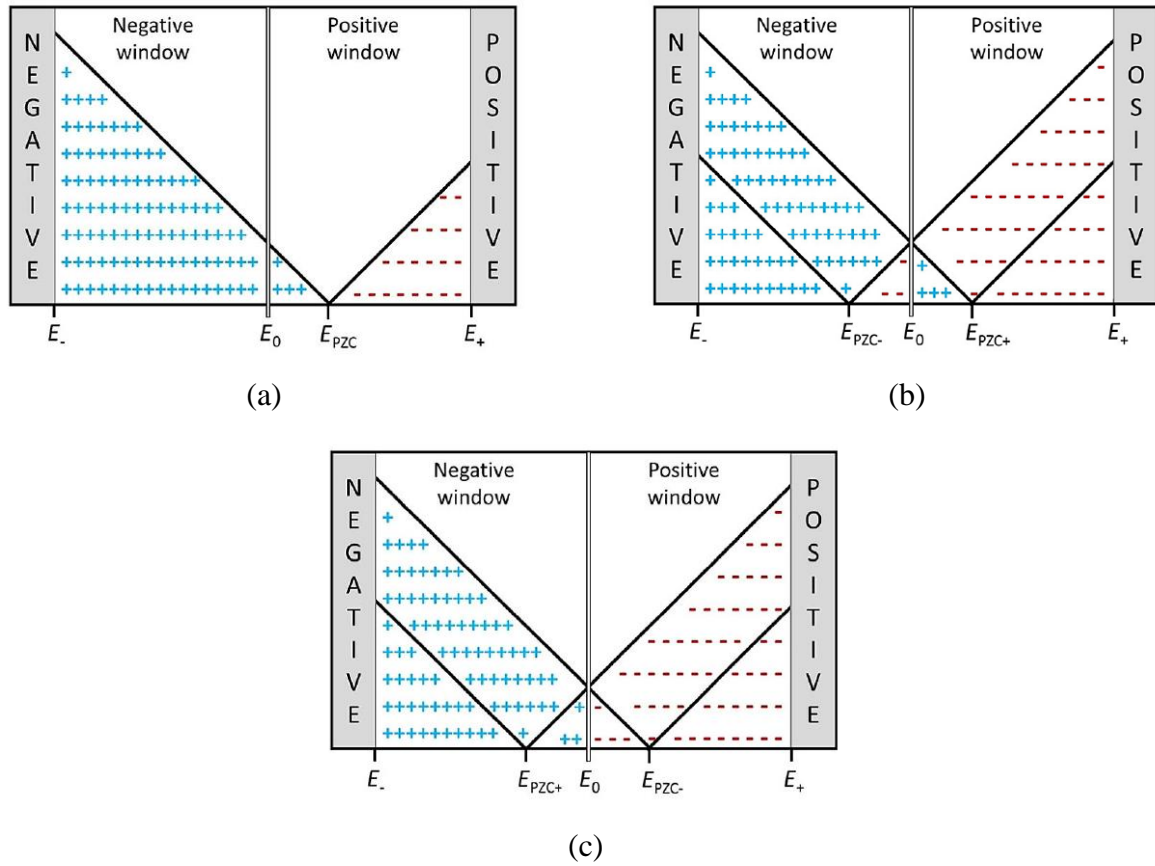


**Fig. 1.5.** Scheme of the co-ion effect for symmetric (a) and asymmetric configurations (b and c).  $E_0$  is the short-circuit potential, and  $E_-$  and  $E_+$  are the potentials applied to the cathode and anode, respectively [119].

As previously stated, the introduction of ion-exchange membranes into CDI cells has also proved to be a feasible method to improve the electrosorption capacity by reducing the effect of co-ion expulsion [80]. In addition, MCDI can inhibit the faradaic reactions by limiting the transport across the IEM of the electrochemically active species, such as dissolved oxygen and oxygen peroxide [126]. Considering the aforementioned aspects, in this work, asymmetric configurations and membrane CDI will be evaluated as strategies to minimize the oxidation on the positive electrode and the co-ion expulsion and, consequently, optimize the desalination performance and the long-term operation stability of PAC electrodes.

## 1.5. Objectives

Considering the gaps concerning the use of PAC as electrode material for CDI, the main goal of this thesis is the development of stable electrodes for long-term desalination, with optimized electrosorption/desorption kinetics. In order to achieve this goal, the specific objectives were established:



- Optimize the textural and electrochemical properties of PAC electrodes by using different electrode preparation procedures and electrode thicknesses in order to enhance the adsorption capacity and adsorption/desorption kinetics.
- Reduce the effect of co-ion expulsion and the electrode degradation by using asymmetric configurations and membrane CDI in order to improve the desalination performance and improve the electrode stability for long-term operation of PAC electrodes.

## 1.6. Thesis outline

In this thesis, activated carbons prepared using polyaniline as precursor were employed as electrode material for capacitive deionization desalination. The main purpose of this work is to understand the electrochemical phenomena affecting the capacitive deionization in order to improve the PAC electrodes to achieve fast kinetics, high salt electrosorption capacity, and long-term stability.

The results are presented in two chapters. In Chapter 2, different PAC/PTS electrodes were compared regarding their preparation procedure: 1) supported on current collectors produced by the doctor-blading procedure, using polyvinylidene difluoride (PVDF) as binder, and 2) free-standing electrodes produced using polytetrafluoroethylene (PTFE) as binder. A comprehensive study of how the electrode thickness, interparticle porosity, and hydrophilicity affect the electrochemical properties of these electrodes was carried out. The importance of the interparticle porosity in terms of salt adsorption capacity and electrosorption/desorption kinetics was evidenced and enabled a better understanding of how tuning the preparation technique of CDI electrodes can improve de desalination performance.

In Chapter 3, different strategies were studied in order to improve the long-term stability of CDI desalination experiments using activated carbon derived from PANi doped with p-toluenesulfonic acid (PAC/PTS) and sulfuric acid (PAC/S). Chemical treatments of the PAC with ethylenediamine and (3-aminopropyl)triethoxysilane were used to provide a positive charge on the surface of the materials and promote asymmetry between the electrodes. The use of asymmetric configurations and ion-exchange membranes minimizes the effect of co-ion expulsion and the electrode degradation. In this sense, we found electrode configurations and cell potentials that optimize the desalination capacity and long-term operation stability of PAC/S and PAC/PTS electrodes.

In Chapter 4, an overall conclusion about the main results obtained in this thesis is presented, along with suggestions for future works.

## CHAPTER 2

### INSIGHTS ON THE ROLE OF INTERPARTICLE POROSITY AND ELECTRODE THICKNESS ON CAPACITIVE DEIONIZATION PERFORMANCE FOR DESALINATION

Capacitive deionization (CDI) is a promising desalination technology employing activated carbon as an electrode material. Although there have been many works concerning carbon preparation, much less attention has been paid to electrode development. Here, we report a comprehensive and systematic study of electrode preparation by blade-casting (DB) and free-standing (FS) techniques. The thickness, interparticle porosity, and hydrophilicity of the electrodes obtained by the different techniques affected their textural and electric properties, consequently influencing their CDI performance. Although there was no significant difference in the gravimetric salt adsorption capacity values ( $SAC_M$  between 14.7 and 16.9 mg g<sup>-1</sup>), the volumetric salt adsorption capacities indicated superior performance of the FS electrode. However, when the  $SAC$  was considered together with the electrosorption and desorption kinetics, the DB electrode outperformed the FS electrode, mainly due to the fast kinetics ascribed to the improved mass transfer provided by the large interparticle voids of the DB carbon films. The results demonstrated that the faster kinetics provided by enhanced mass transfer in thin electrodes with high interparticle porosity can be decisive for selection of the best electrode in CDI applications.

#### 2.1. Introduction

According to international organizations, the water supply for human and animal consumption, and industry is one of the major challenges of this century [1], thus the search for water resources has become a priority in many regions of the planet, especially those suffering regular droughts [127,128]. Technologies such as reverse osmosis (RO), multi-stage flash distillation (MSF), and electrodialysis (ED) have been used for desalination, mainly to obtain potable water from seawater. However, the high energy consumption for desalination of brackish water has stimulated the development of new desalination technologies. Additionally, the use of membranes (RO and ED), high voltages (9–18 V) (ED), and high pressures (RO) make these technologies less attractive due to the capital and operational costs [11]. Hence, there is a need for studies focusing on emerging desalination technologies capable of reducing the salt concentration, while decreasing the specific energy consumption (kWh per kg of salt removed) of the process.

Capacitive deionization (CDI) is an emerging energy-efficient desalination technology that can provide high water recovery, based on the electrosorption of salts using a pair of electrically charged porous electrodes [11,17]. A constant current or potential can be applied to a pair of

electrodes in order to provide the driving force for cations and anions to be stored in the electric double layers (EDLs) formed at the negatively and positively charged electrodes, respectively. Once saturated, the electrodes can be regenerated to enable operation in consecutive cycles of electrosorption/desorption. Considering that CDI operates similarly to a supercapacitor, part of the energy consumed in the desalination step can be recovered during the desorption step [20,129,130]. This advantage, together with the application of low potentials (typically 1.2 V) and high water recovery, makes CDI an attractive energy-efficient option for brackish water desalination. Despite these advantages, the specific energy consumption in CDI could be further reduced by improving the materials and electrodes in order to boost the electrosorption capacity.

In the last decade, the numbers of articles and patents related to CDI technology have shown exponential growth, especially concerning electrode materials [131]. Considering that CDI electrodes require similar properties as supercapacitors, most of the materials reported in the literature have been carbon-based, such as graphene [85], conductive polymers [109], nitrogen-doped carbon aerogel [132], and oxide-coated carbons [133]. Carbons are preferred for CDI due to their high specific surface area available for electrosorption, electrical conductivity suitable for a fast charge/discharge response, and usually low cost [134]. However, although many studies have addressed carbon preparation, much less attention has been paid to electrode preparation.

In previous work by our group, Zornitta et al. [52] demonstrated that polyaniline-activated carbon (PAC) can be successfully employed as an electrode material for CDI desalination. Besides the low cost of the monomer and easy synthesis, the high nitrogen content of polyaniline (~15 wt.%) provides pyridine- and pyrrole-like nitrogen groups that create pseudocapacitance [85] and improve carbon wettability. Furthermore, the properties of polyaniline (PAni) can be easily customized by varying the doping anion during the polymerization process [102]. Zornitta et al. [52] successfully synthesized PAC derived from PAni doped with different anions, obtaining the highest salt adsorption capacity using p-toluenesulfonate-doped PAni as precursor (PAC/PTS). Given that the SAC of PAC/PTS (22.2 mg g<sup>-1</sup> at 1.2 V) is among the highest values reported for CDI desalination using carbon electrodes, this material was selected in the present work.

In general, CDI electrodes are prepared by blading or spray-coating a mixture of carbon and binders onto a current collector [135–138]. Additionally, efforts have been made to prepare free-standing electrodes using binders [119,139,140], or binder-free electrodes such as carbon cloth [41], carbon nanotube sponges [141], and 3D graphene mesh [142]. The electrodes most widely employed for CDI are those supported on current collectors produced by the doctor-blading procedure, using polyvinylidene difluoride (PVDF) as binder, as well as free-standing electrodes produced using polytetrafluoroethylene (PTFE). Recently, Wu et al. [140] reported the preparation of a free-standing activated carbon electrode using phenol resin binder to obtain a 2.0 mm thick electrode with good

electrical conductivity and hydrophilicity, but the  $SAC$  ( $8.9 \text{ mg g}^{-1}$ ) was very low. The effect of electrode thickness has not been discussed, despite its contribution to mechanical stability and its effects on the electric and mass transfer properties.

In the present work, we describe a different technique for obtaining free-standing electrodes, comparing these electrodes with others produced using doctor-blade casting. A comprehensive and systematic study of how the textural and electrochemical properties affect the CDI performance is provided, including the effects of interparticle porosity ( $\varepsilon$ ) and electrode thickness ( $\zeta$ ). As far as we know, this is the first work to report experimental evidence of the importance of  $\varepsilon$  for overall CDI performance in terms of  $SAC$  and the kinetics of electrosorption and desorption. The desalination performance of the electrodes was evaluated in terms of salt adsorption capacity ( $SAC$ ) normalized by mass ( $SAC_M$ ) and volume ( $SAC_V$ ), charge efficiency ( $Q_E$ ), specific energy consumption ( $\eta$ ), and electrosorption/desorption kinetics. Given that the thickness and the preparation procedure directly affect the textural and electrochemical properties of these electrodes, the findings of this work enable a better understanding of ways to tune the electrode preparation technique, in order to optimize the CDI desalination process.

## 2.2. Materials and Methods

### 2.2.1. Materials

The aniline monomer (99%, Sigma-Aldrich) was distilled prior to polymerization and was maintained at a low temperature ( $<3 \text{ }^\circ\text{C}$ ) to prevent oxidation. The compounds p-toluenesulfonic acid monohydrate (HPTS,  $\geq 98.5\%$ , Sigma-Aldrich) and ammonium persulfate (98%, Synth) were used as doping anion source and oxidant to promote polymerization, respectively. Potassium hydroxide (KOH, Sigma-Aldrich) was used for chemical activation. The electrodes were prepared using polyvinylidene fluoride (PVDF, Sigma-Aldrich) and polytetrafluoroethylene (PTFE, 60 wt.%, Sigma-Aldrich) as binders and n-methylpyrrolidone (NMP, 99.5%, Synth) and ethanol (Sigma-Aldrich) as solvents.

### 2.2.2. Activated carbon and electrode preparation

PAni was chemically synthesized using the optimized conditions described by Jelmy et al. [143], with adaptations. Briefly, 10 mL of aniline was added to 500 mL of a  $0.3 \text{ mol L}^{-1}$  HPTS solution, under constant stirring at low temperature ( $3 \text{ }^\circ\text{C}$ ). The polymerization was started by adding 85.9 mL of the oxidant ( $1.0 \text{ mol L}^{-1}$   $(\text{NH}_4)_2\text{S}_2\text{O}_8$ ) into the monomer solution. The mixture was left to

react for 24 h, under stirring. After polymerization, the PTS-doped PANi was filtered, washed with deionized water, and dried in an oven at 60 °C for 24 h.

The polymer was carbonized and activated following the optimized conditions reported by Zornitta et al. [112]. The material was firstly carbonized at 500 °C for 2 h in a tubular furnace (Lindberg Blue M, Thermo Scientific), using a heating rate of 10 °C min<sup>-1</sup>, under an atmosphere of N<sub>2</sub> (150 mL min<sup>-1</sup>). After carbonization, the material was mixed with KOH pellets (KOH:carbonized material mass ratio of 4:1) and a small amount of distilled water (~10 mL), followed by drying overnight in an oven at 105 °C. After drying, the material was activated at 850 °C for 1.5 h, using the same heating rate and N<sub>2</sub> flow conditions as in the carbonization step. The resulting activated carbon was washed with 0.5 mol L<sup>-1</sup> HCl solution (Sigma-Aldrich), followed by distilled water (60 °C) until constant pH, and was then dried at 105 °C for 24 h.

Based on previous studies [144–146], the amounts of PVDF and PTFE were established as the minimum necessary to ensure mechanical stability of the electrode and minimize loss of capacity. The blade-casting electrodes were prepared by mixing together 5 wt.% of PVDF (previously dissolved in NMP) and 95 wt.% of activated carbon. The resulting slurry was spread onto a graphite sheet substrate (PES-15, thickness = 0,4 mm, GES-AGM) using a doctor-blade machine (Fig. 2.1). The carbon films were formed after evaporating the solvent in an oven at 80 °C for 24 h.

The free-standing electrodes were prepared by mixing 95 wt.% of activated carbon and 5 wt.% of PTFE. Firstly, the activated carbon was mixed with ethanol to obtain a homogeneous slurry. After adding PTFE, the mixture was kneaded and then rolled out using a rolling machine (Atlas 150, Marcato) to obtain free-standing carbon electrodes. Finally, the electrodes were dried in an oven at 120 °C for 24 h.

The electrodes with different thicknesses produced by the doctor-blade (DB) and free-standing (FS) methods were labeled as DB- $\zeta$ , and FS- $\zeta$ , where  $\zeta$  represents the thickness ( $\mu\text{m}$ ) of the dry carbon film. The prepared electrodes are shown in Fig. 2.2.

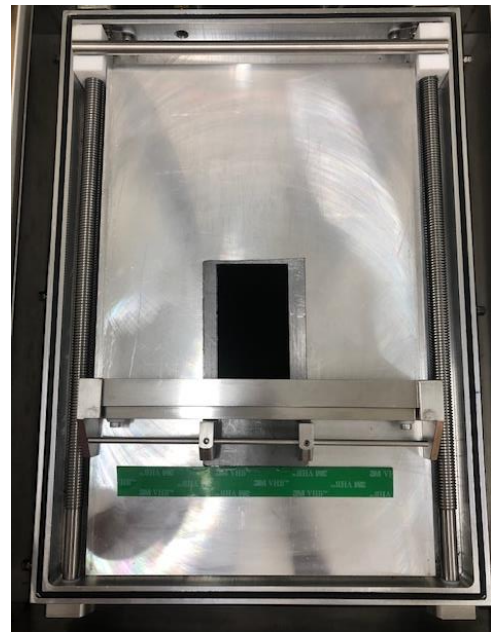
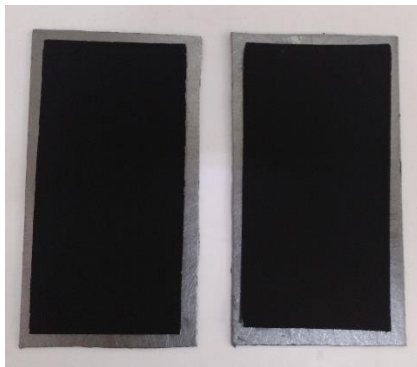


**Fig. 2.1.** Doctor-blade device.



(a)



(b)

**Fig. 2.2.** Blade-casting (a) and free-standing (b) electrodes.

### 2.2.3. Characterizations

#### 2.2.3.1. Textural characterizations

The contact angle ( $\theta$ ), indicating the hydrophobicity or hydrophilicity of the carbon electrodes (i.e., their wettability), was measured according to the sessile drop method described by Lee et al. [147]. Briefly, one drop of water was deposited on the electrode surface and the angle formed between the electrode surface and the water was measured after 10 s, using ImageJ software. After 20 s, the drop was completely absorbed into the electrode.

Scanning electron microscopy (SEM) images of the different electrodes were obtained using a JEOL JEM 2010 microscope. In order to determine the specific surface area (SSA) and pore size

distribution (PSD) of the carbons, assays of the adsorption/desorption of nitrogen at  $-196\text{ }^{\circ}\text{C}$  were carried out using a Micrometitics ASAP 2420 instrument. Prior to the measurements, the samples were degassed at  $90\text{ }^{\circ}\text{C}$  and  $150\text{ }^{\circ}\text{C}$  for 60 min and 720 min, respectively. The SSA was calculated by the Brunauer-Emmett-Teller equation ( $SSA_{BET}$ ), using the linear region of the isotherm. The 2D-NLDFT heterogeneous surface model was employed to calculate the PSD, total pore volume ( $V_T$ ), and SSA ( $SSA_{DFT}$ ), using SAIEUS software. The total pore volume was determined from the cumulative pore size distribution, while the volume of mesopores ( $V_{mes}$ ) was calculated as the difference between  $V_T$  and the volume of micropores ( $V_{mic}$ ).

### 2.2.3.2. Electrochemical characterizations

Cyclic voltammetry (CV), galvanostatic charge-discharge (GCD) measurements, and electrochemical impedance spectroscopy (EIS) were performed using a potentiostat (PGStat 204, Autolab) and a three-electrode cell. Two carbon electrodes were used as working and counter electrodes, together with an Ag/AgCl( $\text{KCl}_{\text{sat}}$ ) reference electrode. The mass of the counter electrode was three times greater than that of the working electrode.

Cyclic voltammograms were recorded at a scan rate ( $v$ ) of  $25\text{ mV s}^{-1}$ , between  $-0.2\text{ V}$  and  $0.5\text{ V vs. Ag/AgCl(KCl}_{\text{sat}})$ , which was previously determined as the potential window to avoid redox reactions. The specific capacitance ( $C_S$ ) of the electrodes ( $\text{F g}^{-1}$ ) was calculated using Eq. (2.1), where  $I$  is the current (A) and  $m$  is the mass (g) of the active material in the working electrode.

$$C_S = \frac{I}{v \cdot m} \quad (2.1)$$

The GCD measurements were performed at  $1\text{ A g}^{-1}$ . In this case, the specific capacitance ( $C_{CD}$ ) was calculated from the slope of the discharge curve using Eq. (2.2), where  $I_d$  is the discharge current (A),  $\Delta t$  is the discharge time (s), and  $\Delta E$  (V) is the potential difference after discharge, subtracting the ohmic drop. The lower and upper potential limits were  $-0.2\text{ V}$  and  $0.5\text{ V vs. Ag/AgCl (KCl}_{\text{sat}})$ .

$$C_{CD} = \frac{I_d \cdot \Delta t}{m \cdot \Delta E} \quad (2.2)$$

The converted deionization capacity ( $D_c$ ) was calculated using Eq. (2.3), where  $E_{\text{cell}}$  is the cell potential in the electrosorption step (V),  $F$  is the Faraday constant ( $96485\text{ C mol}^{-1}$ ), and  $M_{\text{NaCl}}$  is the molecular weight of NaCl ( $58440\text{ mg mol}^{-1}$ ).

$$D_c = C_{CD} \cdot E_{\text{cell}} \frac{M_{\text{NaCl}}}{4 \cdot F} \quad (2.3)$$

EIS measurements were carried out in the frequency range between 1 mHz and 10 kHz, applying a potential of 0.0 V and an AC amplitude of 10 mV. The fitting for the equivalent circuit was performed using Metrohm Autolab NOVA v2.1 software, in order to obtain the values of the specific capacitance and the charge and mass transfer resistances.

The CV, GCD, and EIS experiments were performed in  $1.0 \text{ mol L}^{-1}$  NaCl. This high salt concentration was chosen to prevent ion diffusion limitation during the measurements [43].

## 2.2.4. Desalination

A schematic illustration of the CDI cell used in the desalination experiments is shown in Fig. 2.3(a). The cell consisted of two acrylic plates, a pair of carbon electrodes ( $2.0 \text{ cm} \times 2.3 \text{ cm}$ ), and graphite plates as current collectors. A plastic mesh (1 mm of thickness) placed between the carbon electrodes provided the gap necessary to avoid short circuit and allow flow of the electrolyte. Rubber gaskets were used to seal the cell. All the components were assembled using nuts and bolts.

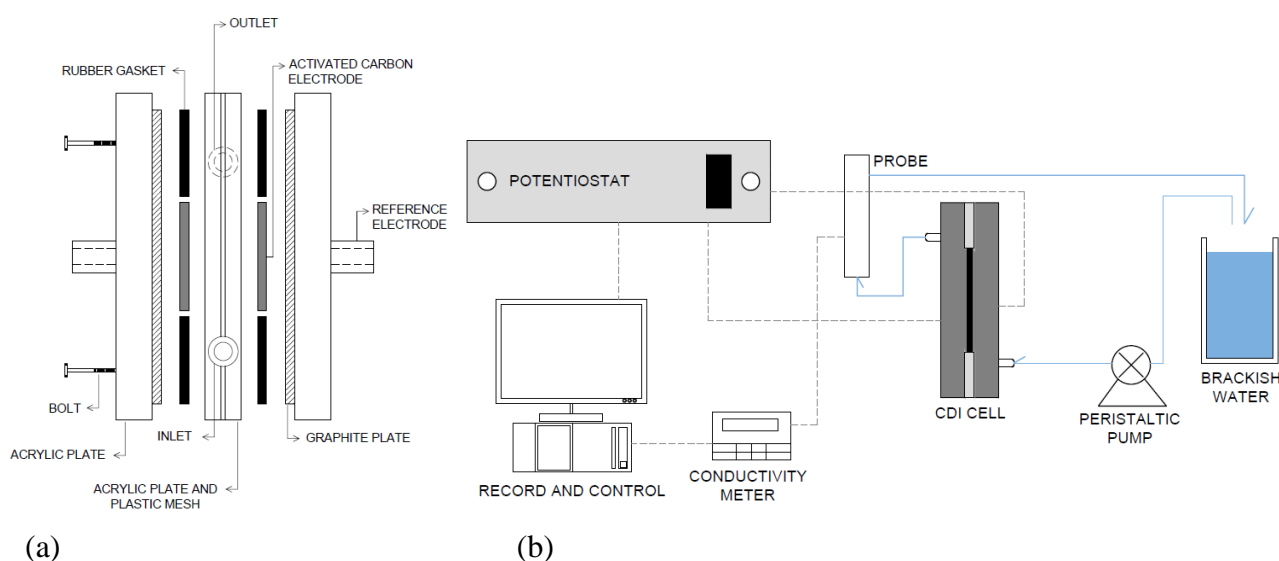


**Fig. 2.3.** Schematic illustrations of the CDI cell (a) and the desalination setup (b).

Desalination was performed using a quasi-single-pass process (Fig. 2.3(b)). Briefly, the electrolyte ( $600 \text{ mg L}^{-1}$  NaCl) was pumped from a reservoir (2 L) through the system by a peristaltic pump (Masterflex L/S, Cole-Parmer), at a constant flow rate of  $10 \text{ mL min}^{-1}$ . The high ratio between the volume of electrolyte and mass of carbon ensured that the change in concentration of the inflow water stream was negligible during the desalination. A potentiostat (PGStat 204, Autolab) provided constant cell potentials of 1.2 V and 0.0 V during the electrosorption and desorption steps, respectively. Each experiment was carried out for 15 cycles, with half-cycles of 30 min. The solution conductivity and pH were measured online at the exit of the cell and were recorded every 3 s, using a Seven Excellence instrument (Mettler Toledo).

The electrosorption performance was evaluated in terms of the salt adsorption capacity normalized by mass ( $SAC_M$ ) and volume ( $SAC_V$ ), the average salt adsorption capacity ( $ASAR$ ), the



charge efficiency ( $Q_E$ ), and the specific energy consumption ( $\eta$ ), calculated using the Eqs. (2.4) to (2.8), respectively.

$$SAC_M = \frac{\dot{V} \cdot \int_{t_1}^{t_2} C(t) dt}{m_E} \quad (2.4)$$

$$SAC_V = \frac{\dot{V} \cdot \int_{t_1}^{t_2} C(t) dt}{V_E} \quad (2.5)$$

$$ASAR = \frac{SAC_M}{t_c} \quad (2.6)$$

$$Q_E(\%) = 100 \frac{z \cdot F \cdot m_E \cdot SAC_M}{M_{NaCl} \int_{t_1}^{t_2} I_e dt} \quad (2.7)$$

$$\eta = \frac{E_{cell} \int_{t_1}^{t_2} I dt}{m_{rem}} \quad (2.8)$$

In these equations,  $\dot{V}$  is the volumetric flow rate of the electrolyte ( $L \text{ min}^{-1}$ ),  $C(t)$  is the concentration at time  $t$  ( $mg \text{ L}^{-1}$ ),  $t_1$  and  $t_2$  give the electrosorption time interval (min),  $m_E$  is the total mass of active material in both electrodes (g),  $V_E$  is the volume of both electrodes ( $cm^3$ ),  $t_c$  is the duration of the charging step (s),  $z$  is the ion valence, and  $m_{rem}$  is the quantity of ions removed from the solution (mg). The current ( $I_e$ ) in Eq. (2.7) is the effective current used for electrosorption (not considering the leakage current), while the current ( $I$ ) in Eq. (2.8) is the total current applied to the cell. The  $SAC$  was calculated as an average value from the adsorption and desorption steps. Finally, the optimized salt removal (OSR) method adapted from Zornitta and Ruotolo [111] was also used to investigate the electrosorption capacity and the electrosorption and desorption kinetics.

### 2.3. Results and Discussion

The visual observation of the electrodes after preparation shows that the thinner electrode prepared by the DB technique had smooth and uniform surfaces, without any apparent cracks, while the thicker DB electrode presented small cracks. These cracks were attributed to the rigidity of the PVDF and were only apparent in the thicker electrode due to the greater amount of solvent that evaporated through a longer path during the drying step of electrode preparation [148]. On the other hand, the free-standing electrodes, independent of the thickness, had smooth and uniform surfaces, without the presence of cracks. It should be noted that attempts to separate the effects of the binder and electrode thickness, by preparing DB and FS electrodes using PTFE and PVDF, respectively, were not successful. These electrodes were not mechanically stable, even using different ratios of binder and activated carbon.

### 2.3.1. Textural characterizations

The SEM images of the cross-sectional areas of the electrodes (Fig. 2.4(a)-(d)) were used to determine the electrode film thicknesses (Table 2.1). The images revealed uniform thicknesses, but with evident differences in the interparticle porosity ( $\varepsilon$ ), which was further confirmed by higher magnification micrographs of the top view images (Fig. 2.4(e)-(f)) and the cross-sectional area (Fig. 2.4(g)-(j)). The free-standing films were clearly more compact than the blade-casting films, with fewer voids. The SEM images were binarized using Image-Pro Plus 7 software and the white and black areas (Fig. 2.5) were used to estimate the film porosity. According to Table 2.1,  $\varepsilon$  was not influenced by the electrode thickness, but depended on the preparation procedure. Two factors could explain the greater hydrophilicity of the DB electrodes: i) higher  $\varepsilon$ , since the pores in the electrode are beneficial for storing and buffering the electrolyte [142]; and ii) the hydrophilicity of the binder, since the contact angles of water on PVDF and PTFE are  $84.5^\circ$  [149] and  $113^\circ$  [150], respectively. These effects would strongly influence the desalination kinetics. The film thickness did not appear to significantly affect the electrode wettability. All the electrodes were hydrophilic, mainly because the PAC/PTS had a high content of surface oxygen groups, including hydroxyl, carboxyl, and carbonyl species, resulting from the activation of polyaniline by KOH [112].

**Table 2.1.** Thicknesses, interparticle porosities, and contact angles of the electrodes.

Electrode	$\zeta$ ( $\mu\text{m}$ )	$\varepsilon$	$\theta$
<b>DB-320</b>	$320 \pm 3$	0.64	$61^\circ$
<b>DB-402</b>	$402 \pm 3$	0.62	$67^\circ$
<b>FS-282</b>	$282 \pm 8$	0.55	$78^\circ$
<b>FS-359</b>	$359 \pm 9$	0.56	$79^\circ$

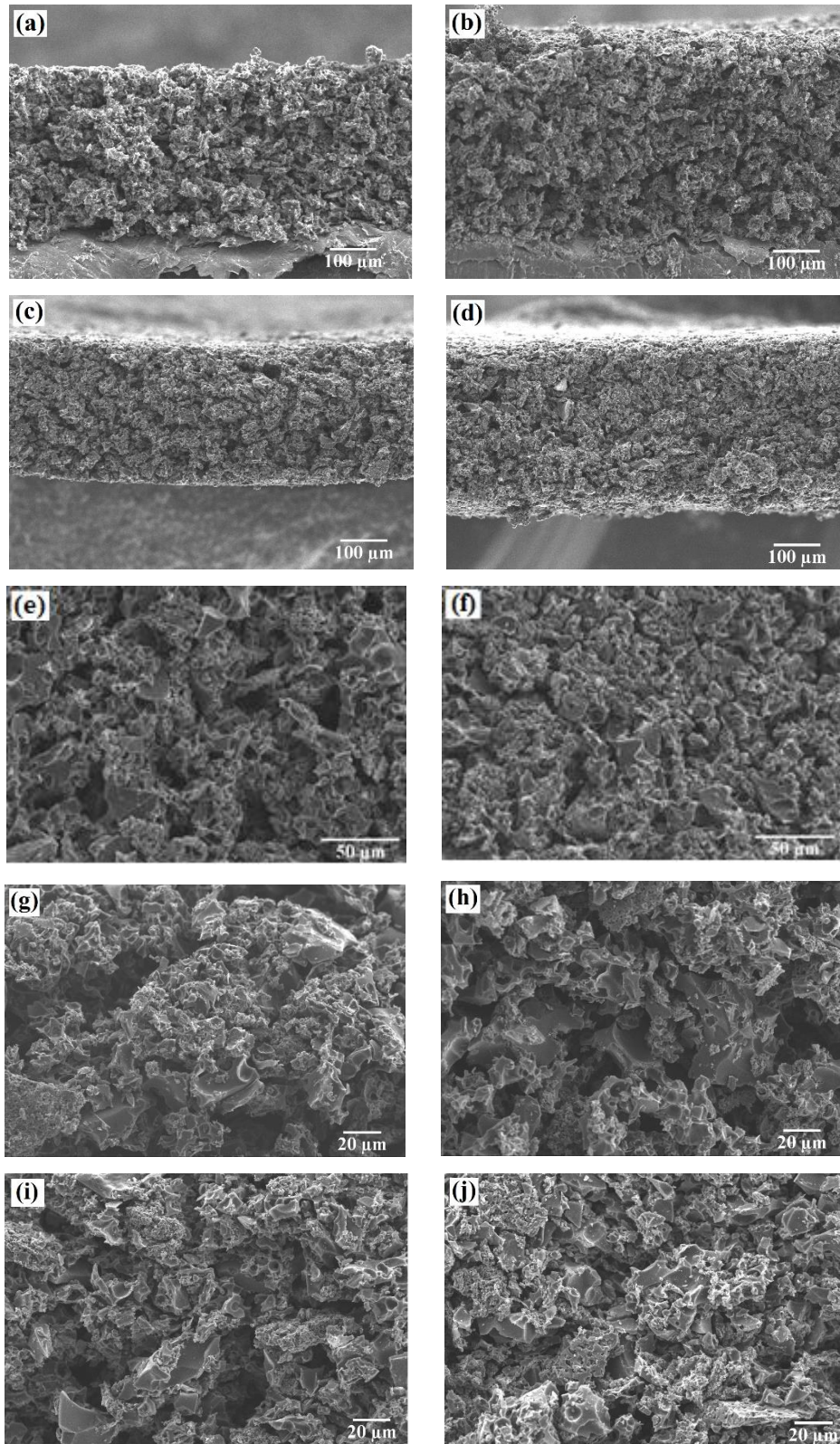


**Fig. 2.4.** SEM images of the cross-sectional areas of the DB-320 (a), DB-402 (b), FS-282 (c), and FS-359 (d) electrodes. Top views of the DB-320 (e) and FS-282 (f) electrodes. Cross-sectional views of the DB-320 (g), DB-402 (h), FS-282 (i), and FS-359 (j) electrodes.

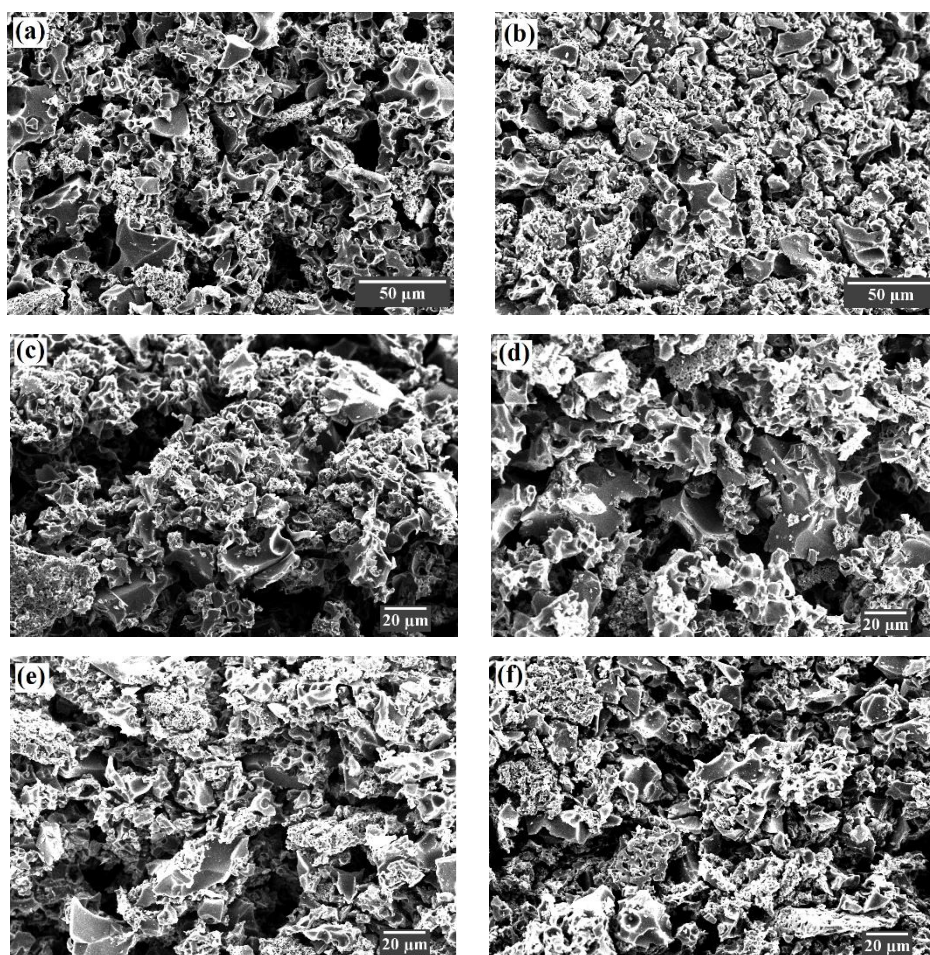


**Fig. 2.5.** Binarized black and white SEM micrographs produced using Image-Pro Plus 7. Top views of the DB-320 (a) and FS-282 (b) electrodes. Cross-sectional views of the DB-320 (c), DB-402 (d), FS-282 (e), and FS-359 (f) electrodes.

The nitrogen adsorption-desorption isotherms and the corresponding pore size distributions for the PAC/PTS and the electrodes are shown in Fig. 2.6. The adsorption isotherms were type I, according to the IUPAC classification, suggesting a predominance of micropores. The type H4 hysteresis at higher pressures indicated a contribution of mesopores. As can be seen in Fig. 2.6(b), all the samples presented two pore size ranges, with peaks at 0.63 and 1.90 nm, confirming the predominance of micropores and also revealing the presence of mesopores. Table 2.2 summarizes the textural properties of the PAC and the electrodes, determined from the nitrogen adsorption-desorption isotherms. It is important to note the high  $SSA$  of PAC ( $SSA_{BET} = 2869 \text{ m}^2 \text{ g}^{-1}$ ), even when calculated using the 2D-NLDFT model ( $SSA_{DFT} = 2285 \text{ m}^2 \text{ g}^{-1}$ ). Although the  $SSA_{DFT}$  values were lower than the  $SSA_{BET}$  values, they were still high when compared to other activated carbons reported in the literature [151–154].

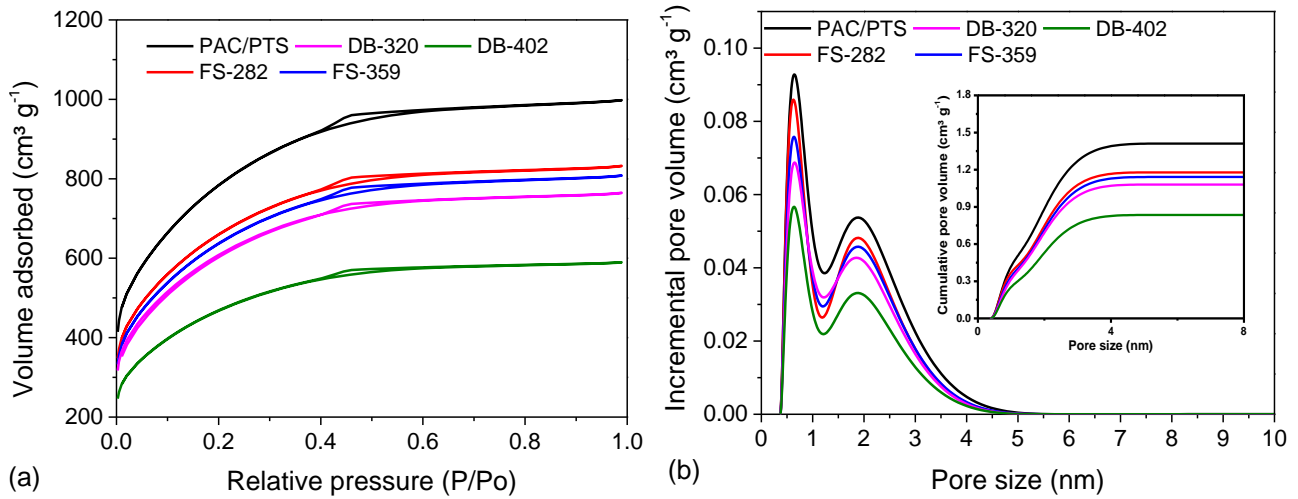


**Fig. 2.6.** Nitrogen adsorption-desorption isotherms (a) and pore size distributions (b) of the PAC/PTS and the DB-320, DB-402, FS-282, and FS-359 electrodes.

**Table 2.2.** Electrode characteristics obtained from the N<sub>2</sub> adsorption-desorption isotherms:  $SSA_{BET}$ ,  $SSA_{DFT}$ , volume of pores ( $V_T$ ), volume of micropores ( $V_{mic}$ ), volume of mesopores ( $V_{mes}$ ), and percentage of mesopores ( $\%V_{mes}$ ).

Material	$SSA_{BET}$ (m <sup>2</sup> g <sup>-1</sup> )	$SSA_{DFT}$ (m <sup>2</sup> g <sup>-1</sup> )	$V_T$ (cm <sup>3</sup> g <sup>-1</sup> )	$V_{mic}$ (cm <sup>3</sup> g <sup>-1</sup> )	$V_{mes}$ (cm <sup>3</sup> g <sup>-1</sup> )	$\%V_{mes}$	$V_{mic}/V_{mes}$
<b>PAC/PTS</b>	2869	2285	1.42	0.87	0.55	38	1.58
<b>DB-320</b>	2225	1748	1.08	0.68	0.40	37	1.70
<b>DB-402</b>	1714	1367	0.84	0.52	0.32	37	1.63
<b>FS-282</b>	2417	1960	1.18	0.74	0.44	38	1.68
<b>FS-359</b>	2326	1850	1.15	0.71	0.44	38	1.61

As expected, the use of binders negatively affected the  $SSA$  and pore volume, since they blocked the pores, in most cases leading to a loss of 15-25% of these properties (see Fig. 2.7), while a loss of ~40% was observed for the DB-402 electrode. The FS electrodes were less prone to pore clogging, compared to the DB electrodes (Table 2.2, Fig. 2.7). It is important to note that many studies reported in the CDI literature have found correlations between desalination performance and the textural properties of the carbon material, instead of the electrode. Considering that both the electrode preparation procedure and the electrode thickness influence the textural properties, it would be more appropriate to discuss the effects of these properties in terms of the electrode  $SSA$  and pore volume.

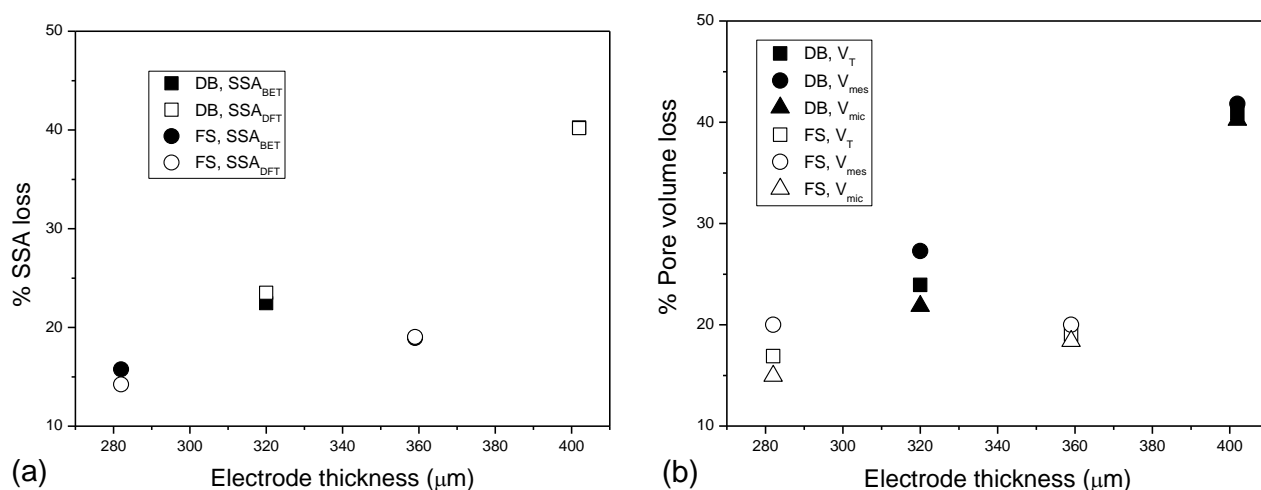


**Fig. 2.7.** Percentage losses of SSA (a) and  $V_T$  (b) after electrode preparation.

Another interesting finding concerned comparison of the values of SSA,  $V_T$ , and %  $V_{mes}$  obtained for the PAC/PTS in this work with those obtained by Zornitta et al. [112] ( $SSA_{BET} = 3649 \text{ m}^2 \text{ g}^{-1}$ ;  $SSA_{DFT} = 2470 \text{ m}^2 \text{ g}^{-1}$ ;  $V_T = 2.30 \text{ cm}^3 \text{ g}^{-1}$ ; %  $V_{mes} = 66$ ). Although the same polymer, carbonization procedure, and KOH activation procedure were used, the dry impregnation of KOH was replaced by wet impregnation, which resulted in inferior textural properties. This difference revealed the important influence of the impregnation method employed prior to PAC/PTS activation.

### 2.3.2. Electrochemical characterizations

The cyclic voltammograms recorded at  $25 \text{ mV s}^{-1}$  (Fig. 2.8(a)) displayed similar capacitances and quasi-rectangular shapes, without evidence of redox peaks, indicating that all the electrodes were highly capacitive and conductive. It has been demonstrated that the capacitance obtained from galvanostatic charge-discharge measurements is better able to predict the electrosorption trend in terms of SAC [52,155], so GCD data were recorded at  $1 \text{ A g}^{-1}$ . Fig. 2.8(b) shows a symmetrical triangular shape, typical of capacitors with reversible non-Faradaic processes and low internal resistance. The highest capacitance was obtained for FS-359 ( $151 \text{ F g}^{-1}$ ), followed by FS-282 ( $141 \text{ F g}^{-1}$ ), DB-402 ( $134 \text{ F g}^{-1}$ ), and DB-320 ( $119 \text{ F g}^{-1}$ ). The  $IR_{drop}$  values for all the electrodes were in the range 10-20 mV, revealing the low values for the contact resistance between electrode and current collector, the solution resistance, the electrode resistivity, and the mass transfer resistance [156].

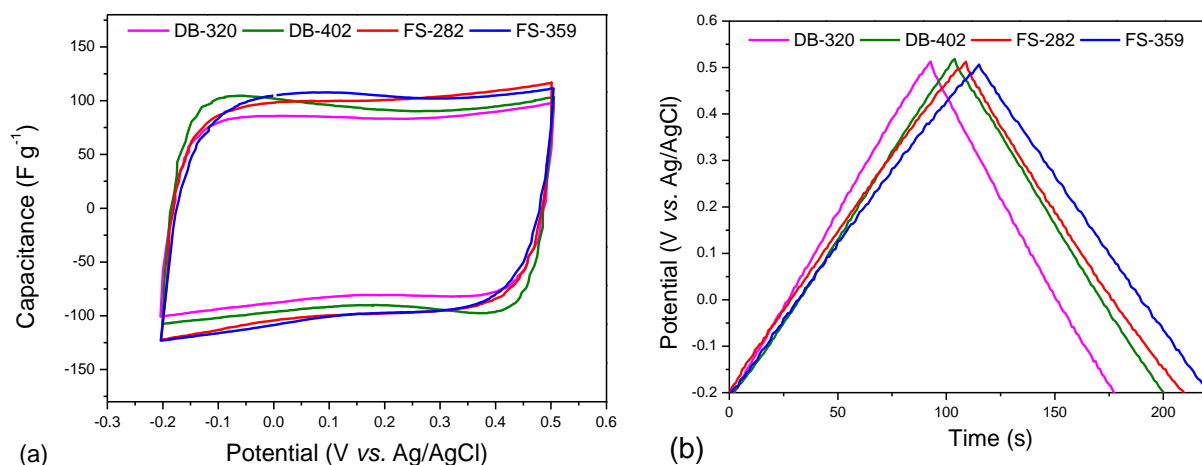


**Fig. 2.8.** (a) Cyclic voltammograms acquired at  $25 \text{ mV s}^{-1}$  and (b) GCD profiles obtained at  $1 \text{ A g}^{-1}$ . Electrolyte:  $1 \text{ mol L}^{-1} \text{ NaCl}$ .

Although a relation between GCD capacitance and  $SSA$  (or  $V_T$ ) was not observed (Fig. 2.9), the electrode capacitance was affected by the preparation procedure and the film thickness. The FS electrodes displayed the highest surface areas and had higher capacitances, compared to the DB electrodes, although  $C_{CD}$  was lower for the thinner electrode, despite its higher surface area. Accordingly, lower capacitances were observed for the DB electrodes, since they presented lower surface areas, with the capacitance again being lower for the thinner electrode, despite its higher surface area. These results suggested that properties other than  $SSA$  strongly influenced the capacitance. Therefore, EIS analyses were performed to investigate the capacitance and series resistances of the porous electrodes.

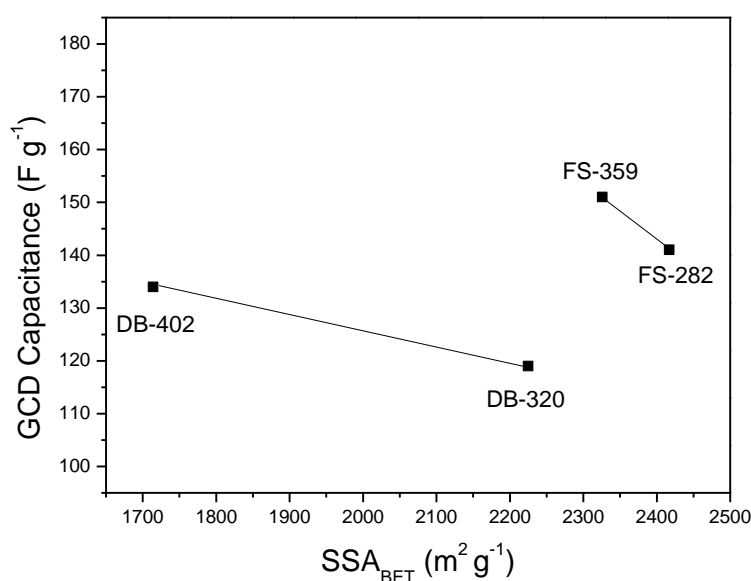


**Fig. 2.9.** GCD capacitance vs.  $SSA_{BET}$  for the DB and FS electrodes.

According to the Nyquist plots shown in Fig. 2.10(a), the electrodes behaved as typical electrochemical supercapacitors, with a semi-circle representing the charge transfer domain at high frequencies and a line representing the mass transfer region at low frequencies [157]. A modified Randle equivalent circuit (inset of Fig. 2.10(b)) was fitted to the Nyquist plot. The circuit elements (Table 2.3) included an ohmic resistance ( $R_{\Omega}$ ), due to the current collector and electrolyte resistances; a charge transfer resistance ( $R_{CT}$ ), which is an intrinsic property of the carbon electrode; a Warburg element ( $W$ ), which concerns the effect of ion migration inside the carbon pores; a capacitance at the electrolyte/electrode interface ( $C_1$ ); and a capacitance developed inside the micropores of the carbon electrode ( $C_2$ ). Fig. 2.10(b) shows the EIS capacitance as a function of frequency. At high frequencies, the capacitances were very low and almost constant, due to the predominance of the ohmic resistance, since the ions did not have sufficient time to reach the pores and be stored in the EDL. As the frequency decreased, the ions reached the micropores and the capacitances attained their maximum values.

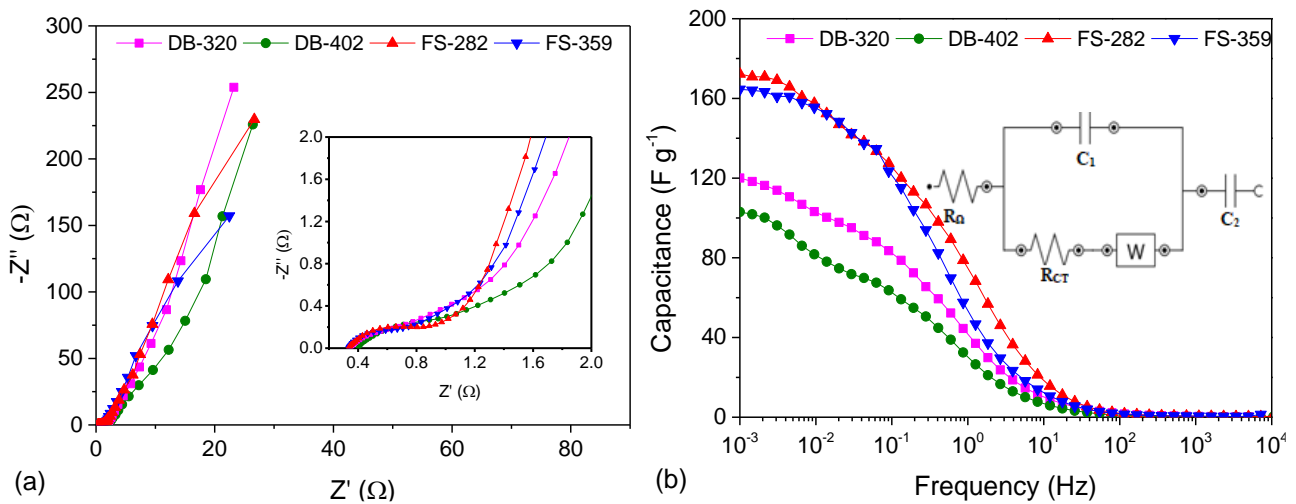


**Fig. 2.10.** (a) Nyquist plots and (b) plots of capacitance against frequency (inset: modified Randle equivalent circuit). Electrolyte: 1.0 mol L<sup>-1</sup> NaCl; potential: 0.0 V; AC amplitude: 10 mV.

**Table 2.3.** EIS parameters obtained from the Nyquist plots and the modified Randle equivalent circuit.

Electrode	$R_{\Omega}$ (Ω) <sup>a</sup>	$R_{CT}$ (Ω) <sup>b</sup>	$R_{\Omega}$ (Ω)	$R_{CT}$ (Ω)	$A_o$ (mS s <sup>1/2</sup> )	$C_1$ (F/g)	$C_2$ (F/g)
<b>DB-320</b>	0.34	0.65	0.38	0.36	544	0.66	131
<b>DB-402</b>	0.39	1.05	0.45	0.50	478	0.31	111
<b>FS-282</b>	0.34	0.63	0.37	0.44	814	0.61	185
<b>FS-359</b>	0.33	0.46	0.36	0.37	897	0.75	192

<sup>a,b</sup> These values of  $R_{\Omega}$  and  $R_{CT}$  were obtained from the first and second intersections of the semi-circle with the abscissa, respectively.



As expected, the values of  $R_{\Omega}$  were similar, since all the measurements were carried out using the same three-electrode cell and experimental conditions, corroborating the low  $IR_{drop}$  observed in the GCD experiments. The values of  $R_{CT}$  were also very low, indicating a good electrode polarization.

It is interesting to note that there was a clear relation between the EIS capacitance ( $C_2$ ) and  $R_{CT}$ , as shown in Fig. 2.11. The capacitance decreased as  $R_{CT}$  increased, demonstrating that the performance of the electrode was influenced by many other variables, additional to the textural properties. Previously, Zornitta et al. [52] showed that the presence of highly polar surface groups was crucial to ensure satisfactory electrode wettability and CDI performance. It was found that although the PAC obtained from Cl-doped polyaniline had the highest surface area, this property was not sufficient to overcome the deleterious effects of electrode resistivity (including  $R_{CT}$ ) and insufficient oxygen surface groups to provide superior CDI performance. The results obtained (Fig. 2.11) also confirmed the importance of the electrode preparation procedure in determining the electrochemical performance, with the FS electrodes presenting better performance, due to both lower  $R_{CT}$  and higher SSA. The admittance element ( $A_0$ ), which is the inverse of the Warburg impedance, is an indication of how fast the ions diffuse inside the carbon micropores. The higher  $A_0$  of the FS electrodes could be attributed to their higher mesopores volume, which facilitates mass transfer and can have influence on the CDI kinetics.

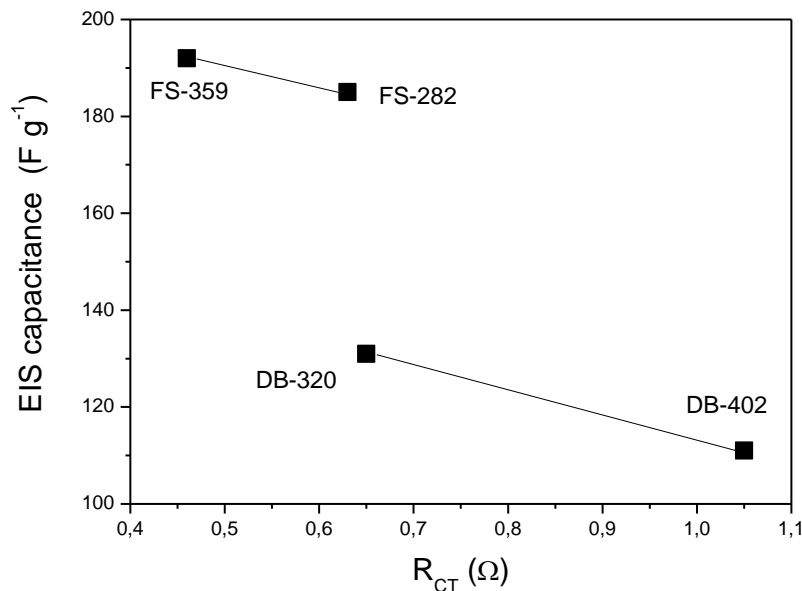


**Fig. 2.11.** EIS capacitance vs.  $R_{CT}$  for the DB and FS electrodes.

### 2.3.3. Electrosorption

The steady state desalination performances of the electrodes are shown in Fig. 2.12(a). In all cases, the adsorption-desorption was reversible, with faster charge-discharge for the DB electrodes. The results confirmed the high electrosorption capacity of PAC/PTS, attributed to its high conductivity, wettability, presence of oxygen surface groups, and pseudocapacitive behavior [52,112]. Although more salt was removed ( $m_R$ ) using the FS electrodes and the thicker electrodes of both types, because more active carbon ( $m_E$ ) was used for their preparation, the  $SAC_M$  values were similar, especially when the standard deviation was considered (Fig. 2.12(b), Table 2.4).

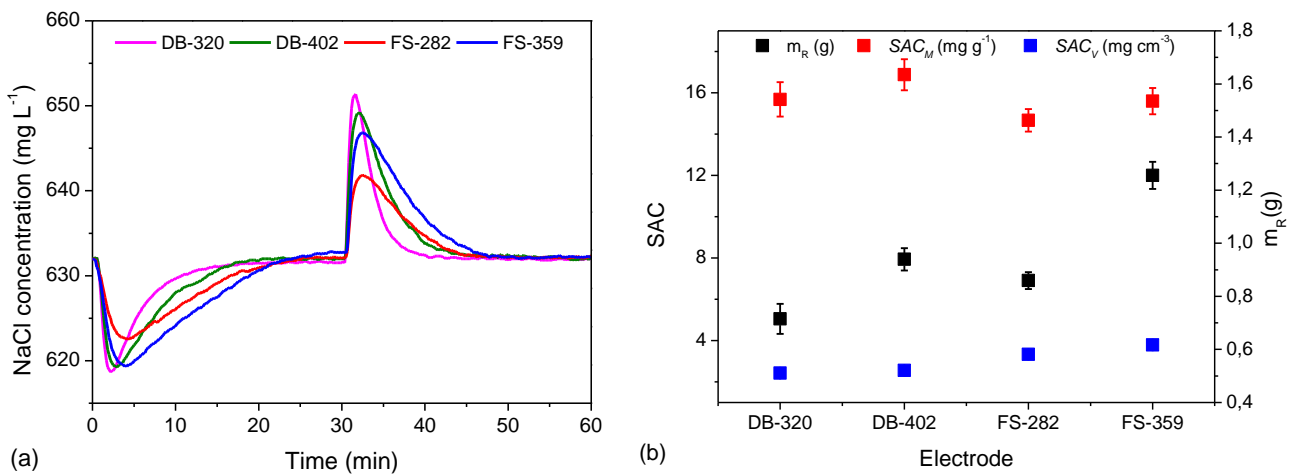


**Fig. 2.12.** Desalination performances (a) and the electrosorption responses  $m_R$ ,  $SAC_M$ , and  $SAC_V$  (b) for the different electrodes.  $E_{cell}$ : 1.2 V (adsorption) and 0.0 V (desorption); 632 mg L<sup>-1</sup> NaCl. The error bars were calculated considering the electrosorption/desorption cycles at the steady state desalination (achieved after 5 cycles).

**Table 2.4.** Total masses of active material ( $m_E$ ) and electrosorption performance parameters  $SAC_M$ ,  $SAC_V$ ,  $Q_E$ , and  $\eta$  for the different electrodes.

Electrode	$m_E$ (g)	$SAC_M$ (mg g <sup>-1</sup> )	$SAC_V$ (mg cm <sup>-3</sup> )	$Q_E$ (%)	$\eta$ (J mg <sup>-1</sup> )
DB-320	0.0456	15.7 ± 0.8	2.4 ± 0.2	73.8 ± 0.4	4.66 ± 0.37
DB-402	0.0556	16.9 ± 0.7	2.5 ± 0.1	82.6 ± 0.4	3.99 ± 0.23
FS-282	0.0586	14.7 ± 0.5	3.3 ± 0.1	81.8 ± 0.3	4.45 ± 0.24
FS-359	0.0803	15.6 ± 0.6	3.8 ± 0.2	95.5 ± 0.3	3.66 ± 0.19

Slightly superior  $SAC_M$  values were obtained for the DB electrodes, which was the opposite of the behavior observed in the GDC characterization, showing that the electrolyte concentration affected the EDL. Consequently, electrochemical characterizations carried out in concentrated electrolytes must be used cautiously for estimation of electrosorption performance. When the GCD capacitance was used to obtain  $D_c$  (i.e., the  $SAC_M$  if the capacitance was completely converted to salt electrosorption), the following trend was observed: FS-359 ( $27.4 \text{ mg g}^{-1}$ ) > FS-282 ( $25.6 \text{ mg g}^{-1}$ ) > DB-402 ( $24.3 \text{ mg g}^{-1}$ ) > DB-320 ( $21.6 \text{ mg g}^{-1}$ ). However, in diluted solutions, the  $SAC$  seldom corresponds to  $D_c$ , due to ohmic losses, Faradaic reactions, and ion transport limitations [158]. Furthermore, the current considered in the  $D_c$  calculation ignores the parasitic currents. Nevertheless, it is interesting to note that for the DB electrodes, approximately 70% of the value predicted by capacitance was achieved, while for the FS electrodes, the values were similar to those obtained by Zornitta et al. [52] (~57%).

Despite the lower  $SSA$  and higher  $R_{CT}$  observed for the DB electrodes, their slightly superior  $SAC_M$  values suggested that  $\varepsilon$  and  $\theta$  had important effects on the desalination performance, which would probably have been masked in the electrochemical characterization carried out using a concentrated electrolyte. In addition, the superior desalination performance expected for the FS electrodes was probably not achieved because of diffusional constraints in dilute solutions that restricted access to sub-nanopores (<1.0 nm), which were not available for electrosorption due to steric effects and EDL overlap phenomena [159,160]. These results reinforced that electrochemical characterizations should not be used alone to determine the feasibility of electrodes for CDI.

$SAC_M$  is an important parameter for comparing different materials and their effect on electrode cost. Here, since all the electrodes displayed similar  $SAC_M$ , the desalination performance was also analyzed in terms of  $SAC_V$ , a parameter directly related to the number of electrodes and the cell size required for a desalination process. The  $SAC_V$  values were in the order FS-359 > FS-282 > DB-402 > DB-320 (Fig. 2.12(b), Table 2.4). Coincidentally, this was the same order observed for the GCD capacitance. Since the FS preparation method produces denser electrodes, more ions could be removed using small CDI cells. Therefore, if the price of the activated carbon is not a hindrance, the FS electrode would be the best option for CDI, in order to achieve higher salt removal per cell. Here, the FS-359 electrode displayed the highest  $Q_E$  (Table 2.4), reflecting excellent reversibility and more effective EDL charging, which could be attributed to the low  $R_{CT}$  and probably a lower influence of co-ions [79,161], compared to the other electrodes.

It is possible that the lower  $Q_E$  values observed for the DB-320, DB-402, and FS-282 electrodes could also have been due to pH fluctuations during the desalination process, associated with Faradaic reactions involving water splitting and/or carbon oxidation [162]. However, the pH varied from 6.5 to 4.9, during electrosorption and desorption (Fig. 2.13), respectively, and in this

range, the pH has a minor influence on the electrolyte conductivity. Hence, the charge efficiency of these electrodes seemed to be mainly influenced by  $R_{CT}$ , since the effect of co-ions was present for all the electrodes [111]. Table 2.4 also displays the values of  $\eta$ , which include the leakage current, since it contributes to the overall energy consumption [18,52]. In this case, an opposite trend was observed for  $Q_E$ , which was expected because all the desalination experiments were carried out at constant cell potential. The low leakage currents observed for the DB (0.7 mA) and FS (0.8 mA) electrodes contributed to the low energy consumption values.

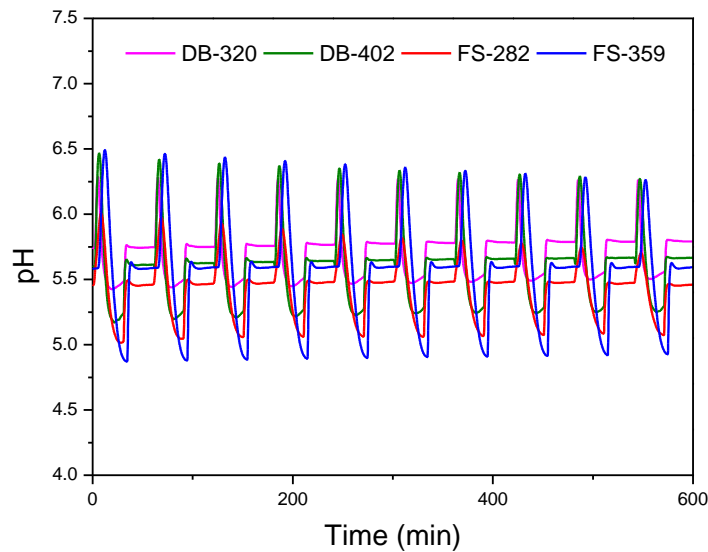


**Fig. 2.13.** Fluctuation of pH during the desalination cycles. Electrolyte:  $632 \text{ mg L}^{-1} \text{ NaCl}$ ;  $E_{cell}$ : 1.2 V (adsorption) and 0.0 V (desorption).

The CDI kinetics was firstly evaluated from the modified Ragone plot [163] displayed in Fig. 2.14. According to this plot, the DB electrodes provided the best CDI performance, since the corresponding points were located closer to the upper-right quadrant of the graph. The two FS electrodes presented similar behavior, with inferior performance mainly being due to the low  $ASAR$  values. Hence, contrary to the results obtained considering  $SAC_M$  alone, the simultaneous analysis of capacity and removal rate indicated that the DB electrodes combined the benefits of high capacity and fast kinetics.

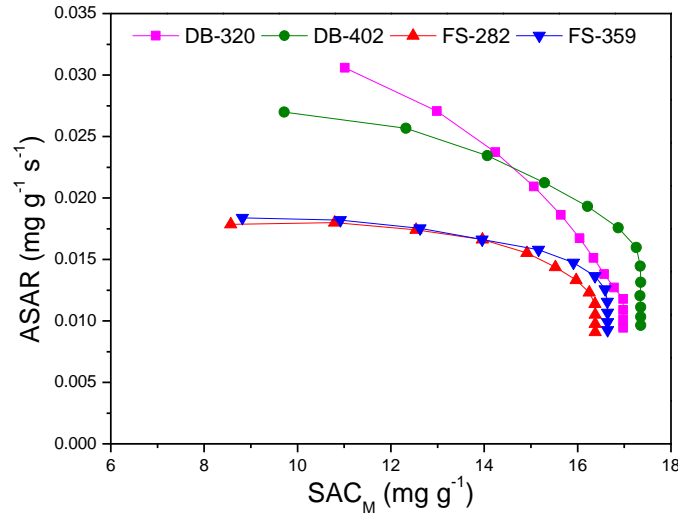


**Fig. 2.14.** ASAR as a function of  $SAC_M$  for the different electrodes.

Although the Ragone plot is a useful tool for the evaluation of kinetics and capacity, it was unable, for example, to indicate the best DB electrode, since the DB-320 and DB-402 electrodes presented different kinetic trends at the beginning and end of the electrosorption process. An additional drawback is that it does not consider the desorption kinetics. Therefore, instead of using a Ragone plot, Zornitta and Ruotolo [111] recently introduced the optimized salt removal (OSR) method as a new approach to evaluate the performance of a material in desalination, involving the simultaneous optimization of the electrosorption and desorption kinetics, and  $SAC$ . The  $OSR_M$  parameter gives the amount of salt removed per gram of electrode material per day of cell operation ( $\text{mg g}^{-1} \text{day}^{-1}$ ). Originally, the OSR method was developed considering a recirculating batch mode operation. In the present work, some modifications were introduced, since the desalination was carried out using single-pass operation. Accordingly, the electrosorption time ( $t_e$ ) and desorption time ( $t_d$ ) were determined as the times required to reach 630 and 634  $\text{mg L}^{-1}$  (Fig. 2.12(a)), respectively. The  $OSR_M$  values were calculated considering the number of cycles performed in one day, with  $m_E = 1.0 \text{ g}$ , while  $OSR_V$  values were also calculated, taking into account the volume of the carbon film (Table 2.5).

**Table 2.5.** Electrode  $OSR$  values, considering an operational time of one day.

Electrode	$t_e$ (min)	$t_d$ (min)	Number of cycles	$OSR_M$ ( $\text{mg g}^{-1} \text{day}^{-1}$ )	$OSR_V$ ( $\text{mg cm}^{-3} \text{day}^{-1}$ )
<b>DB-320</b>	10.9	6.5	82	1197	186
<b>DB-402</b>	14.1	9.6	60	974	147
<b>FS-282</b>	16.9	11.0	51	829	187
<b>FS-359</b>	19.0	13.4	44	739	180

In agreement with the Ragone plots, the DB electrodes showed superior performance. It could be seen that the fast kinetics presented by the DB-320 electrode at the end of the electrosorption was responsible for a shorter  $t_e$ , which together with a shorter  $t_d$  ensured that a high number of cycles could be performed, resulting in the best performance of this electrode. Interestingly, the difference between the electrodes was not so evident in terms of  $OSR_V$ . In this case, the slower kinetics of the FS electrodes was compensated by their higher capacity, since they were denser and could store a greater quantity of ions per unit volume.

The kinetics features of the FS and DB electrodes could not be explained by their textural properties, since all the electrodes presented similar  $V_{mes}$  and  $\%V_{mes}$ . Furthermore, the faster kinetics of the DB electrodes could not be ascribed to differences in mass transfer within micro- or mesopores, since higher admittances ( $A_0$ ) were observed for the FS electrodes. This suggested that the interparticle porosity of the DB electrodes was the main property affecting the electrode kinetics, since it facilitated mass transfer from the bulk solution to the mouths of the pores, consequently improving the mass transfer of ions to the particles and accelerating the electrosorption, which was further improved by the higher wettability of these electrodes. Greater thickness of the electrode led to slower diffusion throughout the electrode mass, so the best results were obtained using thin film electrodes. These results demonstrated the importance of designing cells that provide the best possible flows in the interparticle voids of the electrodes, in order to maximize mass transfer.

From a practical point of view, if the electrosorption and desorption kinetics are not considered, although the electrode thickness has a marginal impact on the amount of salt removed per gram of electrode, the narrow interparticle porosity obtained using the electrodes prepared by the free-standing method led to a higher  $SAC_V$  and a decrease of the cell dimensions. On the other hand, the more compact electrode hinders the kinetics, and fewer cycles can be performed considering the same operational time, as demonstrated by the OSR analysis. Accordingly, considering the production of  $1.0 \text{ m}^3 \text{ day}^{-1}$  of desalinated water from of a  $1000 \text{ mg L}^{-1}$  brackish water, the electrode areas required to achieve the palatable limit ( $500 \text{ mg L}^{-1}$ ) are estimated as 8.4, 8.4, 9.4, and  $7.8 \text{ m}^2$  for the DB-320, DB-402, FS-282, and FS-259 electrodes, respectively. The respective mass of active material required for desalination are 0.42, 0.51, 0.60, and 0.68 kg. Therefore, there is a compromise between the electrode area and mass of active material needed to achieve the same separation, and a cost analysis likely is determinant for the best choice.

## 2.4. Conclusions

A comparison between blade-casting and free-standing electrodes revealed the importance of the preparation procedure in determining the textural, electrochemical, and CDI properties of the electrodes. Although the  $SSA$ ,  $V_T$ , and  $R_{CT}$  values depended on the preparation procedure, the electrodes performed similarly in terms of  $SAC_M$  (14.7-16.9 mg g<sup>-1</sup>) for the desalination of brackish water, although the values for the DB electrodes were slightly superior. If  $SAC_V$  was the parameter considered, the FS electrodes outperformed the DB electrodes, because the carbon films were more compact and a large quantity of electroactive material was available. On the other hand, if the kinetics of electrosorption and desorption were considered, the high interparticle porosity of the DB electrodes provided faster mass transfer, which substantially decreased the cycle time and enabled a greater quantity of salt to be removed, as shown in the OSR analysis. This work brings as the main scientific conclusion the importance of tuning the electrode porosity to enhance mass transfer or improve salt electrosorption capacity, thus paving the way to obtain optimized electrodes, specially aiming future application in flow-through CDI cells.

Blade-casting seems to be the best electrode preparation method for CDI applications involving aqueous diluted salt electrolytes, since it produces electrodes with superior  $OSR_M$ , due to faster electrosorption and desorption kinetics. However, it should be considered that in small CDI cells, a higher amount of salt can be removed using FS electrodes. Therefore, if the material cost is not a constraint, the maximum possible amount of salt could be removed using compact FS electrode CDI cells. Finally, the trends observed in this work also impact the specific energy consumption since the required energy to obtain 1.0 m<sup>3</sup> day<sup>-1</sup> of desalinated water, considering a concentration drop from 1.0 to 0.5 g L<sup>-1</sup>, can be reduced from 0.65 to 0.51 kWh using the DB-320 to FS-359 electrodes, respectively. This drop of 21.5% is due to the  $SAC_V$  improvement from 2.4 (DB-320) to 3.8 (FS-359) mg cm<sup>-3</sup>, thus revealing the importance of the electrode design not only for electrosorption, but also to minimize the energy requirements.

## CHAPTER 3

### EFFICIENT AND STABLE OPERATION OF CAPACITIVE DEIONIZATION ASSESSED BY ELECTRODE AND MEMBRANE ASYMMETRY

Capacitive deionization (CDI) is an electrochemical technology emerging as a cost-effective alternative for desalination of brackish water. Despite the remarkable advances in terms of salt adsorption capacity ( $SAC$ ) and charge efficiency ( $Q_E$ ), there are still challenging issues concerning the electrode stability for long-term operation. Here, we report a comprehensive study of how different cell configurations (asymmetry and membrane CDI) and voltages affect the desalination capacity and the stability of the activated carbons (AC) derived from *p*-toluenesulfonate- or sulfate-doped polyaniline (PAC/PTS or PAC/S, respectively). It was demonstrated that the electrochemical and textural properties of these materials have a major influence on the electrode stability. The control of the potential distribution in asymmetric cells is pointed out as an effective strategy to suppress the carbon oxidation reactions responsible for the  $SAC$  loss, and improve the long-term stability. The best desalination performance was achieved using PAC/PTS electrodes in a MCDI configuration. A remarkable value of  $SAC$  ( $\sim 32 \text{ mg g}^{-1}$  at 1.2 V), along with 100% of  $SAC$  retention was observed over 100 cycles. Our findings enable a better understanding of how to mitigate undesirable faradaic reactions and improve the long-term stability of PAC electrodes, thus providing promising electrodes for water desalination.

#### 3.1. Introduction

According to the United Nations, over 2 billion people live in countries with high water stress, and about 4 billion undergo severe water scarcity during at least one month of the year. Accordingly, three out of ten people did not have a safe drinking water service in 2015, and this number is expected to increase owing to the growing demand and the effect of climate changes [2]. In this scenario, technologies for seawater and brackish water desalination have gaining the attention as alternatives to provide drinking water [18].

Among the desalination techniques, capacitive deionization (CDI) has attracting attention due to its low energy consumption and easy maintenance and operation [17,31]. Based on the electrosorption of salts in the electric double layer (EDL) formed when a pair of electrodes is electrified, CDI has been applied to desalinate brackish water ( $<10 \text{ g L}^{-1}$ ). Once saturated, the electrodes can be easily regenerated to enable operation in consecutive cycles of electrosorption/desorption [18].



In order to achieve an effective CDI performance, electrode materials with high adsorption capability are mandatory [152]; therefore, carbon materials with large surface area accessible for electrosorption, high electrical conductivity, hydrophilic, and chemically stable [18,134] are abundantly reported in the CDI related literature [164–166]. Recently, polyaniline-activated carbon (PAC) electrodes were successfully employed for CDI desalination [52,111,112] and became promising candidates for an effective application due to the low cost of the polyaniline (PAni) monomer and its facile synthesis in aqueous medium, besides its stability and graphite-like structure that facilitates the introduction of nitrogen-containing active sites in the carbon matrix [100,101]. In addition, the pseudocapacitance introduced by the presence of pyrrolic and pyridinic surface groups is recognized to improve the carbon wettability, conductivity and, consequently, enhancing the desalination performance [19,42,85,89]. Zornitta et al. [52] demonstrated that PAC performance can also be optimized regarding its chemical and textural properties by changing the doping anions of PAni during the polymerization process. The CDI performance of PAC electrodes was further improved in terms of salt adsorption capacity ( $SAC$ ) and charge efficiency ( $Q_E$ ) by using ion-exchange membranes (IEM) and asymmetric configurations [111]. Recently, it was found that the carbonization of *p*-toluenesulfonic acid (PTS)-doped PAni at 500 °C, followed by activation with KOH (4:1 wt./wt. KOH/carbon) at 850 °C provides a PAC/PTS electrode with a high  $SAC$  (22.2 mg g<sup>-1</sup> at 1.2 V), which is among the highest values reported in literature for desalination using carbon electrodes [112]. Considering all these advantages, PAC/PTS was chosen to be studied in this work.

Despite all the improvements made in the last few years in carbon electrodes for CDI, their stability in long-term desalination is less explored, although it is a paramount property required for an effective application of CDI for desalination. The decrease of ion removal by carbon electrodes is mainly attributed to carbon oxidation reactions that modify the surface chemical charge and shift the potential of zero charge ( $E_{PZC}$ ) to more positive values, thus boosting the co-ion expulsion effect responsible for the performance loss [51,118,119,121,167]. Concomitantly, an increase of the electrode resistivity and decrease of surface area and pore volume may also occur [121–123,167]. To prevent these reactions and improve the long-term stability, voltage optimization [118,119,168], inverted- CDI [51], alternating polarization [121], and IEM [126] have been proposed. However, despite the increasing attention that has been paid to this issue, the long-term stability of promising electrodes, such as PAC, still needs to be better comprehended.

This work aims to better understand how the electrode configuration and cell potential affect the desalination performance and stability over consecutive electrosorption/desorption cycles. In order to achieve this purpose, a systematic study using PAC/PTS electrodes was performed considering the promising results previously mentioned. Additionally, a new activated carbon (AC) obtained using sulfate-doped PAni as precursor is proposed to investigate the influence of chemical

and textural properties on the desalination stability. Asymmetric configurations were assessed by changing the chemical surface groups and  $E_{PZC}$  of the ACs through chemical treatments of PAC with ethylenediamine or (3-aminopropyl)triethoxysilane. Symmetric configurations for performance comparison and MCDI were also investigated.

Finally, the best electrode configurations giving the highest  $SAC$ ,  $Q_E$ , and the fastest electrosorption/desorption rates were chosen for long-term experiments. Considering that asymmetry and MCDI are reported to minimize the co-ion expulsion, our findings enable a better understanding of the role of  $E_{PZC}$  and propose strategies to optimize the desalination capacity, suppress the oxidation reactions, and improve the long-term stability of PAC electrodes.

## 3.2. Experimental

### 3.2.1 Materials

The aniline monomer (99%, Sigma-Aldrich) was distilled prior to the polymerization and maintained at low temperature ( $<3\text{ }^{\circ}\text{C}$ ) to prevent oxidation. *P*-toluenesulfonic acid monohydrate (HPTS,  $\geq 98.5\%$ , Sigma-Aldrich) and sulfuric acid (95.0-98.0%, Sigma-Aldrich) were used as doping anion sources, while ammonium persulfate (98%, Synth) was used as oxidant to promote polymerization. KOH (Sigma-Aldrich) was used for chemical activation. Nitric acid (70%, Sigma-Aldrich), ethylenediamine ( $\geq 99\%$ , Sigma-Aldrich), (3-aminopropyl)triethoxysilane (APTES, 99%, Sigma-Aldrich), and toluene (99.8%, anhydrous, Sigma-Aldrich,) were used for the surface treatments of the AC in order to obtain different surface charges and asymmetric electrodes. The electrodes were prepared using polytetrafluoroethylene (PTFE, 60 wt.%, Sigma-Aldrich) and ethanol (Sigma-Aldrich) as binder and solvent, respectively. The ion-exchange membranes were purchased from Membranes International Inc. and maintained in a 5% NaCl solution prior to use. The thickness ( $\delta$ ), electrical resistance at 0.5 mol L<sup>-1</sup> NaCl ( $R_A$ ), ion-exchange capacity ( $IEC$ ), and permselectivity at 0.1 mol KCl kg<sup>-1</sup>/0.5 mol KCl kg<sup>-1</sup> ( $perm_{sel}$ ) of the cationic membrane (CMI-7000S) were 0.45 mm,  $< 30\ \Omega\ \text{cm}^2$ , 1.6 meq g<sup>-1</sup>, and 94%, respectively. For the anionic membrane (AMI-7001S),  $\delta = 0.45\ \text{mm}$ ,  $R_A < 40\ \Omega\ \text{cm}^2$ ,  $IEC = 1.3\ \text{meq g}^{-1}$ , and  $perm_{sel} = 90\%$ . The commercial activated carbon Kuraray YP-80F was purchased from Kuraray Co.

### 3.2.2 PANi and AC syntheses, surface treatments, and electrode preparation

PTS- and sulfate (S)-doped PANi were synthesized by adding 10 mL of aniline under constant stirring to 0.3 mol L<sup>-1</sup> solution (500 mL) containing the doping anion (from HPTS or H<sub>2</sub>SO<sub>4</sub>). The

polymerization process started by adding 85.9 mL of the oxidant solution ( $1.0 \text{ mol L}^{-1}$   $(\text{NH}_4)_2\text{S}_2\text{O}_8$ ) into the monomer solution. The syntheses were carried for 24 h at  $3 \text{ }^\circ\text{C}$  or  $25 \text{ }^\circ\text{C}$  in order to obtain PANi/PTS and PANi/S, respectively. After polymerization, the as-obtained polymers were filtered, washed with deionized water, and dried in an oven at  $60 \text{ }^\circ\text{C}$  for 24 h.

The polymers were carbonized and activated according to the optimized conditions found by Zornitta et al. [112]. First, carbonization was carried out at  $500 \text{ }^\circ\text{C}$  for 2 h in a tubular furnace (Thermo Scientific Lindberg Blue M) at a heating rate of  $10 \text{ }^\circ\text{C min}^{-1}$ , under  $\text{N}_2$  atmosphere ( $150 \text{ mL min}^{-1}$ ). The samples were then impregnated with KOH (4:1 wt./wt. KOH:carbon) and activated at  $850 \text{ }^\circ\text{C}$  for 1.5 h using the same heating rate and  $\text{N}_2$  flow employed in the carbonization step. The as-obtained ACs were washed with a solution of  $0.5 \text{ mol L}^{-1}$  HCl and then with distilled water ( $60 \text{ }^\circ\text{C}$ ) until constant pH, and finally dried at  $105 \text{ }^\circ\text{C}$  for 24 h. The activated carbons were labeled as PAC/S and PAC/PTS.

Two surface treatments were carried out in order to obtain positively charged materials. The treatment using ethylenediamine was performed according to a procedure adapted from Gao et al. [169]. In brief, the PAC/S or PAC/PTS were mixed with  $\text{HNO}_3$  (1:13 wt./wt.), stirred for 24 h, washed with plentiful warm water until neutral pH, and then dried in an oven at  $105 \text{ }^\circ\text{C}$  for 24 h. The acid-treated PACs were mixed with ethylenediamine (1:13 wt./wt.) in a round bottom flask, heated to  $105 \text{ }^\circ\text{C}$ , and maintained under reflux for 5 h. After that, the suspension was heated without reflux until the complete evaporation of the ethylenediamine. The surface-modified PACs were washed with warm water until neutral pH, dried in an oven at  $105 \text{ }^\circ\text{C}$  for 24 h, and labeled as ePAC/S and ePAC/PTS.

The PACs were also chemically modified by silanization through the reaction between a silylating agent and the hydroxyl groups on the carbon surface [170]. To obtain the modified material, 1.0 g of PAC was mixed with 12.5 mL of a toluene solution containing 30% vol./vol. of APTES. The suspension was stirred for 24 h in a sealed container and then filtered, washed with distilled water, dried in an oven at  $105 \text{ }^\circ\text{C}$  for 24 h, and labeled as sPAC/S and sPAC/PTS.

The electrodes were prepared by mixing 95 wt.% AC and 5 wt.% PTFE. Firstly, the AC was dispersed in ethanol until a homogeneous slurry was obtained. After adding PTFE, the mixture was kneaded and rolled out in a rolling machine (Marcato Atlas 150) to obtain free-standing electrodes. Finally, the electrodes were dried in an oven at  $120 \text{ }^\circ\text{C}$  for 24 h. The electrode thickness was  $\sim 250 \text{ }\mu\text{m}$ .

### 3.2.3 Characterization

#### 3.2.3.1 Materials

Scanning electron microscopy (SEM) images of the different materials were obtained using a JEOL JSM 6610 microscope. Energy-dispersive X-ray spectroscopy (EDX) was also carried out using an

UltraDry detector from Thermo Scientific. Nitrogen physisorption measurements were performed using a Micromeritics ASAP 2420 instrument. Prior to the measurements, the samples PAC/PTS, PAC/S, and YP-80 were first degassed at 90 °C (1 h) and then at 150 °C (12 h). The outgassing temperatures for the materials treated with ethylenediamine (ePAC/S and ePAC/PTS) and APTES (sPAC/S and sPAC/PTS) were 50 °C (12 h) and 70 °C (12 h), respectively. The specific surface area ( $SSA$ ) was calculated by the Brunauer-Emmett-Teller equation ( $SSA_{BET}$ ) in the relative pressure ( $P/P_0$ ) range of 0.05–0.20. The 2D-NLDFT heterogeneous surface model was employed to calculate the pore size distributions (PSD), total pore volume ( $V_T$ ), and  $SSA_{DFT}$  using the SAIEUS software.

### 3.2.3.2 Electrochemical

Cyclic voltammetry (CV), galvanostatic charge-discharge (GCD), and electrochemical impedance spectroscopy (EIS) were performed in a 1.0 mol L<sup>-1</sup> NaCl solution using an electrochemical workstation (Multi Autolab/M204) and a three-electrode cell. The AC electrodes were used as working and counter electrodes. An Ag/AgCl (KCl<sub>sat</sub>) electrode was used as reference. The mass of the counter electrode was 3-fold larger than the working electrode.

The cyclic voltammograms were recorded at scan-rates ( $\nu$ ) ranging from 5 to 100 mV s<sup>-1</sup>, within a potential window between -0.2 and 0.5 V vs. Ag/AgCl. The specific capacitance ( $C_S$ ) and the average capacitance ( $C_{CV}$ ) of the electrodes (F g<sup>-1</sup>) were calculated according to Eqs. (3.1) and (3.2), respectively, where  $I$  is the current (A),  $m$  is the mass (g) of the active material in the working electrode, and  $E_1$  (V) and  $E_2$  (V) are the lower and upper values of the potential window.

$$C_S = \frac{I}{\nu \cdot m} \quad (3.1)$$

$$C_{CV} = \frac{\int_{E_1}^{E_2} I dV}{2 \cdot \nu \cdot m \cdot (E_2 - E_1)} \quad (3.2)$$

GCD measurements were performed at specific currents ranging from 0.25 to 10 A g<sup>-1</sup>. In this case, the specific capacitance ( $C_{GCD}$ ) was calculated from the slope of the discharge curve using Eq. (3.3), where  $I_d$  is the discharge current (A),  $\Delta t$  the discharge time (s), and  $\Delta E$  is the potential difference (V) after discharge, subtracting the ohmic drop. The lower and upper potential limits were -0.2 and 0.5 V vs. Ag/AgCl.

$$C_{GCD} = \frac{I_d \cdot \Delta t}{m \cdot \Delta E} \quad (3.3)$$

EIS was performed at frequencies ranging from 1 mHz to 10 kHz, applying 0.0 V and an alternating current amplitude of 10 mV. The Nyquist plot was adjusted to an equivalent circuit using the Autolab NOVA v2.1 software in order to determine the specific capacitance, charging resistance, and mass transfer resistance. The potential of zero charge ( $E_{PZC}$ ) was also determined by EIS in 1080

mg L<sup>-1</sup> NaCl, applying 10 mHz, and a step potential (100 mV or 50 mV) starting from -0.5 V up to +0.5 V vs. Ag/AgCl. The capacitance ( $C_{EIS}$ ) was calculated from Eq. (3.4), where  $\omega$  is the angular frequency and  $Z''$  the imaginary component of the EIS spectrum.  $C_{EIS}$  was normalized considering the lowest capacitance value.

$$C_{EIS} = \frac{1}{|\omega Z''|} \quad (3.4)$$

The potential stability window (PSW) was determined according to the Faradaic Fraction ( $R$ ) method reported by Xu et al. [171]. Accordingly, cyclic voltammograms were recorded at 5 mV s<sup>-1</sup> in 1.0 mol L<sup>-1</sup> NaCl, varying the vertex potential at an increment of 0.1 V. Scans towards positive potentials started at -0.1 V and finished at the 1.2 V, while scans towards negative potentials started at +0.1 V and finished at -1.2 V. The  $R$ -values were calculated from Eqs. (3.5) and (3.6), in which  $Q_{pos}$  and  $Q_{neg}$  correspond to the anodic and cathodic charges, respectively.

$$R_{pos} = \frac{Q_{pos}}{Q_{neg}} - 1 \quad (3.5)$$

$$R_{neg} = \frac{Q_{neg}}{Q_{pos}} - 1 \quad (3.6)$$

### 3.2.4 Electrosorption performance

The CDI cell used for desalination consisted of two acrylic plates, a pair of carbon electrodes (2.0 cm × 2.3 cm), and graphite current collectors, as shown in Fig. 3.1. The plastic mesh placed between the carbon electrodes provided the gap needed for the electrolyte flow and also to avoid short-circuit. All the components were assembled by nuts and bolts. Rubber gaskets sealed up the cell. Additionally, two Ag/AgCl (KCl<sub>sat</sub>) reference electrodes were coupled to the cell to record the potentials at the positive and negative electrodes.

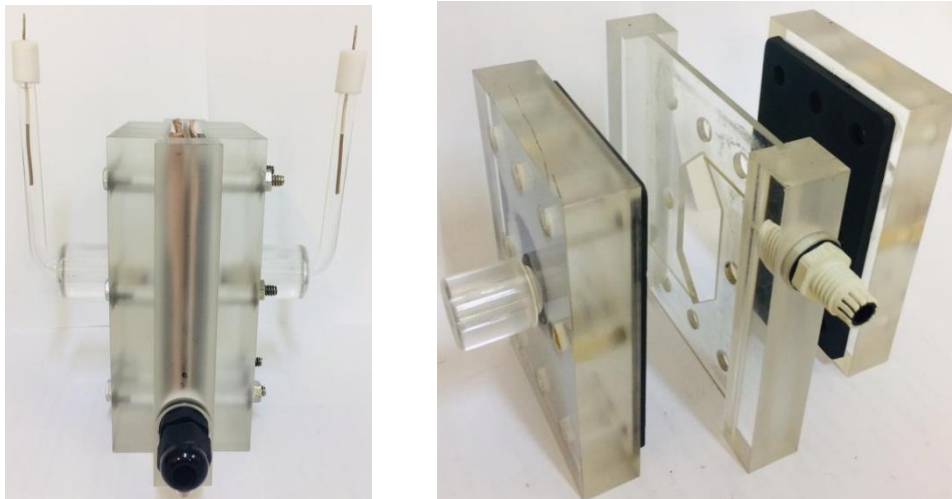


**Fig. 3.1.** CDI cell. The cell was developed in the INM group and adapted from [119].

Firstly, short-term experiments (15 cycles) were carried out to investigate the effect of the electrode configurations (symmetric, asymmetric, and MCDI) on the desalination performance. In this case, the desalination was carried out using a recirculating batch-mode. A peristaltic pump (Masterflex L/S) pumped a 1080 mg L<sup>-1</sup> NaCl solution (35 mL) between the CDI cell and the reservoir at a constant flow rate (26 mL min<sup>-1</sup>). A potentiostat Autolab M204 provided the constant cell potential of 1.2 V and 0.0 V during the electrosorption and desorption steps, respectively.

The desalination was followed by measuring the solution conductivity and pH every 10 s at the exit of the cell using a Seven Excellence instrument (Mettler Toledo). Before converting the conductivity values to concentration, Eq. (3.7) was employed to compensate the effect of the pH on the solution conductivity [62]. In this equation,  $\sigma_n$  is the real conductivity ( $\mu\text{S cm}^{-1}$ ),  $\sigma_m$  is the measured conductivity ( $\mu\text{S cm}^{-1}$ ),  $\kappa_B$  is the Boltzmann constant ( $1.38 \times 10^{-23} \text{ m}^2 \text{ kg s}^{-2} \text{ K}^{-1}$ ),  $N_A$  is the Avogadro constant ( $6.022 \times 10^{23} \text{ mol}^{-1}$ ),  $D_{H_3O^+}$  is the diffusion coefficient of hydronium ion ( $9.3 \times 10^{-9} \text{ m}^2 \text{ s}^{-1}$ ),  $D_{OH^-}$  is the diffusion coefficient of a hydroxyl ion ( $5.3 \times 10^{-9} \text{ m}^2 \text{ s}^{-1}$ ),  $e$  is the charge of the electron ( $1.602 \times 10^{-19} \text{ C}$ ), and  $T$  is the temperature (K).

$$\sigma_n = \sigma_m - \frac{10^7 \cdot e^2}{\kappa_B \cdot T} (10^{-pH} \cdot N_A \cdot D_{H_3O^+} + \frac{10^{-14}}{10^{-pH}} \cdot N_A \cdot D_{OH^-}) \quad (3.7)$$

The electrosorption performance was evaluated in terms of salt adsorption capacity ( $SAC$ ), charge efficiency ( $Q_E$ ), and specific energy consumption ( $\eta$ ), calculated according to Eqs. (3.8) to (3.10), respectively.

$$SAC = \frac{(C_0 - C_t) \cdot V}{m_E} \quad (3.8)$$

$$Q_E = 100 \frac{z \cdot F \cdot m_E \cdot SAC}{M_{NaCl} \int_{t_1}^{t_2} I dt} \quad (3.9)$$

$$\eta = \frac{E_{cell} \int_{t_1}^{t_2} I dt}{m_{rem}} \quad (3.10)$$

In these equations,  $C_0$  is the initial salt concentration (mg L<sup>-1</sup>),  $C_t$  is the salt concentration (mg L<sup>-1</sup>) at time  $t$  (s),  $V$  is the electrolyte volume (L),  $m_E$  is the total mass of the active material in both electrodes (g),  $z$  is the ion valence,  $F$  is the Faraday constant (96485 C mol<sup>-1</sup>),  $I$  is the applied current to the cell (A),  $M_{NaCl}$  is the molecular weight of NaCl (58440 mg mol<sup>-1</sup>),  $E_{cell}$  is the cell potential in the electrosorption step (V), and  $m_{rem}$  is the amount of ions removed from the solution (mg).

The electrosorption capacity and the electrosorption and desorption kinetics were also investigated using the Optimized Salt Removal (OSR) approach proposed by Zornitta and Ruotolo [111]. In brief, the electrosorption ( $k_e$ ) and desorption rate constants ( $k_d$ ) were properly fitted according to a pseudo first-order model (Eq. (3.11)), where  $mSAC$  is the highest value of  $SAC$  (mg g<sup>-1</sup>) and  $SAC' = mSAC - SAC(t)$ . The desorption time ( $t_d$ ) was evaluated considering 99% of electrode regeneration and the optimized electrosorption time ( $t_e$ ) was calculated by deriving the amount of salt

removed,  $m_{sr}$  (Eq. (3.12)), and making it equal to zero (point of maximum). The  $OSR$  values ( $\text{mg g}^{-1} \text{ day}^{-1}$ ) were calculated by replacing  $t_e$  in Eq. (3.12) and represent the amount of salt removed per gram of electrode material in a given operational time ( $t_{op}$ ).

$$SAC' = mSAC \cdot \exp(-k_1 \cdot t) \quad k_1 = k_e; k_d \quad (3.11)$$

$$m_{sr} = \frac{t_{op} \cdot m_E \cdot mSAC}{t_e + t_d} (1 - e^{-k_e \cdot t_e}) \quad (3.12)$$

The long-term performance was investigated only for the electrode configurations displaying the best results for desalination, determined considering  $SAC$ ,  $Q_E$ ,  $\eta$ , and  $OSR$ . The electrode stability was evaluated over 100 electrosorption/desorption cycles in a quasi-single-pass mode. Briefly, the electrolyte ( $1080 \text{ mg L}^{-1} \text{ NaCl}$ ) was pumped from a reservoir (2 L) to the CDI cell at a constant flow rate of  $10 \text{ mL min}^{-1}$ . The ratio between the electrolyte volume and the carbon mass is sufficiently high to ensure that the inflow concentration in the cell is practically constant. The potentiostat provided a constant cell voltage during the electrosorption (1.0, 1.1, or 1.2 V) and desorption (0.0 V) steps. In this case, the  $SAC$  was calculated according to Eq. (3.13), where  $\dot{V}$  is the volumetric flow rate ( $\text{L min}^{-1}$ ),  $C(t)$  is the concentration at time  $t$  ( $\text{mg L}^{-1}$ ), and  $t_1$  and  $t_2$  are the time (min) at which the electrosorption step starts and finishes, respectively.

$$SAC = \frac{\dot{V} \cdot \int_{t_1}^{t_2} C(t) dt}{m_E} \quad (3.13)$$

### 3.3. Results and discussion

Although excellent desalination performance had been obtained using PAC/PTS [52,111,112], in this work a new PAC is proposed as an attempt to reduce the cost with the dopant, by replacing HPTS by  $\text{H}_2\text{SO}_4$ . The as-obtained sulfate-doped PANi was then used as precursor for PAC/S. It was expected that PAC/S could benefit from the electrochemical advantages of PAC, besides reducing the cost of the electrode material, since Zornitta et al. [52] demonstrated that the PANi doping anions can act as templates during PANi carbonization, having an impact on the pore structure, surface groups, resistivity, and wettability of the resulting PACs. Additionally, the distinct chemical and textural properties of PAC/S and PAC/PTS obtained in this work allowed the investigation of the influence of these properties on the electrode performance and stability for both short- and long-term desalination.

The polymerization yield ( $Y_{PANi}$ ) is the ratio between polyaniline and aniline (wt./vol.) and was calculated for the different materials (Table 3.1). The highest value was observed for PAC/PTS, not only due to the high molecular weight of the *p*-toluenesulfonate anion, but also because the synthesis carried out at low temperature leads to a higher polymerization degree [172]. The carbonization ( $Y_C$ )

and activation ( $Y_A$ ) yields were calculated from the ratio of carbonized material and polyaniline (wt./wt.) and the ratio of activated carbon and carbonized material (wt./wt.), respectively. Although  $Y_C$  are similar for PAC/S and PAC/PTS, the difference in  $Y_A$  suggests that the doping anion also influences the activation mechanism. Indeed, the SEM images shown in Fig. 3.2 reveal differences in morphologies that reinforce this statement.

**Table 3.1.** Polymerization ( $Y_{PAni}$ ), carbonization ( $Y_C$ ), activation ( $Y_A$ ) and overall ( $Y_0$ ) yields for PAC/S and PAC/PTS.

<b>Material</b>	<b><math>Y_{PAni}</math> (gPAni/mL aniline)</b>	<b><math>Y_C</math> (%)</b>	<b><math>Y_A</math> (%)</b>	<b><math>Y_0</math> (%)</b>
PAC/S	$0.80 \pm 0.03$	$55.0 \pm 1.4$	$20.6 \pm 0.6$	$11.3 \pm 0.6$
PAC/PTS	$0.98 \pm 0.07$	$54.0 \pm 4.3$	$26.4 \pm 2.6$	$14.2 \pm 2.5$

### 3.3.1 PAC characterization

According to the SEM images shown in Fig. 3.2, PAC/PTS particles have cavities that are not observed in PAC/S, indicating a strong reaction of the carbonized precursor with KOH, which releases large amounts of volatiles during activation [112], thus leading to the remarkable values of SSA and  $V_T$  of PAC/PTS displayed in Table 3.2. It seems that the sulfate-doping suppresses this effect, and PAC/S particles become denser. Regarding the chemical treatments, they also impacted the PAC morphology, especially for the samples treated with ethylenediamine.



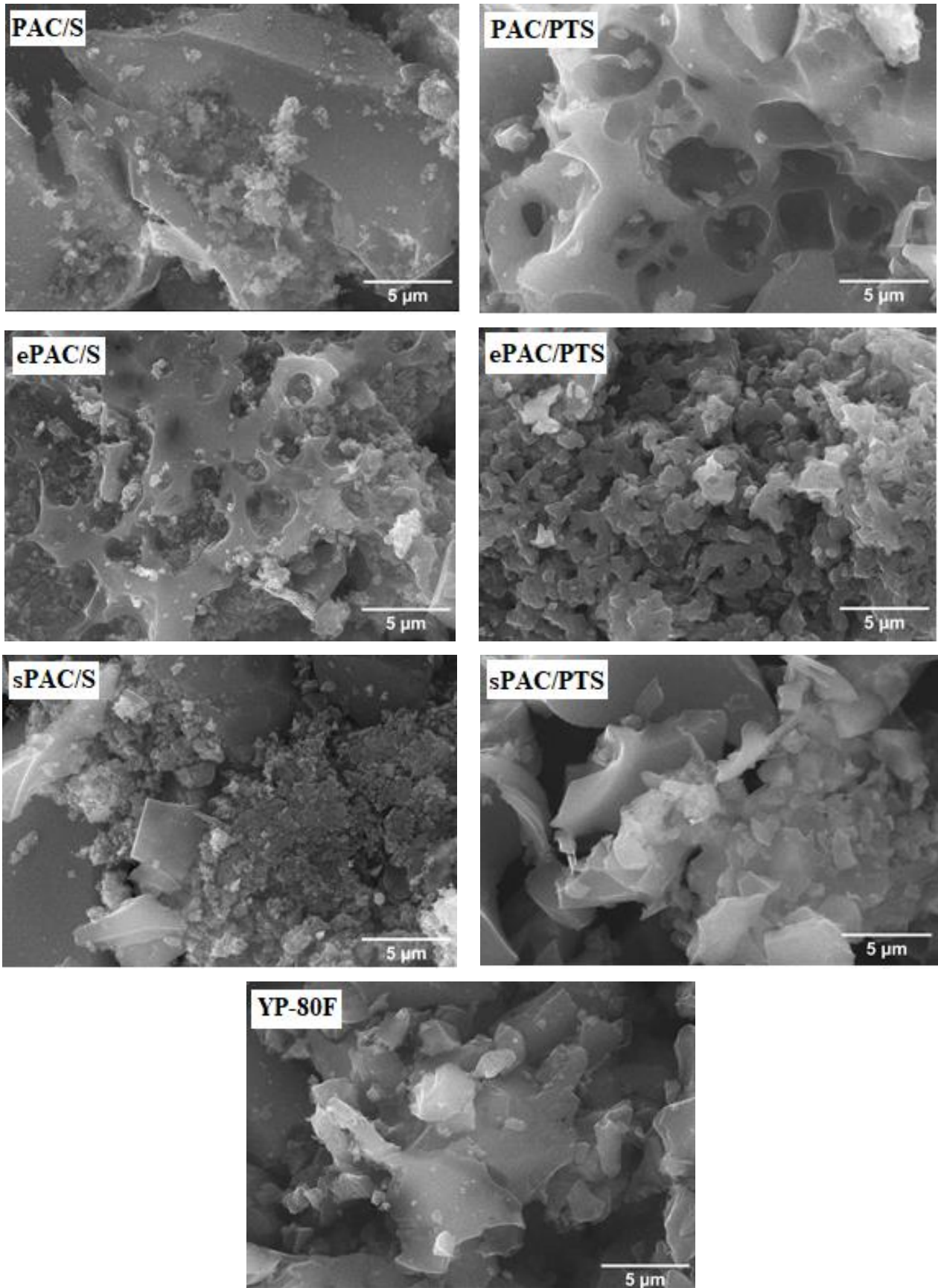


**Fig. 3.2.** SEM micrographs of the as-synthesized PACs, PACs after the chemical treatments, and YP-80F.

**Table 3.2.** Textural analysis: specific surface area ( $SSA_{BET}$  and  $SSA_{DFT}$ ), total pore ( $V_T$ ), micropore ( $V_{mic}$ ) and mesopore ( $V_{mes}$ ) volumes, and percentage of mesopores ( $\%V_{mes}$ ).

Material	$SSA_{BET}$ ( $\text{m}^2 \text{g}^{-1}$ )	$SSA_{DFT}$ ( $\text{m}^2 \text{g}^{-1}$ )	$V_T$ ( $\text{cm}^3 \text{g}^{-1}$ )	$V_{mic}$ ( $\text{cm}^3 \text{g}^{-1}$ )	$V_{mes}$ ( $\text{cm}^3 \text{g}^{-1}$ )	$\%V_{mes}$
PAC/S	2630	2213	1.52	0.74	0.78	51.2
ePAC/S	2228	1697	1.21	0.62	0.59	49.0
sPAC/S	1011	758	0.58	0.25	0.33	56.9
PAC/PTS	3444	2923	1.70	1.10	0.60	35.1
ePAC/PTS	1860	1443	0.86	0.60	0.27	30.1
sPAC/PTS	732	537	0.37	0.21	0.16	43.9
YP-80F	2591	1955	1.19	0.81	0.38	31.8

In addition to changing the morphology, the chemical treatments also change the  $SSA$  and PSD of the as-synthesized PACs (Fig. 3.3). The nitrogen adsorption/desorption measurements (Fig. 3.3(a)) showed isotherms having mostly type I feature. According to the IUPAC classification, type I isotherms indicate the presence of micropores ( $<2 \text{ nm}$ ) and the H4 hysteresis ( $0.4 < P/P_0 < 0.7$ ) reveals the contribution of mesopores, especially for PAC/S, ePAC/S, and sPAC/S. The PSD (Fig. 3.3(b)) reinforces the presence of micro- and mesopores, while the cumulative pore volume plot (inset in Fig. 3.3(b)) reveals a decrease of the PAC pore volume as a consequence of the applied surface treatments, which was also observed for other activated carbons [169,170,173].

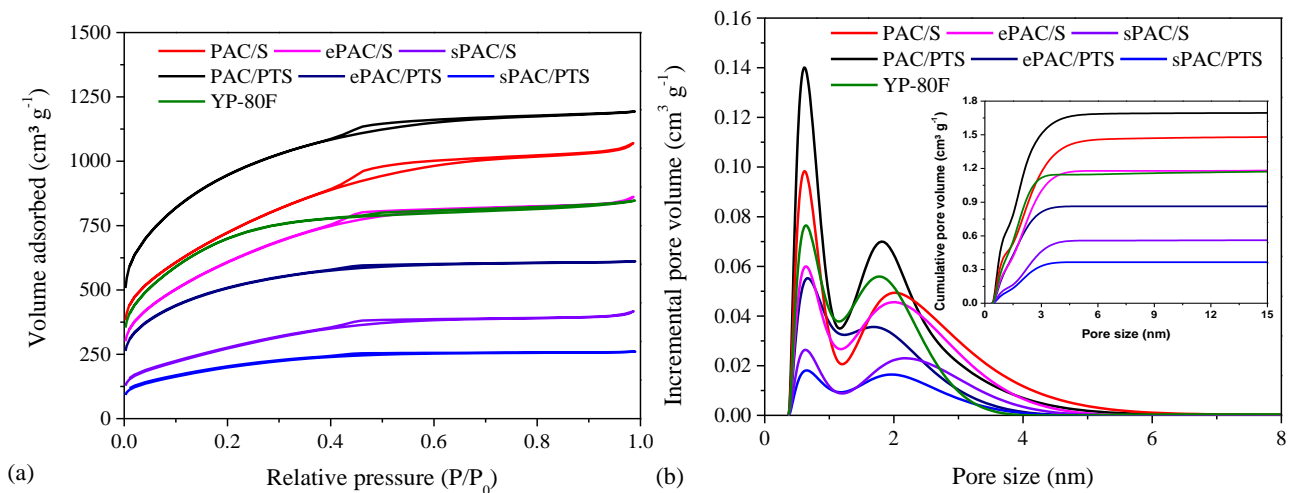


**Fig. 3.3.** Nitrogen adsorption-desorption isotherms at  $-196 \text{ }^\circ\text{C}$  (a) and pore size distribution (b).

Inset: cumulative pore volume.

The Table 3.2 summarizes the textural properties of the activated carbons. Firstly, it is important to note that PAC/PTS and PAC/S display the highest values of  $SSA_{BET}$  and  $SSA_{DFT}$ , which are high compared to other ACs reported in the literature [151–154]. However, the  $SSA$  and pore volume drastically diminished depending on the surface treatments. For instance, compared to the samples without chemical treatment, the  $SSA_{DFT}$  decreases 23.3%, 65.7%, 50.6%, and 81.6% for ePAC/S, sPAC/S, ePAC/PTS, and sPAC/PTS, respectively. The same trend is observed for  $V_T$ , suggesting that the microporous nature of PAC/PTS makes it more prone to pore clogging. The efficacy of the surface treatments was assessed by EDX analysis (Table 3.3), which confirmed that nitrogen and silicon are only present after the chemical treatments.

**Table 3.3.** EDX elemental analysis

Material	Weight (% m/m)		
	C	N	Si
PAC/S	100	-	-
ePAC/S	79.7	20.3	-
sPAC/S	73.9	19.5	6.64
PAC/PTS	100	-	-
ePAC/PTS	79.1	20.9	-
sPAC/PTS	80.7	13.0	6.33
YP-80F	100	-	-

### 3.3.2 Electrochemical characterizations

The electrochemical properties of the AC electrodes were assessed through CV, GCD, and EIS (Fig. 3.4). The cyclic voltammograms (Fig. 3.4(a)) presented a quasi-rectangular shape revealing the highly EDL capacitive behavior of the electrodes, without evidence of redox peaks. This behavior is reinforced by the triangular shape of the GDC curves (Fig. 3.4(c)) and the high coulombic efficiencies (92 - 98%) calculated considering the charge ratio recorded during the discharging and charging processes. The exception is the GCD curve recorded for the sPAC/S electrode, which displayed a slightly distorted triangular shape. In this case, the resulting coulombic efficiency was 74%, which is an indicative of the presence of faradaic processes [174].

In these electrochemical analyses, the electrode capacitances were sensitive to the AC surface treatments (Fig. 3.4(b and d)), and the following trend is evident:  $C_{PAC/PTS} > C_{PAC/S} > C_{ePAC/S} > C_{ePAC/PTS} > C_{YP-80F} > C_{sPAC/S} > C_{sPAC/PTS}$ . This trend can be mainly explained by the significant  $SSA$  and  $V_T$

reduction after the chemical treatments, as shown in Fig. 3.5(a). The main objective in this figure was not to evaluate the values of capacitance but to make evident the tradeoff between surface area and capacitance observed for the most of the electrodes investigated. However, as already reported in literature, high SSA is a desirable property for carbons employed for CDI, but it is not sufficient to ensure a high capacitance or even good desalination performance [52]. Accordingly, the deviation of the capacitances for YP-80F and ePAC/S indicates that the surface chemistry is also affecting the capacitance, as evidenced later by the  $E_{PZC}$  values.

Considering that the capacitance decreases due to mass transfer limitations as the scan rate and specific current increase (Fig. 3.4 (b) and (d)), it is expected that the PSD may play an important role on the electrosorption kinetics. Indeed, comparing sPAC/PTS and PAC/PTS, which correspond to the ACs with the lowest and highest SSA (and  $V_T$ ), respectively, there is a capacitance loss over the scan rate of 55.7% for the sPAC/PTS, while for the PAC/PTS this loss was 43.7%. The superior capacitance retention of PAC/PTS can be attributed to its higher volume of mesopores, which works as large avenues for ion diffusion, thus facilitating the access of the ions to the micropores [113,175]. A similar trend was observed considering the GCD capacitances.

EIS analyses were performed to evaluate both capacitance and series of resistances in the CDI cell. The shapes of the Nyquist plots (Fig. 3.4(e)) were typical of electrochemical supercapacitors, with a semi-circle representing the charge transfer domain at high frequencies and a line representing the mass transfer region at low frequencies [157]. The modified Randle equivalent circuit (Fig. 3.4(f)) successfully fitted the Nyquist plots. The circuit elements are summarized in Table 3.4 and include an ohmic resistance ( $R_\Omega$ ), ascribed to the current collector and electrolyte resistances; a charge transfer resistance ( $R_{CT}$ ), which is an intrinsic property of the carbon electrode; a Warburg element ( $W$ ), which describes the effect of ion migration inside the pores of the carbon film; the capacitance at the electrolyte/electrode interface ( $C_1$ ), and the capacitance developed inside the micropores of the carbon electrode ( $C_2$ ).

The values of  $R_\Omega$  are very low and, as expected, very similar, since all the measurements were performed in the same experimental setup. Any trend between  $R_{CT}$  and the surface treatments was identified, although the values for the sPAC/S and YP-80F are slightly inferior. The admittance element ( $A_0$ ), which is the inverse of the Warburg impedance, is an indicative of the diffusion rate of the ions into the carbon micropores. According to Fig 3.5(b and c), except for the PAC/S, the values of  $A_0$  correlate well with  $V_T$  and  $V_{mes}$ , demonstrating that the mass transfer is improved by the presence of mesopores, since they act as large avenues for ion mass transfer to the micropores [113,115]. The values of  $C_2$ , which correspond to the main contribution to the total capacitance, aligned well with those obtained by the CV and GDC techniques.

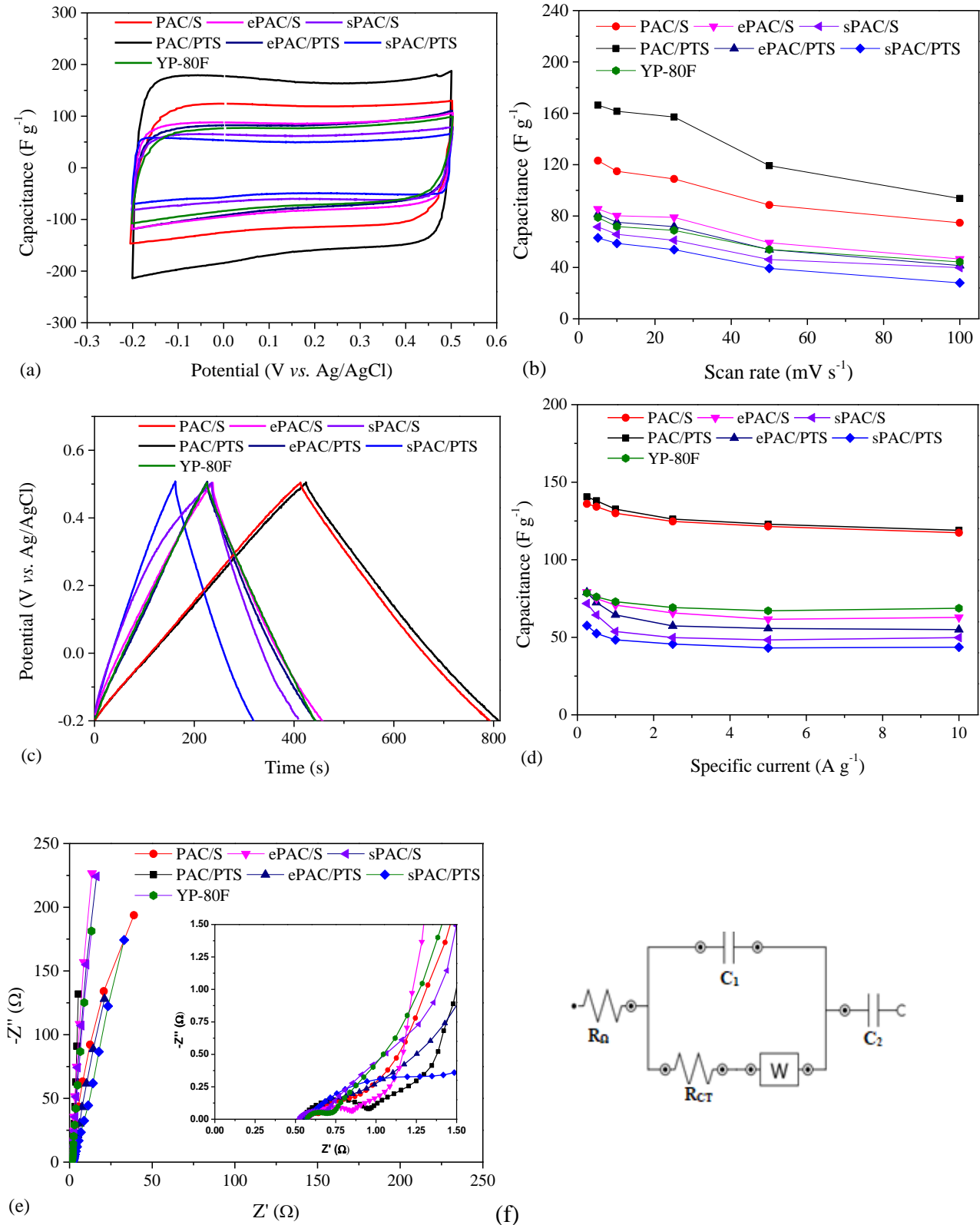


**Fig. 3.4.** Electrochemical characterizations of PAC and YP-80F electrodes: (a) Specific capacitance ( $C_S$ ) from CV recorded at  $5 \text{ mV s}^{-1}$ ; (b) Average CV capacitance ( $C_{CV}$ ) against scan rate; (c) GCD profiles recorded at  $0.25 \text{ A g}^{-1}$ ; (d) GCD capacitance against specific currents; (e) Nyquist plots, and (f) modified Randle equivalent circuit. Electrolyte:  $1 \text{ mol L}^{-1} \text{ NaCl}$ .

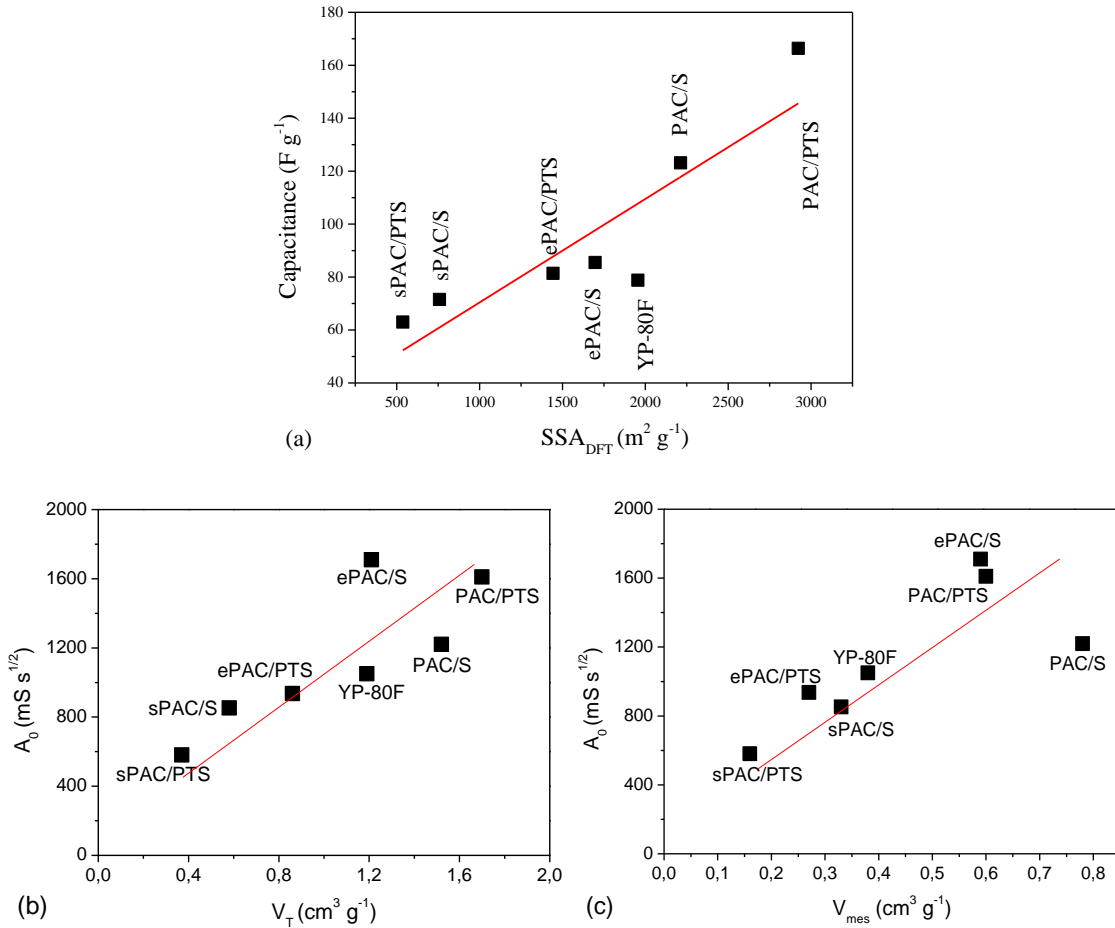


**Fig. 3.5.** (a) CV capacitance vs.  $SSA_{DFT}$ , and  $A_0$  as a function of  $V_T$  (b) and  $V_{mes}$  (c) for PAC and YP-80F electrodes. CV scan rate:  $5 mV s^{-1}$ .

**Table 3.4.** EIS parameters obtained from the Nyquist plots and the modified Randle equivalent circuit.

Electrode	$R_{\Omega}$ ( $\Omega$ )	$R_{CT}$ ( $\Omega$ )	$A_0$ ( $mS s^{1/2}$ )	$C_1$ ( $F g^{-1}$ )	$C_2$ ( $F g^{-1}$ )
PAC/S	0.591	0.266	1220	2.54	169.4
ePAC/S	0.625	0.257	1710	0.153	109.8
sPAC/S	0.525	0.130	852	0.124	78.9
PAC/PTS	0.578	0.400	1610	0.091	177.3
ePAC/PTS	0.463	0.315	936	0.791	95.9
sPAC/PTS	0.618	0.657	581	0.192	70.4
YP-80F	0.586	0.118	1050	0.136	90.6

In summary, the substantial reduction of  $SSA$  and  $V_T$  after the surface treatments led to a significant reduction in capacitance. However, despite these deleterious effects, it was hypothesized that the chemical treatments are able to modify the surface charge and  $E_{PZC}$ , leading to advantageous asymmetric electrode configurations for desalination.

### 3.3.3 Electrosorption: Symmetric and asymmetric electrode configurations

Considering that asymmetric electrodes have been reported to improve the desalination performance by (i) shifting the  $E_{PZC}$ , (ii) minimizing the co-ion expulsion, and (iii) maximizing the applied potential for effective ion electrosorption [51,81], different asymmetric configurations using PAC and YP-80F electrodes were evaluated in order to maximize  $SAC$ , enhance  $Q_E$ , and reduce the energy input. Additionally, to promote the  $E_{PZC}$  shift to more positive and negative values in the cathode and anode, respectively, chemical treatments have also been performed, as well as the use of IEM, which is recognized to improve the electrosorption capacity by reducing the effect of co-ion expulsion [80]. Fig. 3.6 displays the steady-state electrosorption/desorption profiles for the different proposed configurations. The curves for the symmetric CDI and MCDI PAC/S configurations are not shown because the processes were not stable and the steady-states were not achieved after 15 cycles, suggesting that the AC oxidation occurred at the anode [126,162,176]. Regarding the pH, fluctuations ranging from 5.5 to 7.8 were observed, thus Eq. (3.7) was used to correct the measured conductivity.

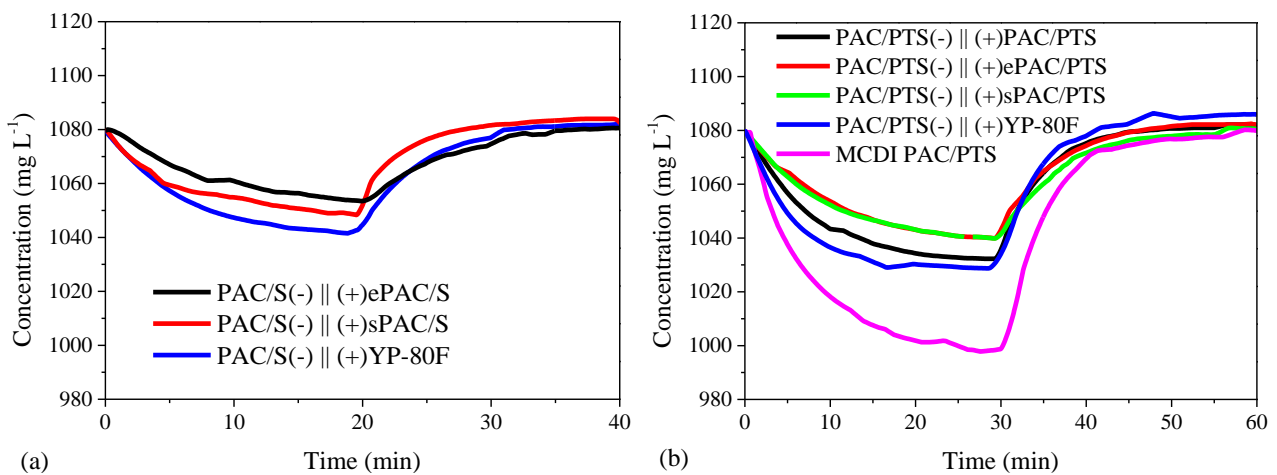


**Fig. 3.6.** CDI and MCDI performances of different symmetric and asymmetric electrode configurations using PAC/S (a) and PAC/PTS (b) electrodes. Electrolyte:  $1080 \text{ mg L}^{-1} \text{ NaCl}$ ;  $E_{cell}$ : 1.2 V (adsorption) and 0.0 V (desorption). IEM: cationic (CMI-7000S) and anionic (AMI-7001S).

According to Fig. 3.6, the PAC/PTS electrodes displayed superior performance than the PAC/S. In order to understand the differences in desalination performances, the  $E_{PZC}$  was determined by EIS. The minimum capacitance in Fig. 3.7(a) determines the  $E_{PZC}$ , which corresponds to the potential at which the whole surface charge of the electrode is compensated when this potential is applied [119]. The positive  $E_{PZC}$  ( $E_{PZC,PAC/S} = 0.3$  V; and  $E_{PZC,PAC/PTS} = 0.2$  V) of the unmodified PAC electrodes is an indicative of negatively charged surfaces. The effectiveness of the chemical treatments to modify the surface charge of the electrodes is also confirmed by the  $E_{PZC}$  shift to more negative values ( $E_{PZC,ePAC/S} = -0.1$  V;  $E_{PZC,ePAC/PTS} = -0.1$  V;  $E_{PZC,sPAC/S} = -0.2$  V;  $E_{PZC,sPAC/PTS} = -0.2$  V), compared to unmodified electrodes, indicating that after exposing PAC/S and PAC/PTS to the treatments with ethylenediamine and APTES, these PAC electrodes exhibited more positive surface charges.

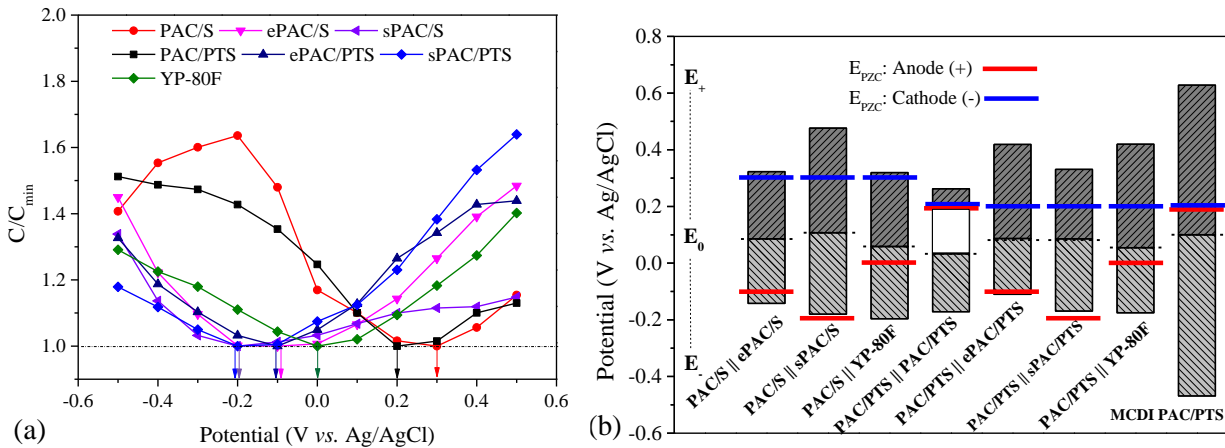


**Fig. 3.7.** (a) Normalized capacitance vs. electrode potential for PAC and YP-80F electrodes and (b) potential distribution of the symmetrical and asymmetrical CDI and MCDI configurations.  $E_0$  is the short-circuit potential.  $E_-$  and  $E_+$  indicate the potential in the cathode and anode, respectively. The potentials were determined considering the electrosorption/desorption cycles at steady state.

The  $E_{PZC}$ , the potentials measured at the cathode ( $E_-$ ) and anode ( $E_+$ ), and the short-circuit potential ( $E_0$ ) are displayed in the potential distribution diagram of Fig. 3.7(b). This diagram reveals the influence of the  $E_{PZC}$  of the negative and positive electrodes on the potential effectively used for electrosorption and the potential spent for co-ion expulsion, which are represented by the hatched and blank bars, respectively. According to the diagram, the  $E_{PZC}$  of the symmetric cell PAC/PTS(-)||(+)-PAC/PTS is higher than the  $E_0$ , meaning that part of the applied potential at the positive electrode is used for counterion electrosorption, whereas the other part is dedicated to co-ion expulsion. In the negative electrode, the applied potential is used for counterion electrosorption. In this scenario, it was expected that the introduction of IEMs in the CDI cell (MCDI PAC/PTS) would prevent the co-ion



expulsion in the positive electrode, besides enhancing the electrosorption capacity. For all asymmetric configurations with modified PAC electrodes or YP-80F as anode, the  $E_{PZC}$  of the two electrodes are out of their respective polarization window; therefore, the applied potential is mostly used for counterion electrosorption. The cell configurations in which the  $E_{PZC}$  values of the two electrodes are located within their corresponding polarization window (ePAC/S(-)||(+))PAC/S, sPAC/S(-)||(+))PAC/S, ePAC/PTS(-)||(+))PAC/PTS, and sPAC/PTS(-)||(+))PAC/PTS) were not further evaluated, since it is known that they correspond to the worst configurations for CDI in terms of  $SAC$  and  $Q_E$  [119,177]. In these cases, part of the charge in both electrodes is deviated for co-ion expulsion, diminishing the effective potential for adsorption.

Using the proper asymmetric configurations based on Fig. 3.7(b), the instability observed during the symmetric PAC/S cell operation does not repeat when PAC/S is used as negative electrode and ePAC/S, sPAC/S, or YP-80F are used as positive electrodes, as shown in Fig. 3.6(a). It is also important to note that, although the  $SAC$  for PAC/S(-)||(+))YP-80F is slightly superior to those for PAC/S(-)||(+))ePAC/S and PAC/S(-)||(+))sPAC/S, according to Table 3.5, the last two configurations outperform the first one in terms of  $\eta$  and  $Q_E$ , achieving  $\sim 100\%$   $Q_E$  and the lowest  $\eta$  when sPAC/S is employed as positive electrode. This trend is ascribed to the respective electropositivity and electronegativity of the anode and cathode material surfaces, which can also contribute for counterions electrosorption [177], compensating the loss in  $SSA$  observed for ePAC/S and sPAC/S.

The cells assembled with PAC/PTS displayed the following  $SAC$  sequence: MCDI PAC/PTS > PAC/PTS(-)||(+))YP-80F > PAC/PTS(-)||(+))PAC/PTS > PAC/PTS(-)||(+))sPAC/PTS > PAC/PTS(-)||(+))ePAC/PTS, thus confirming that the use of IEMs (MCDI PAC/PTS) is able to boost the  $SAC$  up to  $\sim 110\%$  compared to PAC/PTS(-)||(+))PAC/PTS, in accordance with its higher effective potential used for electrosorption shown in Fig. 3.7(b). Considering that for asymmetric configurations the co-ion expulsion is minimized, the outstanding  $SAC$  observed using membranes can be mainly ascribed to the presence of the co-ions which further contribute for ion removal [79,80]. Differently of a typical CDI process in which the counterions are adsorbed in the EDL formed within the micropores and the contribution of macropores for ion removal is negligible, over the electrode polarization in MCDI, the co-ions expelled from the micropores remain in the macropores due to the presence of the membranes. Hence, in order to maintain the charge balance, more counterions cross the membranes and accumulate in the macropores, thus leading to the remarkable value of  $SAC$  observed for MCDI.

Zornitta and Ruotolo [111] also investigated the use of IEM applying similar PAC/PTS electrodes and desalination setup, however, curiously the  $SAC$  enhancement was only  $\sim 34\%$ , achieving  $20.0 \text{ mg g}^{-1}$ . This remarkable difference is attributed to the differences in cell design, illustrated in Fig. 3.8. In the cell used by Zornitta and Ruotolo [111], the electrolyte can flow through the electrode voids (Fig. 3.8(a)), thus diminishing the benefic effect of the co-ions charge

compensation. On the other hand, in the cell used in this work (Fig. 3.8(b)), the electrode was completely isolated by the membrane, and consequently, all the co-ions in the macropores contribute to the counterions electrosorption.

**Table 3.5.** Electrosorption performance parameters ( $SAC$ ,  $Q_E$ , and  $\eta$ ) for the different CDI cell configurations. Electrolyte:  $1080 \text{ mg L}^{-1} \text{ NaCl}$ ;  $E_{cell}$ : 1.2 V (adsorption) and 0.0 V (desorption).

CDI cell configuration	$SAC \text{ (mg g}^{-1}\text{)}$	$Q_E \text{ (\%)}$	$\eta \text{ (J mg}^{-1}\text{)}$
PAC/S(-)    (+)ePAC/S	$13.3 \pm 0.5$	63.9	3.10
PAC/S(-)    (+)sPAC/S	$15.2 \pm 0.9$	99.1	1.92
PAC/S(-)    (+)YP-80F	$16.4 \pm 0.5$	57.6	3.44
PAC/PTS(-)    (+)PAC/PTS	$18.0 \pm 0.4$	71.6	2.77
PAC/PTS(-)    (+)ePAC/PTS	$12.6 \pm 0.6$	62.6	3.16
PAC/PTS(-)    (+)sPAC/PTS	$13.1 \pm 0.4$	67.9	2.92
PAC/PTS(-)    (+)YP-80F	$20.7 \pm 2.0$	73.9	2.69
MCDI PAC/PTS	$38.0 \pm 2.9$	99.2	1.92

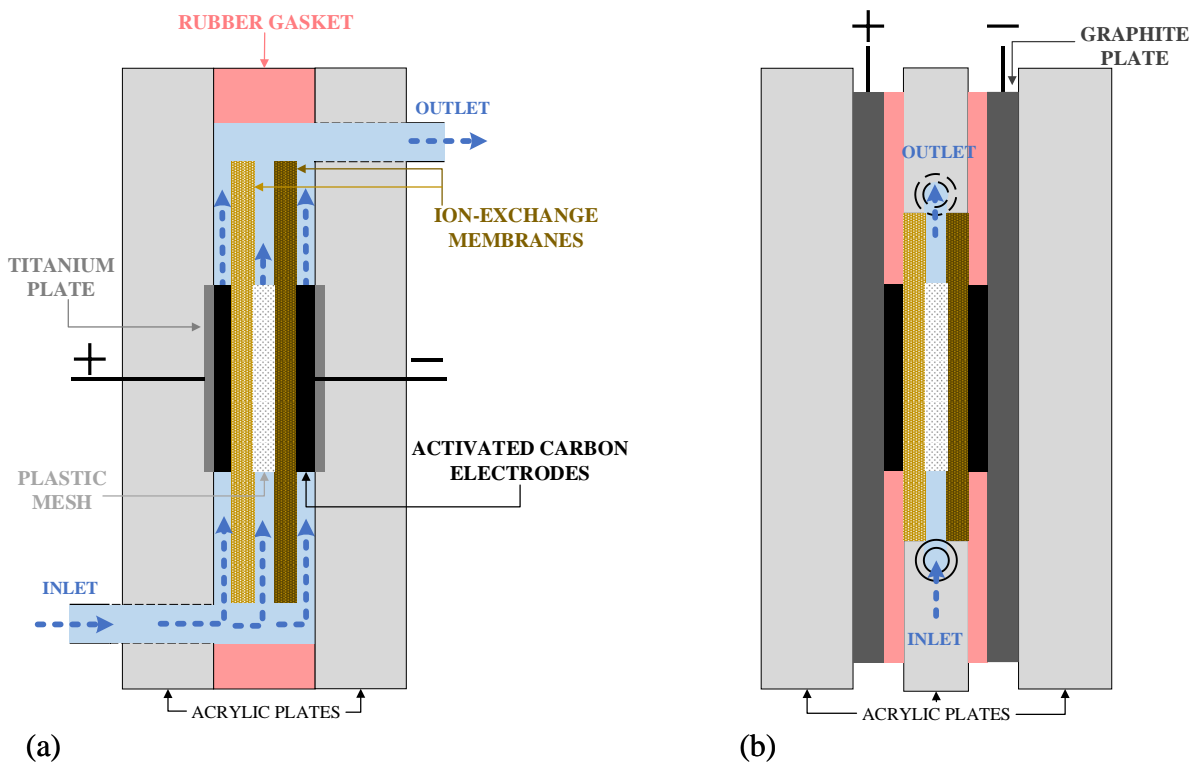


**Fig. 3.8.** Schematic illustrations of the CDI cell used by Zornitta and Ruotolo [111] (a) and in this work (b).

As previously mentioned, the chemical treatments of PAC/PTS with ethylenediamine and APTES were used to provide positive surface charges and promote the electrosorption by hindering the co-ion expulsion in asymmetric setups. However, on contrary to the observed using the surface-modified PAC/S electrodes, low  $SAC$  is obtained using PAC/PTS(-)||(+) $sPAC/PTS$  and PAC/PTS(-)||(+) $ePAC/PTS$  configurations, which is attributed to the substantial reduction of the  $SSA$  and  $V_T$  observed for  $sPAC/PTS$  and  $ePAC/PTS$  (Table 3.2). According to Table 3.5, the  $Q_E$  follows the same trend of the  $SAC$ , and MCDI PAC/PTS seems to be by far the most efficient configuration, achieving  $\sim 100\%$   $Q_E$  and the lowest  $\eta$ . In the case of PAC/PTS(-)||(+) $ePAC/PTS$  and PAC/PTS(-)||(+) $sPAC/PTS$  configurations, the reduction of the charge used for co-ion expulsion by introducing asymmetry was not sufficient to compensate their lower  $SAC$ , thus lower  $Q_E$  and higher  $\eta$  were observed. Additionally, comparing these configurations with those using PAC/S and modified PAC/S electrodes, the low values of  $E_{PZC}$  observed for PAC/PTS lead to a minor contribution of the cathode surface electronegativity for counterions electrosorption, thus impacting the charge efficiency and electrosorption capacity.

Comparing the CV and CDG capacitances (Fig. 3.4 (b, d) and Fig. 3.5(a)) and  $SAC$  (Table 3.5), it is noteworthy that the electrochemical characterizations are not able to predict alone the electrosorption performance trend of the different configurations, especially of those using asymmetric electrodes. For instance, although the activated carbons treated with ethylenediamine ( $ePAC/S$  and  $ePAC/PTS$ ) have higher capacitances than those treated with APTES ( $sPAC/S$  and  $sPAC/PTS$ ), they performed worse for desalination when used as anodes. This behavior can be ascribed to the less positive charge of  $ePAC/S$  and  $ePAC/PTS$  (less negative  $E_{PZC}$ ), thus revealing the great influence of the  $E_{PZC}$  on the co-ion expulsion and counterion electrosorption, consequently impacting the desalination performance of the asymmetric cells.

Although the  $SAC$  analysis is important to evaluate the capacity of ions storage, the electrosorption kinetics, and the time required for desorption are decisive to indicate the best electrode since they influence the number of CDI cycles and the amount of salt removed in a given operational time [111]. In this sense, it is important to evaluate the desalination performance considering the  $SAC$  and kinetics simultaneously. According to the  $OSR$  values displayed in Table 3.6, the MCDI PAC/PTS also outperforms the other cell configurations (145% higher than PAC/PTS(-)||(+) $PAC/PTS$ ). In addition, it is interesting to note that the desorption and electrosorption times have a strong influence on the  $OSR$ . For instance, comparing the desorption time using PAC/S(-)||(+) $YP-80F$  and PAC/S(-)||(+) $sPAC/S$ , which have relatively similar  $k_e$  and  $SAC$ , the desorption rate was the main factor indicating the PAC/S(-)||(+) $sPAC/S$  as the better configuration, with an  $OSR \sim 17\%$  superior. The faster  $k_d$  observed for this configuration is ascribed to three main factors: i) higher  $\%V_{mes}$  in  $sPAC/S$  that facilitates the ion mass transfer to and from the micropores; ii) faster EDL charging

owing to the minimization of the co-ions expulsion; and iii) anion adsorption due to the electropositive surface of sPAC/S. The same trends were not observed for PAC/PTS(-)||(+sPAC/PTS configuration. Despite the higher  $\%V_{mes}$  of sPAC/PTS (44%) compared with PAC/PTS (35%), the sharp  $V_T$  reduction ( $\sim 78\%$ ) after the chemical treatment certainly contributed to making the kinetics slow. Furthermore, the expressive decrease of SSA and  $V_T$  observed for the ePAC/S and ePAC/PTS explains the poor OSR performance of the configurations using these materials. Finally, in order to confirm the impact of asymmetry provided by the surface charge modification on the desalination performance, symmetric YP-80F electrodes were applied for desalination, giving the worst performance in terms of SAC ( $6.44 \text{ mg g}^{-1}$ ) and  $Q_E$  (48.7%).

**Table 3.6.** OSR values, considering the operational time of one day.

CDI cell configuration	$k_e$ ( $\text{s}^{-1}$ )	$k_d$ ( $\text{s}^{-1}$ )	$t_e$ (s)	$t_d$ (s)	$N_{cycles}$	SAC ( $\text{mg g}^{-1}$ )	OSR ( $\text{mg g}^{-1} \text{ day}^{-1}$ )
PAC/S(-)    (+)ePAC/S	0.0024	0.0029	797	1580	36	13.3	412
PAC/S(-)    (+)sPAC/S	0.0031	0.0058	528	788	65	15.2	798
PAC/S(-)    (+)YP80F	0.0031	0.0040	601	1147	49	16.4	683
PAC/PTS(-)    (+)PAC/PTS	0.0023	0.0035	765	1301	41	18.0	622
PAC/PTS(-)    (+)ePAC/PTS	0.0019	0.0028	930	1630	33	12.6	352
PAC/PTS(-)    (+)sPAC/PTS	0.0019	0.0025	970	1872	30	13.1	336
PAC/PTS(-)    (+)YP-80F	0.0029	0.0036	647	1270	45	20.7	791
MCDI PAC/PTS	0.0028	0.0040	643	1147	48	38.0	1526

Comparing the desalination performances shown in Tables 3.5 and 3.6, asymmetry and IEM, along with textural properties (Table 3.2), are the paramount parameters to be considered to establish an optimized CDI cell configuration. Except for PAC/S electrodes, the use of membranes enhanced the desalination performance of PAC/PTS electrodes in terms of SAC,  $Q_E$ , and kinetics, but imposed an additional capital cost for the cell. Regarding asymmetry, combining PAC and YP-80F electrodes revealed to be promising, mainly due to the superior textural properties of YP-80F (higher SSA and  $V_{mic}$ ). On the other hand, the asymmetry provided by the chemically modified materials (ePAC and sPAC) led to a poor SAC and OSR performance, although it has been reported in literature that they improve the electrode performance by reducing the co-ions expulsion [119,177–179]. For instance, Haq et al. [179] reported a SAC and  $Q_E$  enhancement for CDI from 7 to  $14.7 \text{ mg g}^{-1}$  and 37.5 to 85.8%, respectively, after anchoring amino and sulfonic groups to the activated carbon surface. Using MCDI, the respective values of SAC and  $Q_E$  increased to  $16.4 \text{ mg g}^{-1}$  and 89.2%. Even though the authors did not present the textural properties of the modified-electrodes, the advantages of the chemical surface

modification probably surpassed eventual disadvantages associated to SSA reduction due to the chemical treatments. On contrary, in this work, the deleterious effect of the chemical treatments on the SSA and pore volume of ePAC and sPAC led to poor desalination performance (lower *SAC* and *OSR* values). Therefore, here we demonstrate that there is a tradeoff between the chemical surface modification and the textural properties, more specifically, the SSA and pore volume.

Despite all the electrodes displayed in Table 3.6 have been stable during 15 cycles, for an effective application, these electrodes must be tested for a large number of cycles. In addition, during the long-term operation, the loss of electrosorption capacity of carbon electrodes is mainly attributed to carbon oxidation reactions that shift the  $E_{PZC}$  to positive values, thus boosting the co-ion expulsion [51,118,119,121,167]. Therefore, the best electrodes and configurations identified for short-term desalination were further evaluated regarding their long-term stability. Accordingly, desalination was then carried out for 100 cycles using PAC/S(-)||(+sPAC/S, PAC/PTS(-)||(+YF-80F, and MCDI PAC/PTS, which correspond, according to Tables 3.5 and 3.6, to the most promising configurations in terms of *OSR*,  $Q_E$ , and  $\eta$ .

### 3.3.4 Long-term desalination

One of the most challenging issues related to capacitive deionization concerns to its stable operation envisaging the long-term operation. CDI systems usually operate at voltages close to 1.2 V to prevent faradaic reactions [37]; however, the electrode potential may increase throughout the process up to values in which the carbon becomes not stable in both the anodic and cathodic regimes, sometimes even applying voltages lower than 1.2 V. In this sense, stable desalination operation could be achieved in the absence of faradaic reactions by controlling the cell potential. In order to understand the role of the electrochemical parameters on the electrode stability, the long-term stability of the PAC/S(-)||(+sPAC/S, PAC/PTS(-)||(+YF-80F, and MCDI PAC/PTS configurations was evaluated for desalination applying 1.0, 1.1, and 1.2 V. The desalination performances are shown in Fig. 3.9 and Table 3.7.

Fig. 3.9(a) shows that the PAC/S(-)||(+sPAC/S configuration, regardless the applied  $E_{cell}$ , is not stable. In this case, the *SAC* and  $Q_E$  decrease significantly after 100 cycles, with low *SAC* retention capabilities (~55% and ~42% at 1.0 and 1.1 V, respectively). Accordingly,  $Q_E$  decreases from ~90 to ~75%. However, according to Fig. 3.9(c), using the PAC/PTS(-)||(+YF-80F configuration, the performance loss is mitigated by applying 1.0 V, and the *SAC* remained at ~16 mg g<sup>-1</sup> ( $Q_E \approx 76\%$ ). Upon increasing  $E_{cell}$ , the *SAC* decreases 20.8% (1.1 V) and 37.3% (1.2 V), with concomitant  $Q_E$  drop (6.7% and 28.1% at 1.1 V and 1.2 V, respectively). However, the desalination stability seems to be achieved after ~55 and ~70 cycles applying 1.1 and 1.2 V, respectively (Fig. 3.9 (c)). In regard to  $\eta$ ,

according to Table 3.7, despite the SAC enhancement promoted by increasing  $E_{cell}$ , the use of high voltages also impacts the energy consumption. Indeed, the increase of the applied voltage from 1.0 to 1.1 V for PAC/PTS(-)||(+)-YP-80F increases the  $\eta$  by  $\sim 16\%$ , but does not bring a significant improvement in terms of SAC (only  $\sim 4\%$ ).

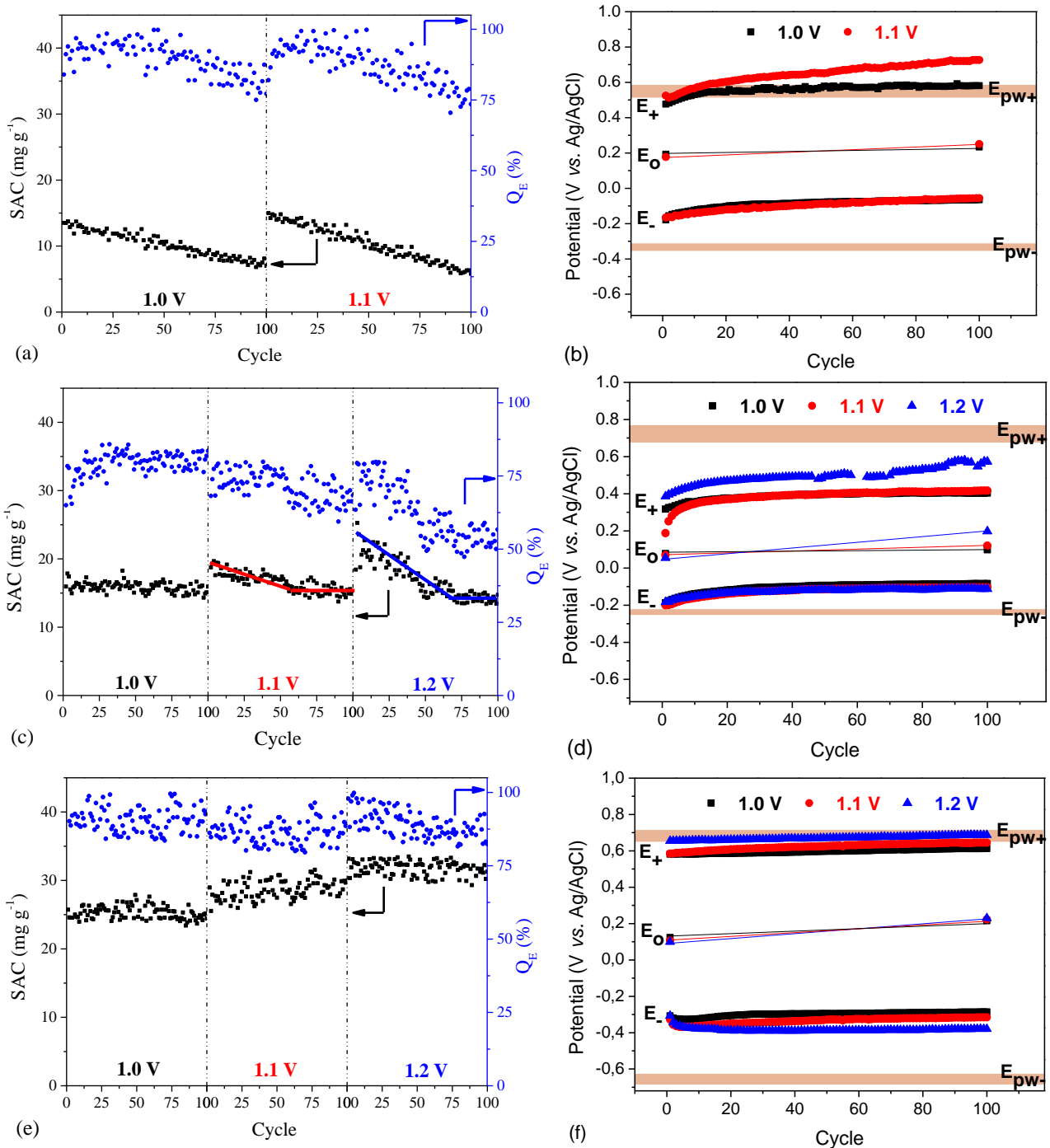


**Fig. 3.9.** SAC and  $Q_E$  throughout the desalination cycles operated at different  $E_{cell}$  for PAC/S(-)||(+)-sPAC/S (a), PAC/PTS(-)||(+)-YP-80F (c), and MCDI PAC/PTS (e) configurations. Electrode potential distributions for PAC/S(-)||(+)-sPAC/S (b), PAC/PTS(-)||(+)-YP-80F (d), and MCDI PAC/PTS (f) configurations. Electrolyte:  $1080 \text{ mg L}^{-1}$  NaCl. The standard deviation regarding the potential limits is 5%.

**Table 3.7.** Long-term electrosorption performance for the cell configurations achieving desalination stability.

CDI cell configuration	SAC (mg g <sup>-1</sup> )	Q <sub>E</sub> (%)	η (J mg <sup>-1</sup> )
PAC/PTS(-)    (+)YP-80F (1.0 V)	15.9 ± 0.7	75.7 ± 3.7	2.19 ± 0.12
PAC/PTS(-)    (+)YP-80F (1.1 V)*	16.6 ± 1.3	71.5 ± 4.9	2.55 ± 0.18
PAC/PTS(-)    (+)YP-80F (1.2 V)*	17.1 ± 2.9	62.1 ± 9.6	3.26 ± 0.48
MCDI PAC/PTS (1.0 V)	25.3 ± 0.9	90.6 ± 4.2	1.83 ± 0.08
MCDI PAC/PTS (1.1 V)	28.7 ± 1.4	86.6 ± 4.2	2.10 ± 0.10
MCDI PAC/PTS (1.2 V)	31.8 ± 1.3	89.3 ± 4.5	2.22 ± 0.11

\* The stability was achieved after a number of cycles.

The superior stability of PAC/PTS(-)||(+)-YP-80F compared to PAC/S(-)||(+)-sPAC/S configuration may be ascribed to the remarkable textural properties and higher intrinsic electrochemical stability of PAC/PTS and YP-80F. In order to better understand the stability of PAC/S, sPAC/S, PAC/PTS, and YP-80F electrodes, using or not IEMs, cyclic voltammograms were recorded at different vertex potentials (Fig. 3.10) and displayed as *R*-values (Eqs. 3.5 e 3.6) in Fig. 3.11. The limiting potentials for reduction ( $E_{PW-}$ ) and oxidation ( $E_{PW+}$ ), i.e., the PSW, were established by adopting  $R < 0.025$  as stability criterion. According to Fig. 3.11(a), PAC/S presents the lowest stability at positive potentials (lowest  $E_{PW+}$  at  $R = 0.025$ ), which aligns well with the prominent instability observed in the short-term desalination using symmetric PAC/S cells.

In the anodic regime, high reversible processes are observed for sPAC/S and YP-80F until 0.55 and 0.72 V vs. Ag/AgCl ( $R$ -values  $< 0.025$ ), respectively, indicating the predominance of the charge-storage mechanism in the EDL up to these potentials, in accordance with the quasi-rectangular shapes of the cyclic voltammograms displayed in Fig. 3.10. The lower oxidation potential limit of sPAC/S aligns well with its  $E_{PZC}$  that indicates the presence of more surface functional groups compared to YP-80F (Table 3.3, Fig. 3.7(a)), in agreement with the observation of other authors, who used different ACs [92,119]. When PAC/S and PAC/PTS electrodes are negatively polarized, there is a sharp increase of the *R*-values, indicating the narrow stability limits of these electrodes in the cathodic regime. Accordingly, the *R*-values surpass 0.025 at -0.33 V and -0.23 V vs. Ag/AgCl for PAC/S and PAC/PTS, respectively.

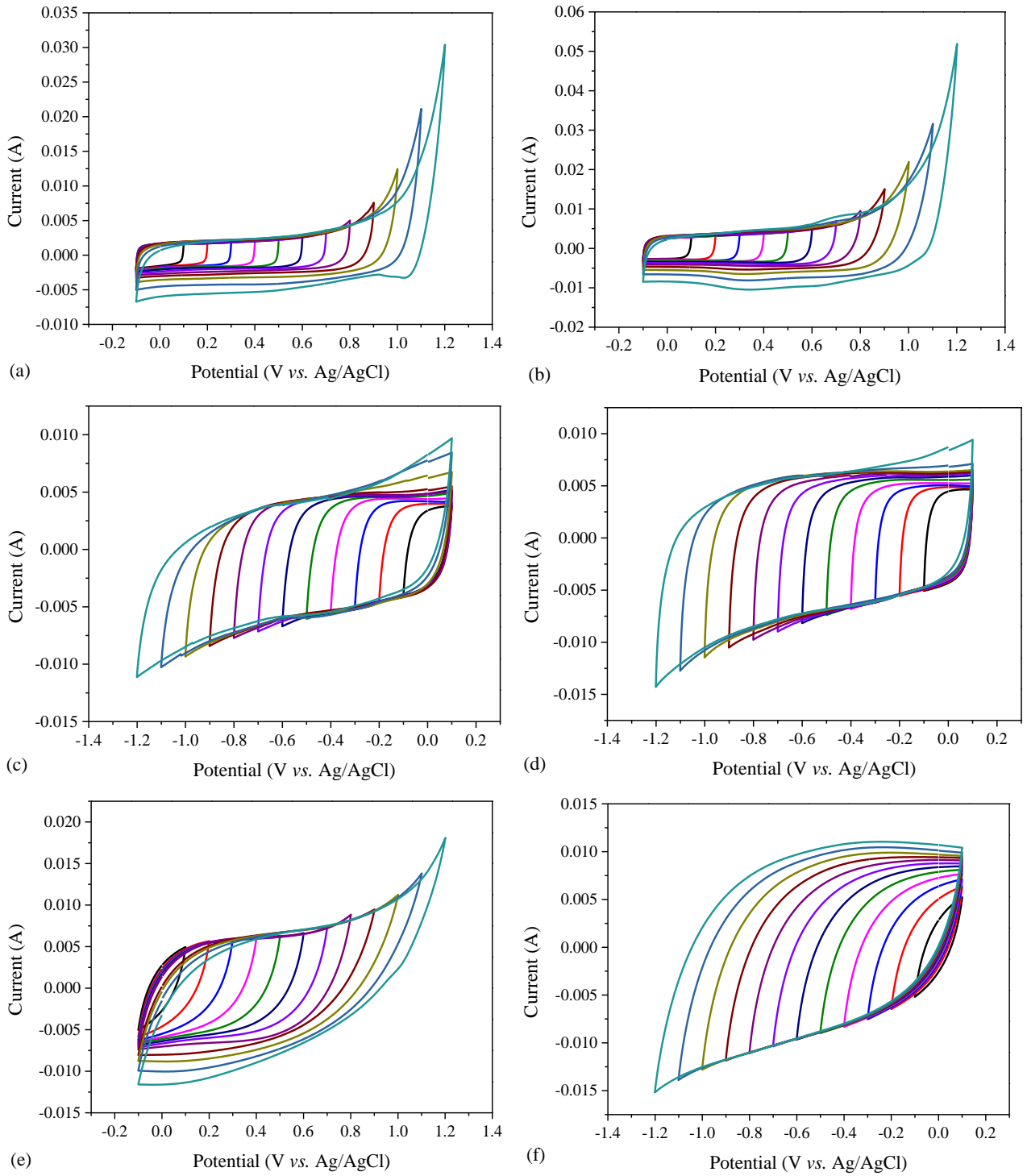


**Fig. 3.10.** Cyclic voltammograms recorded at  $5 \text{ mV s}^{-1}$  for sPAC/S (a), YP-80F (b), PAC/S (c), and PAC/PTS (d) electrodes without the use of IEMs, and for PAC/PTS using IEMs in the anodic (e), and cathodic (f) regimes. Electrolyte:  $1 \text{ mol L}^{-1} \text{ NaCl}$ .



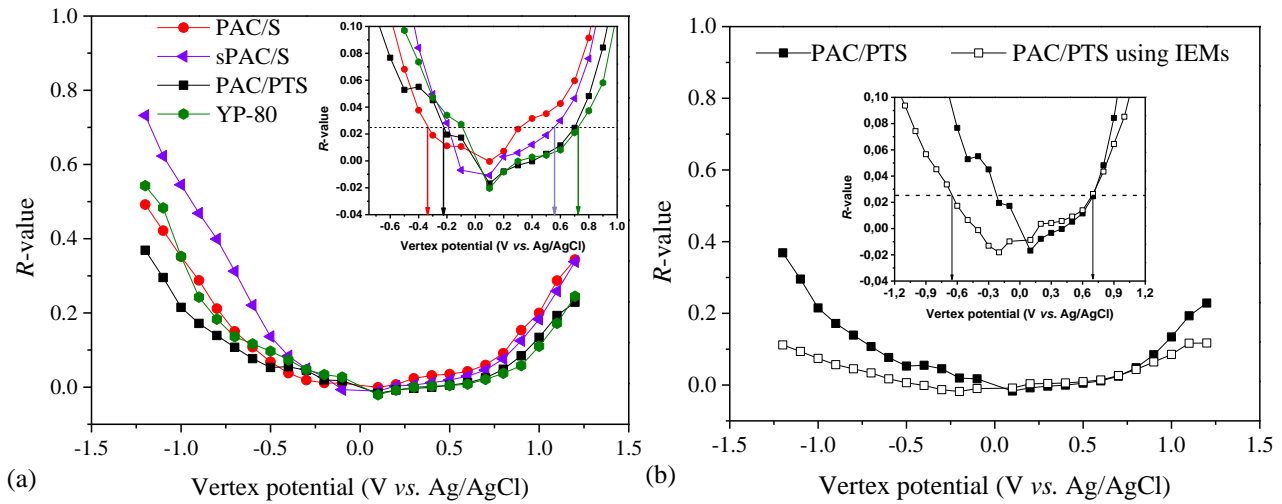


**Fig. 3.11.**  $R$ -value against the vertex potential for PAC/S, sPAC/S, PAC/PTS, and YP-80F (a), and for PAC/PTS using IEMs (b).

According to the potential profiles shown in Fig. 3.9, the stability potential limits are exceeded for some electrode configurations, e.g., for sPAC/S when polarized at 1.0 V, in which  $E_+$  starts at 0.48 V (1<sup>st</sup> cycle) and reach the  $E_{PW+}$  after only  $\sim 10$  cycles. Concomitantly,  $E_-$  is shifted to less negative values after 100 cycles (from -0.180 V to -0.065 V vs. Ag/AgCl), while  $E_0$  is shifted from 0.193 to 0.234 V vs. Ag/AgCl. Upon increasing the  $E_{cell}$  to 1.1 V, the potential of the positive electrode is already in the  $E_{PW+}$  range at the first cycle. Therefore, it can be concluded that the electrode instability observed for the PAC/S(-)||(+sPAC/S configuration is due to the oxidation reactions occurring at the positive electrode, since the values of  $E_+$  surpass the PSW. Accordingly, the superior stability achieved using PAC/PTS(-)||(+YP-80F configuration can be attributed to the more stable potential profiles that remained within the PSW for PAC/PTS (-0.23 V vs. Ag/AgCl) and YP-80F (0.72 V vs. Ag/AgCl) over the desalination cycles (Fig. 3.5(d)).

The PAC/PTS(-)||(+YP-80F configuration remained stable throughout the 100 cycles by applying 1.0 V, but at 1.1 and 1.2 V; although the  $E_+$  and  $E_-$  did not surpass the potential limits, an unexpected decrease in  $SAC$  is observed, suggesting that faradaic reactions may be occurring, particularly at the anode. It is well known that long-term performance can be affected by carbon oxidation reactions, such as those shown in Eqs. (3.14)-(3.16) [81,180]. An indication that these reactions occur is the  $E_{PZC}$  displacement to more positive values, confirming that the carbon surface becomes more negatively charged owing to the introduction of oxygen functional groups [121,167–169,181,182]. Accordingly, we observed  $E_{PZC}$  shifts of 0.3 V for the YP-80F electrode after 100 cycles applying both 1.1 or 1.2 V (Table 3.8), indicating that, although  $E_+$  is within the PSW, surface reactions probably occurred at potentials below the stability limits determined by the  $R$ -value approach. Indeed, this assumption is reinforced considering the  $E_+$  enhancement observed for the YP-

80F electrode polarized at 1.2 V, which could indicate the occurrence of redox processes at low potentials, which are not detected during the *R*-value analysis. Nevertheless, these redox processes seem to be a transient process, since the *SAC* reaches a steady value after some cycles, as previously discussed. It is also noteworthy that, according to Table 3.8,  $E_{PZC}$  shifts are observed for the PAC/PTS anode, even using membranes (0.1 V). In the case of the sPAC/S electrode, the  $E_{PZC}$  shifts are higher than 0.55 V, which would be expected, since the PSW is extrapolated and oxidation reactions occur at high positive potentials. Interestingly, considering all these aspects, a trend between the electrode stability and  $E_{PZC}$  displacement can be established. An electrode could be considered stable if the  $E_{PZC}$  shift is lower than 0.2 V, but for shifts higher than 0.55 V, the electrode loses electrochemical activity owing to more intensive oxidative processes occurring outside the stability window. It seems that in the range between  $0.2 < E_{PZC} \text{ shift} < 0.3$  V, transient redox reactions lead to an initial loss of *SAC*, but a steady-state is observed after a number of cycles, depending on the applied cell potential.



**Table 3.8.**  $E_{PZC}$  values of the positive electrodes before and after the long-term operation using the different asymmetric and MCDI configurations.

CDI cell configuration	$E_{PZC,0}$ (V)	$E_{PZC,100c}$ (V)	$E_{PZC}$ shift (V)
PAC/S(-)    (+)sPAC/S (1.0 V)	-0.20	0.35	0.55
PAC/S(-)    (+)sPAC/S (1.1 V)	-0.20	0.40	0.60
PAC/PTS(-)    (+)YP-80F (1.0 V)	0.00	0.20	0.20
PAC/PTS(-)    (+)YP-80F (1.1 V)	0.00	0.30	0.30
PAC/PTS(-)    (+)YP-80F (1.2 V)	0.00	0.30	0.30
MCDI PAC/PTS (1.0 V)	0.20	0.30	0.10
MCDI PAC/PTS (1.1 V)	0.20	0.30	0.10
MCDI PAC/PTS (1.2 V)	0.20	0.30	0.10

\* $E_{PZC,0}$ :  $E_{PZC}$  of the pristine electrodes;  $E_{PZC,100c}$ :  $E_{PZC}$  after 100 electrosorption/desorption cycles.

Using the MCDI PAC/PTS configuration, both electrosorption performance and stability are boosted, and a remarkable *SAC* ( $31.8 \pm 1.0 \text{ mg g}^{-1}$ ) is achieved at 1.2 V, with 100% of capability retention (Fig. 3.9(e)). Additionally,  $Q_E$  also remained at values higher than 80% throughout the process. On contrary to the observed for the other asymmetric configurations, despite the high

electrode potentials developed during the long-term operation, particularly at the cathode (Fig. 3.9(f)), a performance loss is not observed for MCDI since the potentials remain below or inside the PSW, according to Fig. 3.11(b). Interestingly, the  $E_{PW}$  was displaced to more negative values using IEMs (Fig. 3.11(b)), probably owing to the hindering of the dissolved oxygen transport to the cathode by the cationic membrane, avoiding the formation of peroxide species that can oxidize the carbon [81,183]. Furthermore, the small  $E_{PZC}$  shift (0.1 V) after 100 cycles reinforces the fact that the electrodes used in MCDI desalination remain stable.

Finally, the desalination performance using the MCDI PAC/PTS configuration at 1.2 V was compared to values reported in the CDI/MCDI literature and displayed in Table 3.9. The highest SAC values found in our search were reported by D. Li et al. [184] and Shi et al. [185], using N-rich microporous carbon materials derived from hexaazatriphenylene (30.8 mg g<sup>-1</sup>) and three-dimensional graphene networks and metal-organic frameworks-derived porous carbon rods (37.6 mg g<sup>-1</sup>) as electrode materials, respectively. Here, a superior SAC of 38.0 mg g<sup>-1</sup> and lower specific energy consumption (1.92 J mg<sup>-1</sup>) were achieved using PAC/PTS electrodes, which are of facile preparation using low-cost chemicals, besides remaining stable over 100 desalination cycles. Unfortunately, the references shown in Table 3.9 did not provide data about electrode stability over long-term operation. Considering all these aspects, PAC/PTS electrodes can be considered a promising candidate for large-scale MCDI applications.

**Table 3.9.** SAC and  $Q_E$  values reported in the literature using carbon materials as CDI electrode.

Electrode material	Configuration	Cell voltage (V)	[NaCl] (mg L <sup>-1</sup> )	SAC (mg g <sup>-1</sup> )	$Q_E$ (%)	$\eta$ (J mg <sup>-1</sup> )	References
Three-dimensional graphene networks and metal-organic frameworks (MOFs)-derived porous carbon rods	MCDI	1.2	1000	37.6	65	3.05	[185]
N,B-dual-doped porous carbon spheres	CDI	1.2	500	10.3	55	3.60	[186]
	MCDI	1.2	500	18.5	85	2.33	
Two-dimensional carbon nitride hexagonal-like sheets	MCDI	1.2	1000	30.8	-	-	[184]
Sugarcane biowaste-derived activated carbon	CDI	1.2	600	5.4	8	24.8	[48]
	MCDI	1.2	600	22.8	90	2.20	
Covalent triazine-based frameworks	MCDI	1.2	1000	29.3	-	-	[187]
Nitrogen-doped carbon nanotubes	MCDI	1.2	584.4	13.26	-	-	[188]
PAC/PTS	CDI	1.2	1080	18.0	71.6	2.77	This work
	MCDI	1.2	1080	38.0	99.2	1.92	

\*All electrodes were tested in recirculating batch mode.

## 4. Conclusions

Long-term stability is a paramount parameter for the effective application of activated carbons in CDI. In this work, we provided a comprehensive and systematic study of how the application of asymmetric electrode configurations and MCDI cells affects the desalination stability and performance. The use of asymmetric electrodes is an effective strategy to overcome the deleterious effect of co-ion expulsion and improve the short-term desalination performance. However, the increase of the electrode potential at the anode to values surpassing the stability limits and/or the  $E_{PZC}$  shift to values higher than 0.55 V lead to the  $SAC$  and  $Q_E$  drop for long-term operation. In this sense, the understanding of how the electrode potentials develop during the long-term operation is crucial to achieve a good performance stability with asymmetric cells.

The use of MCDI configuration demonstrated to be the best strategy to achieve high  $SAC$  and  $Q_E$ , leading to the lowest  $\eta$  among the electrode configurations, besides the excellent performance retention over the long-term operation. This remarkable stability and performance achieved using IEMs are attributed to the hindering of co-ion expulsion, concentration of co-ions in the macropores, and the reduction of the transport of active species across the IEM, thus preventing faradaic reactions. Although the use of IEM imposes an additional capital cost for CDI, the low specific energy consumption and the use of less expensive electrode materials, such as PAC/PTS, make MCDI competitive for large-scale applications. Accordingly, considering a concentration drop from 1000 mg L<sup>-1</sup> (brackish water) to 500 mg L<sup>-1</sup> (palatable limit), the electrode area required to produce 1.0 m<sup>3</sup> day<sup>-1</sup> of desalinated water is estimated as 3.3 m<sup>2</sup>, demanding 0.33 kg of PAC/PTS. Additionally, the low energy consumption (0.27 kWh) makes this process attractive from an economic point of view.

## CHAPTER 4

### CONCLUSIONS AND SUGGESTIONS FOR FUTURE WORKS

The importance of tuning the electrode porosity and thickness to improve the mass transfer and consequently the salt electrosorption capacity was evidenced. The ion-buffering reservoirs formed inside interparticle porosity can minimize the distance of ion diffusion from the bulk solution to the inner surface, facilitating the access of the ions to the micropores of the electrodes. In this sense, the electrodes produced by the doctor-blading procedure seem to be the best for CDI applications involving aqueous diluted salt electrolytes, since they present superior interparticle porosity, which leads to higher  $OSR_M$  values. However, if the electrosorption and desorption kinetics are not considered, a higher amount of salt can be removed using free-standing electrodes in a compact CDI cell. The effects of the electrode preparation procedures and electrode thicknesses were also observed on the specific energy consumption, revealing the importance of the electrode design not only for electrosorption, but also to minimize the energy requirements.

Improvements in desalination performance and stability in the long-term operation of PAC electrodes were also achieved by adopting cell configurations with ion-exchange membranes and asymmetric electrodes. In general, the understanding of how the electrode potentials develop and the  $E_{PZC}$  displaces in long-term desalination is crucial to improve the electrode stability in asymmetric cells, since the increase of the electrode potential at the anode to values surpassing the stability limits and/or the  $E_{PZC}$  shift to values higher than 0.55 V were responsible for the  $SAC$  and  $Q_E$  drop. The combination of the PAC and YP-80F electrodes revealed to be a promising asymmetric configuration, mainly due to the higher textural properties and intrinsic electrochemical stability of YP-80F when compared to the PAC treated with ethylenediamine and (3-aminopropyl)triethoxysilane. However, the introduction of ion-exchange membranes into CDI cells still seems to be the more feasible method to improve both electrosorption performance and stability by reducing the effect of co-ion expulsion and by limiting the transport across the IEM of the electrochemically active species responsible for faradaic reactions. In this sense, the best desalination performance was achieved using PAC/PTS electrodes in a MCDI configuration, obtaining a remarkable value of  $SAC$  ( $\sim 32 \text{ mg g}^{-1}$  at 1.2 V), 100% of  $SAC$  retention, and a small  $E_{PZC}$  shift (0.1 V) after 100 cycles.

Here, it was demonstrated efficient strategies to optimize the desalination capacity, enhance the adsorption/desorption kinetics, suppress the oxidation reactions, and improve the long-term

stability of PAC electrodes, paving the way to obtain optimized electrodes and cell configurations, specially aiming large-scale applications.

### **Suggestions for future works**

New insights about the adsorption/desorption kinetics and the electrode stability for long-term operation have been achieved in this thesis. However, other studies must be carried out to further improve and optimize the CDI technology, especially for large-scale applications. In this regard, the following suggestions are proposed for future works:

- The importance of the interparticle porosity in terms of salt adsorption capacity and electrosorption/desorption kinetics was evidenced in this work. Therefore, it is suggested to also employ the PAC/PTS for desalination in a flow-through configuration, since the access to the pores and mass transfer processes would be facilitated in this configuration;
- PAC/PTS showed a remarkable performance for long-term MCDI desalination. It is suggested to employ this electrode material for desalination of more concentrated solutions, and evaluate its performance in multicomponent solutions. A comprehensive study with more complex solutions with competing ions is needed for fully understanding the behavior of the electrode on a real system;
- Nowadays, there is an increasing interest in reducing the effect of co-ions expulsion and degradation of the positive electrode. Therefore, the development of new strategies to stabilize the positive electrode using low-cost electrodes is also suggested;
- A techno-economic analysis that links the lab-scale experimental performance to capital and operating costs of full-scale water production is also suggested in order to evaluate the financial viability of MCDI desalination using PAC/PTS electrodes.

## REFERENCES

- [1] M.M. Mekonnen, A.Y. Hoekstra, Four billion people facing severe water scarcity, *Sci. Adv.* 2 (2016) e1500323.
- [2] WWAP (UNESCO World Water Assessment Programme), *The United Nations World Water Development Report 2019: Leaving No One Behind*, 2019.
- [3] Agência Nacional de Águas, *Conjuntura dos recursos hídricos no Brasil 2019: informe anual / Agência Nacional de Águas*, (2019) 100.
- [4] N.C. Darre, G.S. Toor, Desalination of Water: a Review, *Curr. Pollut. Reports.* 4 (2018) 104–111. <https://doi.org/10.1007/s40726-018-0085-9>.
- [5] B. Van der Bruggen, C. Vandecasteele, Distillation vs. membrane filtration: Overview of process evolutions in seawater desalination, *Desalination.* 143 (2002) 207–218. [https://doi.org/10.1016/S0011-9164\(02\)00259-X](https://doi.org/10.1016/S0011-9164(02)00259-X).
- [6] E. Jones, M. Qadir, M.T.H. van Vliet, V. Smakhtin, S. mu Kang, The state of desalination and brine production: A global outlook, *Sci. Total Environ.* 657 (2019) 1343–1356. <https://doi.org/10.1016/j.scitotenv.2018.12.076>.
- [7] T. Younos, K.E. Tulou, Overview of Desalination Techniques, *J. Contemp. Water Res. Educ.* 132 (2009) 3–10. <https://doi.org/10.1111/j.1936-704x.2005.mp132001002.x>.
- [8] J. Kim, K. Park, D.R. Yang, S. Hong, A comprehensive review of energy consumption of seawater reverse osmosis desalination plants, *Appl. Energy.* 254 (2019) 113652. <https://doi.org/10.1016/j.apenergy.2019.113652>.
- [9] K.P. Lee, T.C. Arnot, D. Mattia, A review of reverse osmosis membrane materials for desalination-Development to date and future potential, *J. Memb. Sci.* 370 (2011) 1–22. <https://doi.org/10.1016/j.memsci.2010.12.036>.
- [10] L. Malaeb, G.M. Ayoub, Reverse osmosis technology for water treatment: State of the art review, *Desalination.* 267 (2011) 1–8. <https://doi.org/10.1016/j.desal.2010.09.001>.
- [11] M.A. Anderson, A.L. Cudero, J. Palma, Capacitive deionization as an electrochemical means of saving energy and delivering clean water. Comparison to present desalination practices:



- Will it compete?, *Electrochim. Acta.* 55 (2010) 3845–3856. <https://doi.org/10.1016/j.electacta.2010.02.012>.
- [12] K.B. Oldham, J.C. Myland, A.M. Bond, *Electrochemical Science and Technology: Fundamentals and Applications*, 2011. <https://doi.org/10.1002/9781119965992>.
- [13] A. Al-Karaghoul, L.L. Kazmerski, Energy consumption and water production cost of conventional and renewable-energy-powered desalination processes, *Renew. Sustain. Energy Rev.* 24 (2013) 343–356. <https://doi.org/10.1016/j.rser.2012.12.064>.
- [14] R. de O. Andrade, Removing salt from sea water, *Rev. Pesqui. FAPESP.* (2019). <https://revistapesquisa.fapesp.br/en/removing-salt-from-water/>.
- [15] M. Elimelech, W.A. Phillip, The future of seawater desalination: Energy, technology, and the environment, *Science* (80-. ). 333 (2011) 712–717. <https://doi.org/10.1126/science.1200488>.
- [16] F.S. Pinto, R.C. Marques, Desalination projects economic feasibility: A standardization of cost determinants, *Renew. Sustain. Energy Rev.* 78 (2017) 904–915. <https://doi.org/10.1016/j.rser.2017.05.024>.
- [17] M.E. Suss, S. Porada, X. Sun, P.M. Biesheuvel, J. Yoon, V. Presser, Water desalination via capacitive deionization: What is it and what can we expect from it?, *Energy Environ. Sci.* 8 (2015) 2296–2319. <https://doi.org/10.1039/c5ee00519a>.
- [18] S. Porada, R. Zhao, A. Van Der Wal, V. Presser, P.M. Biesheuvel, Review on the science and technology of water desalination by capacitive deionization, *Prog. Mater. Sci.* 58 (2013) 1388–1442. <https://doi.org/10.1016/j.pmatsci.2013.03.005>.
- [19] X. Xu, L. Pan, Y. Liu, T. Lu, Z. Sun, Enhanced capacitive deionization performance of graphene by nitrogen doping, *J. Colloid Interface Sci.* 445 (2015) 143–150. <https://doi.org/10.1016/j.jcis.2015.01.003>.
- [20] P. Długołęcki, A. van der Wal, Energy Recovery in Membrane Capacitive Deionization, *Environ. Sci. Technol.* 47 (2013) 4904–4910. <https://doi.org/10.1021/es3053202>.
- [21] J.E. Dykstra, S. Porada, A. van der Wal, P.M. Biesheuvel, Energy consumption in capacitive deionization – Constant current versus constant voltage operation, *Water Res.* 143 (2018) 367–

375. <https://doi.org/10.1016/j.watres.2018.06.034>.

- [22] T. Matsunaga, S. Nakasono, Y. Kitajima, K. Horiguchi, Electrochemical disinfection of bacteria in drinking water using activated carbon fibers, *Biotechnol. Bioeng.* 43 (1994) 429–433. <https://doi.org/10.1002/bit.260430511>.
- [23] B. van Limpt, Performance relations in capacitive deionization systems, 2010.
- [24] A. Ramachandran, D.I. Oyarzun, S.A. Hawks, P.G. Campbell, M. Stadermann, J.G. Santiago, Comments on “Comparison of energy consumption in desalination by capacitive deionization and reverse osmosis,” *Desalination.* 461 (2019) 30–36. <https://doi.org/10.1016/j.desal.2019.03.010>.
- [25] J.C. Farmer, D. V. Fix, G. V. Mack, R.W. Pekala, J.F. Poco, Capacitive Deionization of NaCl and NaNO<sub>3</sub> Solutions with Carbon Aerogel Electrodes, *J. Electrochem. Soc.* 143 (1996) 159–169. <https://doi.org/10.1149/1.1836402>.
- [26] A.M. Johnson, J. Newman, Desalting by Means of Porous Carbon Electrodes, *J. Electrochem. Soc.* 118 (1971) 510. <https://doi.org/10.1149/1.2408094>.
- [27] A.M. Johnson, A.W. Venolia, J. Newman, R.G. Wilbourne, C.M. Wong, W.S. Gillam, S. Johnson, R.H. Horowitz, Electrosorb process for desalting water, Office of Saline Water Research and Development, in: Prog. Rep. No 516, US Dep. Inter. Publ. 200 056, 1970.
- [28] A. Johnson, Electric demineralizing apparatus, US3755135A, 1973.
- [29] J.C. Farmer, D. V Fix, G. V Mack, R.W. Pekala, J.F. Poco, Capacitive Deionization of NaCl and NaNO<sub>3</sub> Solutions with Carbon Aerogel Electrodes, *J. Electrochem. Soc.* 143 (1996) 159–169. <https://doi.org/10.1149/1.1836402>.
- [30] M.A. Ahmed, S. Tewari, Capacitive deionization: Processes, materials and state of the technology, *J. Electroanal. Chem.* 813 (2018) 178–192. <https://doi.org/10.1016/j.jelechem.2018.02.024>.
- [31] J. Choi, P. Dorji, H.K. Shon, S. Hong, Applications of capacitive deionization: Desalination, softening, selective removal, and energy efficiency, *Desalination.* 449 (2019) 118–130. <https://doi.org/10.1016/j.desal.2018.10.013>.

- [32] K. Dai, L. Shi, J. Fang, D. Zhang, B. Yu, NaCl adsorption in multi-walled carbon nanotubes, *Mater. Lett.* 59 (2005) 1989–1992. <https://doi.org/10.1016/j.matlet.2005.01.042>.
- [33] H. Li, Y. Gao, L. Pan, Y. Zhang, Y. Chen, Z. Sun, Electrosorptive desalination by carbon nanotubes and nanofibres electrodes and ion-exchange membranes, *Water Res.* 42 (2008) 4923–4928. <https://doi.org/10.1016/j.watres.2008.09.026>.
- [34] H. Li, L. Zou, L. Pan, Z. Sun, Novel Graphene-Like Electrodes for Capacitive Deionization, *Environ. Sci. Technol.* 44 (2010) 8692–8697. <https://doi.org/10.1021/es101888j>.
- [35] Y. Chen, X. Zhang, H. Zhang, X. Sun, D. Zhang, Y. Ma, High-performance supercapacitors based on a graphene-activated carbon composite prepared by chemical activation, *RSC Adv.* 2 (2012) 7747–7753. <https://doi.org/10.1039/c2ra20667f>.
- [36] W. Shi, H. Li, X. Cao, Z.Y. Leong, J. Zhang, T. Chen, H. Zhang, H.Y. Yang, Ultrahigh Performance of Novel Capacitive Deionization Electrodes based on A Three-Dimensional Graphene Architecture with Nanopores, *Sci. Rep.* 6 (2016) 18966. <https://doi.org/10.1038/srep18966>.
- [37] K.L. Yang, T.Y. Ying, S. Yiacoumi, C. Tsouris, E.S. Vittoratos, Electrosorption of ions from aqueous solutions by carbon aerogel: An electrical double-layer model, *Langmuir.* 17 (2001) 1961–1969. <https://doi.org/10.1021/la001527s>.
- [38] C.M. Yang, W.H. Choi, B.K. Na, B.W. Cho, W. Il Cho, Capacitive deionization of NaCl solution with carbon aerogel-silicagel composite electrodes, *Desalination.* 174 (2005) 125–133. <https://doi.org/10.1016/j.desal.2004.09.006>.
- [39] G. Rasines, P. Lavela, C. Macías, M. Haro, C.O. Ania, J.L. Tirado, Electrochemical response of carbon aerogel electrodes in saline water, *J. Electroanal. Chem.* 671 (2012) 92–98. <https://doi.org/10.1016/j.jelechem.2012.02.025>.
- [40] M.C. Zafra, P. Lavela, C. Macías, G. Rasines, J.L. Tirado, Electrosorption of environmental concerning anions on a highly porous carbon aerogel, *J. Electroanal. Chem.* 708 (2013) 80–86. <https://doi.org/10.1016/j.jelechem.2013.09.020>.
- [41] C. Kim, P. Srimuk, J. Lee, S. Fleischmann, M. Aslan, V. Presser, Influence of pore structure and cell voltage of activated carbon cloth as a versatile electrode material for capacitive

- deionization, *Carbon* N. Y. 122 (2017) 329–335. <https://doi.org/10.1016/j.carbon.2017.06.077>.
- [42] G.X. Li, P.X. Hou, S.Y. Zhao, C. Liu, H.M. Cheng, A flexible cotton-derived carbon sponge for high-performance capacitive deionization, *Carbon* N. Y. 101 (2016) 1–8. <https://doi.org/10.1016/j.carbon.2015.12.095>.
- [43] M. Aslan, M. Zeiger, N. Jäckel, I. Grobelsek, D. Weingarth, V. Presser, Improved capacitive deionization performance of mixed hydrophobic/hydrophilic activated carbon electrodes, *J. Phys. Condens. Matter*. 28 (2016) 114003. <https://doi.org/10.1088/0953-8984/28/11/114003>.
- [44] S. Porada, L. Weinstein, R. Dash, A. Van Der Wal, M. Bryjak, Y. Gogotsi, P.M. Biesheuvel, Water desalination using capacitive deionization with microporous carbon electrodes, *ACS Appl. Mater. Interfaces*. 4 (2012) 1194–1199. <https://doi.org/10.1021/am201683j>.
- [45] C.L. Yeh, H.C. Hsi, K.C. Li, C.H. Hou, Improved performance in capacitive deionization of activated carbon electrodes with a tunable mesopore and micropore ratio, *Desalination*. 367 (2015) 60–68. <https://doi.org/10.1016/j.desal.2015.03.035>.
- [46] C.H. Hou, N.L. Liu, H.C. Hsi, Highly porous activated carbons from resource-recovered *Leucaena leucocephala* wood as capacitive deionization electrodes, *Chemosphere*. 141 (2015) 71–79. <https://doi.org/10.1016/j.chemosphere.2015.06.055>.
- [47] Y.C. Tsai, R.A. Doong, Activation of hierarchically ordered mesoporous carbons for enhanced capacitive deionization application, *Synth. Met.* 205 (2015) 48–57. <https://doi.org/10.1016/j.synthmet.2015.03.026>.
- [48] J.J. Lado, R.L. Zornitta, I. Vázquez Rodríguez, K. Malverdi Barcelos, L.A.M. Ruotolo, Sugarcane Biowaste-Derived Biochars as Capacitive Deionization Electrodes for Brackish Water Desalination and Water-Softening Applications, *ACS Sustain. Chem. Eng.* 7 (2019) 18992–19004. <https://doi.org/10.1021/acssuschemeng.9b04504>.
- [49] P. Liu, H. Wang, T. Yan, J. Zhang, L. Shi, D. Zhang, Grafting sulfonic and amine functional groups on 3D graphene for improved capacitive deionization, *J. Mater. Chem. A*. 4 (2016) 5303–5313. <https://doi.org/10.1039/c5ta10680j>.
- [50] C.T. Hsieh, H. Teng, Influence of oxygen treatment on electric double-layer capacitance of

activated carbon fabrics, *Carbon N. Y.* 40 (2002) 667–674. [https://doi.org/10.1016/S0008-6223\(01\)00182-8](https://doi.org/10.1016/S0008-6223(01)00182-8).

- [51] X. Gao, A. Omosebi, J. Landon, K. Liu, Surface charge enhanced carbon electrodes for stable and efficient capacitive deionization using inverted adsorption–desorption behavior, *Energy Environ. Sci.* 8 (2015) 897–909. <https://doi.org/10.1039/C4EE03172E>.
- [52] R.L. Zornitta, F.J. García-Mateos, J.J. Lado, J. Rodríguez-Mirasol, T. Cordero, P. Hammer, L.A.M. Ruotolo, High-performance activated carbon from polyaniline for capacitive deionization, *Carbon N. Y.* 123 (2017) 318–333. <https://doi.org/10.1016/j.carbon.2017.07.071>.
- [53] J.J. Lado, R.L. Zornitta, F.A. Calvi, M. Martins, M.A. Anderson, F.G.E. Nogueira, L.A.M. Ruotolo, Enhanced capacitive deionization desalination provided by chemical activation of sugar cane bagasse fly ash electrodes, *J. Anal. Appl. Pyrolysis.* 126 (2017) 143–153. <https://doi.org/10.1016/j.jaap.2017.06.014>.
- [54] H. Yin, S. Zhao, J. Wan, H. Tang, L. Chang, L. He, H. Zhao, Y. Gao, Z. Tang, Three-Dimensional Graphene/Metal Oxide Nanoparticle Hybrids for High-Performance Capacitive Deionization of Saline Water, *Adv. Mater.* 25 (2013) 6270–6276. <https://doi.org/10.1002/adma.201302223>.
- [55] M.T.Z. Myint, J. Dutta, Fabrication of zinc oxide nanorods modified activated carbon cloth electrode for desalination of brackish water using capacitive deionization approach, *Desalination.* 305 (2012) 24–30. <https://doi.org/10.1016/j.desal.2012.08.010>.
- [56] K. Laxman, M.T.Z. Myint, H. Bourdoucen, J. Dutta, Enhancement in ion adsorption rate and desalination efficiency in a capacitive deionization cell through improved electric field distribution using electrodes composed of activated carbon cloth coated with zinc oxide nanorods, *ACS Appl. Mater. Interfaces.* 6 (2014) 10113–10120. <https://doi.org/10.1021/am501041t>.
- [57] K. Laxman, M.T.Z. Myint, R. Khan, T. Pervez, J. Dutta, Improved desalination by zinc oxide nanorod induced electric field enhancement in capacitive deionization of brackish water, *Desalination.* 359 (2015) 64–70. <https://doi.org/10.1016/j.desal.2014.12.029>.

- [58] K. Laxman, M.T.Z. Myint, R. Khan, T. Pervez, J. Dutta, Effect of a semiconductor dielectric coating on the salt adsorption capacity of a porous electrode in a capacitive deionization cell, *Electrochim. Acta.* 166 (2015) 329–337. <https://doi.org/10.1016/j.electacta.2015.03.049>.
- [59] J. Yang, L. Zou, H. Song, Z. Hao, Development of novel MnO<sub>2</sub>/nanoporous carbon composite electrodes in capacitive deionization technology, *Desalination.* 276 (2011) 199–206. <https://doi.org/10.1016/j.desal.2011.03.044>.
- [60] A.G. El-Deen, N.A.M. Barakat, H.Y. Kim, Graphene wrapped MnO<sub>2</sub>-nanostructures as effective and stable electrode materials for capacitive deionization desalination technology, *Desalination.* 344 (2014) 289–298. <https://doi.org/10.1016/j.desal.2014.03.028>.
- [61] A.G. El-Deen, J.H. Choi, C.S. Kim, K.A. Khalil, A.A. Almajid, N.A.M. Barakat, TiO<sub>2</sub> nanorod-intercalated reduced graphene oxide as high performance electrode material for membrane capacitive deionization, *Desalination.* 361 (2015) 53–64. <https://doi.org/10.1016/j.desal.2015.01.033>.
- [62] J. Lee, P. Srimuk, S. Carpier, J. Choi, R.L. Zornitta, C. Kim, M. Aslan, V. Presser, Confined Redox Reactions of Iodide in Carbon Nanopores for Fast and Energy-Efficient Desalination of Brackish Water and Seawater, *ChemSusChem.* 11 (2018) 3460–3472. <https://doi.org/10.1002/cssc.201801538>.
- [63] C. Zhang, D. He, J. Ma, W. Tang, T.D. Waite, Faradaic reactions in capacitive deionization (CDI) - problems and possibilities: A review, *Water Res.* 128 (2018) 314–330. <https://doi.org/10.1016/j.watres.2017.10.024>.
- [64] P. Srimuk, J. Halim, J. Lee, Q. Tao, J. Rosen, V. Presser, Two-Dimensional Molybdenum Carbide (MXene) with Divacancy Ordering for Brackish and Seawater Desalination via Cation and Anion Intercalation, *ACS Sustain. Chem. Eng.* 6 (2018) 3739–3747. <https://doi.org/10.1021/acssuschemeng.7b04095>.
- [65] P. Srimuk, F. Kaasik, B. Krüner, A. Tolosa, S. Fleischmann, N. Jäckel, M.C. Tekeli, M. Aslan, M.E. Suss, V. Presser, MXene as a novel intercalation-type pseudocapacitive cathode and anode for capacitive deionization, *J. Mater. Chem. A.* 4 (2016) 18265–18271. <https://doi.org/10.1039/c6ta07833h>.

- [66] H. Yoon, J. Lee, S. Kim, J. Yoon, Hybrid capacitive deionization with Ag coated carbon composite electrode, *Desalination*. 422 (2017) 42–48. <https://doi.org/10.1016/j.desal.2017.08.010>.
- [67] P. Srimuk, J. Lee, S. Fleischmann, S. Choudhury, N. Jäckel, M. Zeiger, C. Kim, M. Aslan, V. Presser, Faradaic deionization of brackish and sea water via pseudocapacitive cation and anion intercalation into few-layered molybdenum disulfide, *J. Mater. Chem. A*. 5 (2017) 15640–15649. <https://doi.org/10.1039/c7ta03120c>.
- [68] F. Xing, T. Li, J. Li, H. Zhu, N. Wang, X. Cao, Chemically exfoliated MoS<sub>2</sub> for capacitive deionization of saline water, *Nano Energy*. 31 (2017) 590–595. <https://doi.org/10.1016/j.nanoen.2016.12.012>.
- [69] J. Lee, S. Kim, C. Kim, J. Yoon, Hybrid capacitive deionization to enhance the desalination performance of capacitive techniques, *Energy Environ. Sci*. 7 (2014) 3683–3689. <https://doi.org/10.1039/c4ee02378a>.
- [70] S. Kim, J. Lee, C. Kim, J. Yoon, Na<sub>2</sub>FeP<sub>2</sub>O<sub>7</sub> as a Novel Material for Hybrid Capacitive Deionization, *Electrochim. Acta*. 203 (2016) 265–271. <https://doi.org/10.1016/j.electacta.2016.04.056>.
- [71] J. Lee, S. Kim, J. Yoon, Rocking Chair Desalination Battery Based on Prussian Blue Electrodes, *ACS Omega*. 2 (2017) 1653–1659. <https://doi.org/10.1021/acsomega.6b00526>.
- [72] S. Porada, A. Shrivastava, P. Bukowska, P.M. Biesheuvel, K.C. Smith, Nickel Hexacyanoferrate Electrodes for Continuous Cation Intercalation Desalination of Brackish Water, *Electrochim. Acta*. 255 (2017) 369–378. <https://doi.org/10.1016/j.electacta.2017.09.137>.
- [73] J. Lee, P. Srimuk, K. Aristizabal, C. Kim, S. Choudhury, Y.C. Nah, F. Mücklich, V. Presser, Pseudocapacitive Desalination of Brackish Water and Seawater with Vanadium-Pentoxide-Decorated Multiwalled Carbon Nanotubes, *ChemSusChem*. 10 (2017) 3611–3623. <https://doi.org/10.1002/cssc.201701215>.
- [74] P. Srimuk, J. Lee, A. Tolosa, C. Kim, M. Aslan, V. Presser, Titanium Disulfide: A Promising Low-Dimensional Electrode Material for Sodium Ion Intercalation for Seawater Desalination,

Chem. Mater. 29 (2017) 9964–9973. <https://doi.org/10.1021/acs.chemmater.7b03363>.

- [75] M. Salanne, B. Rotenberg, K. Naoi, K. Kaneko, P.-L. Taberna, C.P. Grey, B. Dunn, P. Simon, Efficient storage mechanisms for building better supercapacitors, *Nat. Energy*. 1 (2016) 16070. <https://doi.org/10.1038/nenergy.2016.70>.
- [76] M.E. Suss, V. Presser, Water Desalination with Energy Storage Electrode Materials, *Joule*. 2 (2018) 10–15. <https://doi.org/10.1016/j.joule.2017.12.010>.
- [77] P.M. Biesheuvel, A. van der Wal, Membrane capacitive deionization, *J. Memb. Sci.* 346 (2010) 256–262. <https://doi.org/10.1016/j.memsci.2009.09.043>.
- [78] P. Liang, X. Sun, Y. Bian, H. Zhang, X. Yang, Y. Jiang, Optimized desalination performance of high voltage flow-electrode capacitive deionization by adding carbon black in flow-electrode, *Desalination*. 420 (2017) 63–69. <https://doi.org/10.1016/j.desal.2017.05.023>.
- [79] R. Zhao, P.M. Biesheuvel, A. Van Der Wal, Energy consumption and constant current operation in membrane capacitive deionization, *Energy Environ. Sci.* 5 (2012) 9520–9527. <https://doi.org/10.1039/c2ee21737f>.
- [80] P.M. Biesheuvel, R. Zhao, S. Porada, A. van der Wal, Theory of membrane capacitive deionization including the effect of the electrode pore space, *J. Colloid Interface Sci.* 360 (2011) 239–248. <https://doi.org/10.1016/j.jcis.2011.04.049>.
- [81] A. Omosibi, X. Gao, J. Landon, K. Liu, Asymmetric Electrode Configuration for Enhanced Membrane Capacitive Deionization, *ACS Appl. Mater. Interfaces*. 6 (2014) 12640–12649. <https://doi.org/10.1021/am5026209>.
- [82] J.-H. Choi, Determination of the electrode potential causing Faradaic reactions in membrane capacitive deionization, *Desalination*. 347 (2014) 224–229. <https://doi.org/10.1016/j.desal.2014.06.004>.
- [83] S. Il Jeon, H.R. Park, J.G. Yeo, S. Yang, C.H. Cho, M.H. Han, D.K. Kim, Desalination via a new membrane capacitive deionization process utilizing flow-electrodes, *Energy Environ. Sci.* 6 (2013) 1471–1475. <https://doi.org/10.1039/c3ee24443a>.
- [84] S. Yang, H. Kim, S. Jeon, J. Choi, J. Yeo, H. Park, J. Jin, D. Kook, Analysis of the desalting



performance of flow-electrode capacitive deionization under short-circuited closed cycle operation, *Desalination*. 424 (2017) 110–121. <https://doi.org/10.1016/j.desal.2017.09.032>.

- [85] X. Gu, Y. Yang, Y. Hu, M. Hu, J. Huang, C. Wang, Nitrogen-doped graphene composites as efficient electrodes with enhanced capacitive deionization performance, *RSC Adv.* 4 (2014) 63189–63199. <https://doi.org/10.1039/C4RA11468J>.
- [86] Y. Liu, X. Xu, T. Lu, Z. Sun, D.H.C. Chua, L. Pan, Nitrogen-doped electrospun reduced graphene oxide–carbon nanofiber composite for capacitive deionization, *RSC Adv.* 5 (2015) 34117–34124. <https://doi.org/10.1039/C5RA00620A>.
- [87] X. Xu, Z. Sun, D.H.C. Chua, L. Pan, Novel nitrogen doped graphene sponge with ultrahigh capacitive deionization performance, *Sci. Rep.* 5 (2015) 11225. <https://doi.org/10.1038/srep11225>.
- [88] Z. Zhang, Z. Zhou, H. Peng, Y. Qin, G. Li, Nitrogen- and oxygen-containing hierarchical porous carbon frameworks for high-performance supercapacitors, *Electrochim. Acta.* 134 (2014) 471–477. <https://doi.org/10.1016/j.electacta.2014.04.107>.
- [89] N.D. Kim, W. Kim, J.B. Joo, S. Oh, P. Kim, Y. Kim, J. Yi, Electrochemical capacitor performance of N-doped mesoporous carbons prepared by ammoxidation, *J. Power Sources.* 180 (2008) 671–675. <https://doi.org/10.1016/j.jpowsour.2008.01.055>.
- [90] X. Wang, J.S. Lee, Q. Zhu, J. Liu, Y. Wang, S. Dai, Ammonia-treated ordered mesoporous carbons as catalytic materials for oxygen reduction reaction, *Chem. Mater.* 22 (2010) 2178–2180. <https://doi.org/10.1021/cm100139d>.
- [91] P. Chen, T.Y. Xiao, Y.H. Qian, S.S. Li, S.H. Yu, A nitrogen-doped graphene/carbon nanotube nanocomposite with synergistically enhanced electrochemical activity, *Adv. Mater.* 25 (2013) 3192–3196. <https://doi.org/10.1002/adma.201300515>.
- [92] S. Porada, F. Schipper, M. Aslan, M. Antonietti, V. Presser, T.P. Fellingner, Capacitive deionization using biomass-based microporous salt-templated heteroatom-doped carbons, *ChemSusChem.* 8 (2015) 1867–1874. <https://doi.org/10.1002/cssc.201500166>.
- [93] J. Shi, N. Yan, H. Cui, Y. Liu, Y. Weng, D. Li, X. Ji, Nitrogen doped hierarchically porous carbon derived from glucosamine hydrochloride for CO<sub>2</sub> adsorption, *J. CO<sub>2</sub> Util.* 21 (2017)

444–449. <https://doi.org/10.1016/j.jcou.2017.08.010>.

- [94] X. Yang, D. Wu, X. Chen, R. Fu, Nitrogen-enriched nanocarbons with a 3-D continuous mesopore structure from polyacrylonitrile for supercapacitor application, *J. Phys. Chem. C*. 114 (2010) 8581–8586. <https://doi.org/10.1021/jp101255d>.
- [95] L. Zheng, W.B. Li, J.L. Chen, Nitrogen doped hierarchical activated carbons derived from polyacrylonitrile fibers for CO<sub>2</sub> adsorption and supercapacitor electrodes, *RSC Adv.* 8 (2018) 29767–29774. <https://doi.org/10.1039/c8ra04367a>.
- [96] J. Yan, T. Wei, W. Qiao, Z. Fan, L. Zhang, T. Li, Q. Zhao, A high-performance carbon derived from polyaniline for supercapacitors, *Electrochem. Commun.* 12 (2010) 1279–1282. <https://doi.org/10.1016/j.elecom.2010.06.037>.
- [97] E. Qezselfloo, S. Khalili, M. Jahanshahi, M. Peyravi, Adsorptive removal of CO<sub>2</sub> on Nitrogen-doped porous carbon derived from polyaniline: Effect of chemical activation, *Mater. Chem. Phys.* 239 (2020) 122304. <https://doi.org/10.1016/j.matchemphys.2019.122304>.
- [98] M.J. Mostazo-López, D. Salinas-Torres, R. Ruiz-Rosas, E. Morallón, D. Cazorla-Amorós, Nitrogen-doped superporous activated carbons as electrocatalysts for the oxygen reduction reaction, *Materials (Basel)*. 12 (2019) 1–17. <https://doi.org/10.3390/ma12081346>.
- [99] A.B. Fuertes, T.A. Centeno, Mesoporous carbons with graphitic structures fabricated by using porous silica materials as templates and iron-impregnated polypyrrole as precursor, *J. Mater. Chem.* 15 (2005) 1079–1083. <https://doi.org/10.1039/b416007j>.
- [100] L. Li, E. Liu, J. Li, Y. Yang, H. Shen, Z. Huang, X. Xiang, W. Li, A doped activated carbon prepared from polyaniline for high performance supercapacitors, *J. Power Sources*. 195 (2010) 1516–1521. <https://doi.org/10.1016/j.jpowsour.2009.09.016>.
- [101] G. Wu, K.L. More, C.M. Johnston, P. Zelenay, High-performance electrocatalysts for oxygen reduction derived from polyaniline, iron, and cobalt, *Science (80-. )*. 332 (2011) 443–447. <https://doi.org/10.1126/science.1200832>.
- [102] N. Gavrilov, I.A. Pašti, M. Vujković, J. Travas-Sejdic, G. Ćirić-Marjanović, S. V. Mentus, High-performance charge storage by N-containing nanostructured carbon derived from polyaniline, *Carbon* N. Y. 50 (2012) 3915–3927.

<https://doi.org/10.1016/j.carbon.2012.04.045>.

- [103] Y. Jia, J. Jiang, K. Sun, Pyrolysis of polyaniline–poly(styrene sulfonate) hydrogels to prepare activated carbons for the adsorption of vitamin B12, *J. Anal. Appl. Pyrolysis*. 111 (2015) 247–253. <https://doi.org/10.1016/j.jaap.2014.10.023>.
- [104] J.W.F. To, Z. Chen, H. Yao, J. He, K. Kim, H.-H. Chou, L. Pan, J. Wilcox, Y. Cui, Z. Bao, Ultrahigh Surface Area Three-Dimensional Porous Graphitic Carbon from Conjugated Polymeric Molecular Framework, *ACS Cent. Sci.* 1 (2015) 68–76. <https://doi.org/10.1021/acscentsci.5b00149>.
- [105] M. Yang, B. Cheng, H. Song, X. Chen, Preparation and electrochemical performance of polyaniline-based carbon nanotubes as electrode material for supercapacitor, *Electrochim. Acta*. 55 (2010) 7021–7027. <https://doi.org/10.1016/j.electacta.2010.06.077>.
- [106] X. Xiang, E. Liu, Z. Huang, H. Shen, Y. Tian, C. Xiao, J. Yang, Z. Mao, Preparation of activated carbon from polyaniline by zinc chloride activation as supercapacitor electrodes, *J. Solid State Electrochem.* 15 (2011) 2667–2674. <https://doi.org/10.1007/s10008-010-1258-7>.
- [107] K.S. Kim, S.J. Park, Easy synthesis of polyaniline-based mesoporous carbons and their high electrochemical performance, *Microporous Mesoporous Mater.* 163 (2012) 140–146. <https://doi.org/10.1016/j.micromeso.2012.04.047>.
- [108] M. Vujković, N. Gavrilov, I. Pašti, J. Krstić, J. Travas-Sejdic, G. Ćirić-Marjanović, S. Mentus, Superior capacitive and electrocatalytic properties of carbonized nanostructured polyaniline upon a low-temperature hydrothermal treatment, *Carbon N. Y.* 64 (2013) 472–486. <https://doi.org/10.1016/j.carbon.2013.07.100>.
- [109] Y. Wang, L. Zhang, Y. Wu, S. Xu, J. Wang, Polypyrrole/carbon nanotube composites as cathode material for performance enhancing of capacitive deionization technology, *Desalination*. 354 (2014) 62–67. <https://doi.org/10.1016/j.desal.2014.09.021>.
- [110] T. Zhu, J. Zhou, Z. Li, S. Li, W. Si, S. Zhuo, Hierarchical porous and N-doped carbon nanotubes derived from polyaniline for electrode materials in supercapacitors, *J. Mater. Chem. A*. 2 (2014) 12545–12551. <https://doi.org/10.1039/c4ta01465k>.
- [111] R.L. Zornitta, L.A.M. Ruotolo, Simultaneous analysis of electrosorption capacity and kinetics

- for CDI desalination using different electrode configurations, *Chem. Eng. J.* 332 (2018) 33–41. <https://doi.org/10.1016/j.cej.2017.09.067>.
- [112] R.L. Zornitta, K.M. Barcelos, F.G.E. Nogueira, L.A.M. Ruotolo, Understanding the mechanism of carbonization and KOH activation of polyaniline leading to enhanced electrosorption performance, *Carbon* N. Y. 156 (2020) 346–358. <https://doi.org/10.1016/j.carbon.2019.09.058>.
- [113] L. Zou, L. Li, H. Song, G. Morris, Using mesoporous carbon electrodes for brackish water desalination, 42 (2008) 2340–2348. <https://doi.org/10.1016/j.watres.2007.12.022>.
- [114] X. Xu, Y. Liu, M. Wang, C. Zhu, T. Lu, R. Zhao, L. Pan, Hierarchical hybrids with microporous carbon spheres decorated three-dimensional graphene frameworks for capacitive applications in supercapacitor and deionization, *Electrochim. Acta.* 193 (2016) 88–95. <https://doi.org/10.1016/j.electacta.2016.02.049>.
- [115] L. Han, K.G. Karthikeyan, M.A. Anderson, K.B. Gregory, Exploring the impact of pore size distribution on the performance of carbon electrodes for capacitive deionization, *J. Colloid Interface Sci.* 430 (2014) 93–99. <https://doi.org/10.1016/j.jcis.2014.05.015>.
- [116] X. Wen, D. Zhang, L. Shi, T. Yan, H. Wang, J. Zhang, Three-dimensional hierarchical porous carbon with a bimodal pore arrangement for capacitive deionization, *J. Mater. Chem.* 22 (2012) 23835. <https://doi.org/10.1039/c2jm35138b>.
- [117] H. Wang, D. Zhang, T. Yan, X. Wen, J. Zhang, L. Shi, Q. Zhong, Three-dimensional macroporous graphene architectures as high performance electrodes for capacitive deionization, *J. Mater. Chem. A.* 1 (2013) 11778. <https://doi.org/10.1039/c3ta11926b>.
- [118] I. Cohen, E. Avraham, Y. Bouhadana, A. Soffer, D. Aurbach, Long term stability of capacitive de-ionization processes for water desalination: The challenge of positive electrodes corrosion, *Electrochim. Acta.* 106 (2013) 91–100. <https://doi.org/10.1016/j.electacta.2013.05.029>.
- [119] R.L. Zornitta, P. Srimuk, J. Lee, B. Krüner, M. Aslan, L.A.M. Ruotolo, V. Presser, Charge and potential balancing for optimized capacitive deionization using lignin-derived, low-cost activated carbon electrodes, *ChemSusChem.* 11 (2018) 2101–2113. <https://doi.org/10.1002/cssc.201800689>.

- [120] Y. Bouhadana, E. Avraham, M. Noked, M. Ben-Tzion, A. Soffer, D. Aurbach, Capacitive Deionization of NaCl Solutions at Non-Steady-State Conditions: Inversion Functionality of the Carbon Electrodes, *J. Phys. Chem. C.* 115 (2011) 16567–16573. <https://doi.org/10.1021/jp2047486>.
- [121] I. Cohen, E. Avraham, Y. Bouhadana, A. Soffer, D. Aurbach, The effect of the flow-regime, reversal of polarization, and oxygen on the long term stability in capacitive de-ionization processes, *Electrochim. Acta.* 153 (2015) 106–114. <https://doi.org/10.1016/j.electacta.2014.12.007>.
- [122] F. Duan, X. Du, Y. Li, H. Cao, Y. Zhang, Desalination stability of capacitive deionization using ordered mesoporous carbon: Effect of oxygen-containing surface groups and pore properties, *Desalination.* 376 (2015) 17–24. <https://doi.org/10.1016/j.desal.2015.08.009>.
- [123] X. Gao, A. Omosibi, J. Landon, K. Liu, Dependence of the Capacitive Deionization Performance on Potential of Zero Charge Shifting of Carbon Xerogel Electrodes during Long-Term Operation, *J. Electrochem. Soc.* 161 (2014) E159–E166. <https://doi.org/10.1149/2.0561412jes>.
- [124] M. He, K. Fic, E. Frąckowiak, P. Novák, E.J. Berg, Ageing phenomena in high-voltage aqueous supercapacitors investigated by in situ gas analysis, *Energy Environ. Sci.* 9 (2016) 623–633. <https://doi.org/10.1039/C5EE02875B>.
- [125] K.C. Leonard, J.R. Genthe, J.L. Sanfilippo, W.A. Zeltner, M.A. Anderson, Synthesis and characterization of asymmetric electrochemical capacitive deionization materials using nanoporous silicon dioxide and magnesium doped aluminum oxide, *Electrochim. Acta.* 54 (2009) 5286–5291. <https://doi.org/10.1016/j.electacta.2009.01.082>.
- [126] W. Tang, D. He, C. Zhang, P. Kovalsky, T.D. Waite, Comparison of Faradaic reactions in capacitive deionization (CDI) and membrane capacitive deionization (MCDI) water treatment processes, *Water Res.* 120 (2017) 229–237. <https://doi.org/10.1016/j.watres.2017.05.009>.
- [127] V.B. Brião, J. Magoga, M. Hemkemeier, E.B. Brião, L. Girardelli, L. Sbeghen, D.P.C. Favaretto, Reverse osmosis for desalination of water from the Guarani Aquifer System to produce drinking water in southern Brazil, *Desalination.* 344 (2014) 402–411. <https://doi.org/10.1016/j.desal.2014.04.008>.

- [128] S. Foster, Groundwater and urban development in the 21st century – moving from piecemeal development to planned management in developing cities, in: *Solving Groundw. Challenges 21st Century*, CRC Press, 2016: pp. 23–40. <https://doi.org/10.1201/b20133-4>.
- [129] E. García-Quismondo, R. Gómez, F. Vaquero, A.L. Cudero, J. Palma, M. Anderson, New testing procedures of a capacitive deionization reactor, *Phys. Chem. Chem. Phys.* 15 (2013) 7648. <https://doi.org/10.1039/c3cp50514f>.
- [130] E. García-Quismondo, C. Santos, J. Lado, J. Palma, M.A. Anderson, Optimizing the Energy Efficiency of Capacitive Deionization Reactors Working under Real-World Conditions, *Environ. Sci. Technol.* 47 (2013) 11866–11872. <https://doi.org/10.1021/es4021603>.
- [131] Y. Liu, C. Nie, X. Liu, X. Xu, Z. Sun, L. Pan, Review on carbon-based composite materials for capacitive deionization, *RSC Adv.* 5 (2015) 15205–15225. <https://doi.org/10.1039/C4RA14447C>.
- [132] G. Rasines, P. Lavela, C. Macías, M.C. Zafra, J.L. Tirado, J.B. Parra, C.O. Ania, N-doped monolithic carbon aerogel electrodes with optimized features for the electrosorption of ions, *Carbon N. Y.* 83 (2015) 262–274. <https://doi.org/10.1016/j.carbon.2014.11.015>.
- [133] J.J. Wouters, M.I. Tejedor-Tejedor, J.J. Lado, R. Perez-Roa, M.A. Anderson, Influence of Metal Oxide Coatings, Carbon Materials and Potentials on Ion Removal in Capacitive Deionization, *J. Electrochem. Soc.* 165 (2018) E148–E161. <https://doi.org/10.1149/2.0271805jes>.
- [134] Y. Oren, Capacitive deionization (CDI) for desalination and water treatment - past, present and future (a review), *Desalination.* 228 (2008) 10–29. <https://doi.org/10.1016/j.desal.2007.08.005>.
- [135] J. Xie, Y. Xue, M. He, W. Luo, H. Wang, R. Wang, Y.-M. Yan, Organic-inorganic hybrid binder enhances capacitive deionization performance of activated-carbon electrode, *Carbon N. Y.* 123 (2017) 574–582. <https://doi.org/10.1016/j.carbon.2017.08.011>.
- [136] M. Liu, M. Xu, Y. Xue, W. Ni, S. Huo, L. Wu, Z. Yang, Y.-M. Yan, Efficient Capacitive Deionization Using Natural Basswood-Derived, Freestanding, Hierarchically Porous Carbon Electrodes, *ACS Appl. Mater. Interfaces.* 10 (2018) 31260–31270.

<https://doi.org/10.1021/acsami.8b08232>.

- [137] C. Santos, J.J. Lado, E. García-Quismondo, J. Soria, J. Palma, M.A. Anderson, Maximizing Volumetric Removal Capacity in Capacitive Deionization by Adjusting Electrode Thickness and Charging Mode, *J. Electrochem. Soc.* 165 (2018) E294–E302. <https://doi.org/10.1149/2.1011807jes>.
- [138] B. Cheng, R. Cheng, F. Tan, X. Liu, J. Huo, G. Yue, Highly Efficient Quasi-Solid-State Asymmetric Supercapacitors Based on MoS<sub>2</sub>/MWCNT and PANI/MWCNT Composite Electrodes, *Nanoscale Res. Lett.* 14 (2019) 66. <https://doi.org/10.1186/s11671-019-2902-5>.
- [139] N. Li, J. An, X. Wang, H. Wang, L. Lu, Z.J. Ren, Resin-enhanced rolling activated carbon electrode for efficient capacitive deionization, *Desalination.* 419 (2017) 20–28. <https://doi.org/10.1016/j.desal.2017.05.035>.
- [140] L. Wu, M. Liu, S. Huo, X. Zang, M. Xu, W. Ni, Z. Yang, Y.-M. Yan, Mold-casting prepared free-standing activated carbon electrodes for capacitive deionization, *Carbon N. Y.* 149 (2019) 627–636. <https://doi.org/10.1016/j.carbon.2019.04.102>.
- [141] L. Wang, M. Wang, Z.-H. Huang, T. Cui, X. Gui, F. Kang, K. Wang, D. Wu, Capacitive deionization of NaCl solutions using carbon nanotube sponge electrodes, *J. Mater. Chem.* 21 (2011) 18295. <https://doi.org/10.1039/c1jm13105b>.
- [142] J. Li, B. Ji, R. Jiang, P. Zhang, N. Chen, G. Zhang, L. Qu, Hierarchical hole-enhanced 3D graphene assembly for highly efficient capacitive deionization, *Carbon N. Y.* 129 (2018) 95–103. <https://doi.org/10.1016/j.carbon.2017.11.095>.
- [143] E.J. Jelmy, S. Ramakrishnan, S. Devanathan, M. Rangarajan, N.K. Kothurkar, Optimization of the conductivity and yield of chemically synthesized polyaniline using a design of experiments, *J. Appl. Polym. Sci.* 130 (2013) 1047–1057. <https://doi.org/10.1002/app.39268>.
- [144] K.K. Park, J.B. Lee, P.Y. Park, S.W. Yoon, J.S. Moon, H.M. Eum, C.W. Lee, Development of a carbon sheet electrode for electrosorption desalination, *Desalination.* 206 (2007) 86–91. <https://doi.org/10.1016/j.desal.2006.04.051>.
- [145] J.Y. Choi, J.H. Choi, A carbon electrode fabricated using a poly(vinylidene fluoride) binder controlled the Faradaic reaction of carbon powder, *J. Ind. Eng. Chem.* 16 (2010) 401–405.

<https://doi.org/10.1016/j.jiec.2009.08.005>.

- [146] M. Liu, C. Xiao, Research progress on modification of activated carbon, in: E3S Web Conf., Trans Tech Publ, 2018: pp. 780–784. <https://doi.org/10.1051/e3sconf/20183802005>.
- [147] J. Lee, K. Park, S. Yoon, P. Park, K. Park, C. Lee, Desalination performance of a carbon-based composite electrode, *Desalination*. 237 (2009) 155–161. <https://doi.org/10.1016/j.desal.2007.11.058>.
- [148] B.M. Asquith, J. Meier-Haack, B.P. Ladewig, Poly(arylene ether sulfone) copolymers as binders for capacitive deionization activated carbon electrodes, *Chem. Eng. Res. Des.* 104 (2015) 81–91. <https://doi.org/10.1016/j.cherd.2015.07.020>.
- [149] A. Kaynak, T. Mehmood, X. Dai, K. Magniez, A. Kouzani, Study of Radio Frequency Plasma Treatment of PVDF Film Using Ar, O<sub>2</sub> and (Ar + O<sub>2</sub>) Gases for Improved Polypyrrole Adhesion, *Materials (Basel)*. 6 (2013) 3482–3493. <https://doi.org/10.3390/ma6083482>.
- [150] T. Urai, M. Kamai, H. Fujii, Estimation of Intrinsic Contact Angle of Various Liquids on PTFE by Utilizing Ultrasonic Vibration, *J. Mater. Eng. Perform.* 25 (2016) 3384–3389. <https://doi.org/10.1007/s11665-016-2185-2>.
- [151] B. Jia, W. Zhang, Preparation and Application of Electrodes in Capacitive Deionization (CDI): a State-of-Art Review, *Nanoscale Res. Lett.* 11 (2016) 64. <https://doi.org/10.1186/s11671-016-1284-1>.
- [152] Z.H. Huang, Z. Yang, F. Kang, M. Inagaki, Carbon electrodes for capacitive deionization, *J. Mater. Chem. A*. 5 (2017) 470–496. <https://doi.org/10.1039/c6ta06733f>.
- [153] J. Oladunni, J.H. Zain, A. Hai, F. Banat, G. Bharath, E. Alhseinat, A comprehensive review on recently developed carbon based nanocomposites for capacitive deionization: From theory to practice, *Sep. Purif. Technol.* 207 (2018) 291–320. <https://doi.org/10.1016/j.seppur.2018.06.046>.
- [154] P. Ratajczak, M.E. Suss, F. Kaasik, F. Béguin, Carbon electrodes for capacitive technologies, *Energy Storage Mater.* 16 (2019) 126–145. <https://doi.org/10.1016/j.ensm.2018.04.031>.
- [155] M.S. Palagonia, C. Erinmwingbovo, D. Brogioli, F. La Mantia, Comparison between cyclic



voltammetry and differential charge plots from galvanostatic cycling, *J. Electroanal. Chem.* 847 (2019) 113170. <https://doi.org/10.1016/j.jelechem.2019.05.052>.

- [156] S. Zhao, T. Yan, H. Wang, G. Chen, L. Huang, J. Zhang, L. Shi, D. Zhang, High capacity and high rate capability of nitrogen-doped porous hollow carbon spheres for capacitive deionization, *Appl. Surf. Sci.* 369 (2016) 460–469. <https://doi.org/10.1016/j.apsusc.2016.02.085>.
- [157] A.J. Bard, L.R. Faulkner, *Electrochemical methods: fundamentals and applications*, 2nd ed., John Wiley & Sons Inc, New York, NY, 2001.
- [158] T. Kim, J. Yoon, Relationship between capacitance of activated carbon composite electrodes measured at a low electrolyte concentration and their desalination performance in capacitive deionization, *J. Electroanal. Chem.* 704 (2013) 169–174. <https://doi.org/10.1016/j.jelechem.2013.07.003>.
- [159] T.Y. Ying, K.L. Yang, S. Yiacoumi, C. Tsouris, Electrosorption of ions from aqueous solutions by nanostructured carbon aerogel, *J. Colloid Interface Sci.* 250 (2002) 18–27. <https://doi.org/10.1006/jcis.2002.8314>.
- [160] C.J. Gabelich, T.D. Tran, I.H. “Mel” Suffet, Electrosorption of Inorganic Salts from Aqueous Solution Using Carbon Aerogels, *Environ. Sci. Technol.* 36 (2002) 3010–3019. <https://doi.org/10.1021/es0112745>.
- [161] P.M. Biesheuvel, Thermodynamic cycle analysis for capacitive deionization, *J. Colloid Interface Sci.* 332 (2009) 258–264. <https://doi.org/10.1016/j.jcis.2008.12.018>.
- [162] D. He, C.E. Wong, W. Tang, P. Kovalsky, T.D. Waite, Faradaic Reactions in Water Desalination by Batch-Mode Capacitive Deionization, *Environ. Sci. Technol. Lett.* 3 (2016) 222–226. <https://doi.org/10.1021/acs.estlett.6b00124>.
- [163] T. Kim, J. Yoon, CDI ragone plot as a functional tool to evaluate desalination performance in capacitive deionization, *RSC Adv.* 5 (2015) 1456–1461. <https://doi.org/10.1039/C4RA11257A>.
- [164] Y. Cheng, Z. Hao, C. Hao, Y. Deng, X. Li, K. Li, Y. Zhao, A review of modification of carbon electrode material in capacitive deionization, *RSC Adv.* 9 (2019) 24401–24419.

<https://doi.org/10.1039/C9RA04426D>.

- [165] O. Sufiani, J. Elisadiki, R.L. Machunda, Y.A.C. Jande, Modification strategies to enhance electrosorption performance of activated carbon electrodes for capacitive deionization applications, *J. Electroanal. Chem.* 848 (2019) 113328. <https://doi.org/10.1016/j.jelechem.2019.113328>.
- [166] F. Yu, L. Wang, Y. Wang, X. Shen, Y. Cheng, J. Ma, Faradaic reactions in capacitive deionization for desalination and ion separation, *J. Mater. Chem. A* 7 (2019) 15999–16027. <https://doi.org/10.1039/C9TA01264H>.
- [167] A. Omosibi, X. Gao, J. Rentschler, J. Landon, K. Liu, Continuous operation of membrane capacitive deionization cells assembled with dissimilar potential of zero charge electrode pairs, *J. Colloid Interface Sci.* 446 (2015) 345–351. <https://doi.org/10.1016/j.jcis.2014.11.013>.
- [168] D. Lu, W. Cai, Y. Wang, Optimization of the voltage window for long-term capacitive deionization stability, *Desalination* 424 (2017) 53–61. <https://doi.org/10.1016/j.desal.2017.09.026>.
- [169] X. Gao, S. Porada, A. Omosibi, K.-L. Liu, P.M. Biesheuvel, J. Landon, Complementary surface charge for enhanced capacitive deionization, *Water Res.* 92 (2016) 275–282. <https://doi.org/10.1016/j.watres.2016.01.048>.
- [170] A.C. Arulrajan, D.L. Ramasamy, M. Sillanpää, A. van der Wal, P.M. Biesheuvel, S. Porada, J.E. Dykstra, Exceptional Water Desalination Performance with Anion-Selective Electrodes, *Adv. Mater.* 31 (2019) 1806937. <https://doi.org/10.1002/adma.201806937>.
- [171] K. Xu, S.P. Ding, T.R. Jow, Toward Reliable Values of Electrochemical Stability Limits for Electrolytes, *J. Electrochem. Soc.* 146 (1999) 4172–4178. <https://doi.org/10.1149/1.1392609>.
- [172] A. John, P.J.P. Yadav, S. Palaniappan, Clean synthesis of 1,8-dioxo-dodecahydroxanthene derivatives catalyzed by polyaniline-p-toluenesulfonate salt in aqueous media, *J. Mol. Catal. A Chem.* 248 (2006) 121–125. <https://doi.org/10.1016/j.molcata.2005.12.017>.
- [173] G.D. Vuković, A.D. Marinković, M. Čolić, M.Đ. Ristić, R. Aleksić, A.A. Perić-Grujić, P.S. Uskoković, Removal of cadmium from aqueous solutions by oxidized and ethylenediamine-functionalized multi-walled carbon nanotubes, *Chem. Eng. J.* 157 (2010) 238–248.

<https://doi.org/10.1016/j.cej.2009.11.026>.

- [174] B. Pillay, J. Newman, The Influence of Side Reactions on the Performance of Electrochemical Double-Layer Capacitors, *J. Electrochem. Soc.* 143 (1996) 1806–1814. <https://doi.org/10.1149/1.1836908>.
- [175] X. Xu, H. Tang, M. Wang, Y. Liu, Y. Li, T. Lu, L. Pan, Carbon spheres with hierarchical micro/mesopores for water desalination by capacitive deionization, *J. Mater. Chem. A* 4 (2016) 16094–16100. <https://doi.org/10.1039/C6TA07616E>.
- [176] J. Yu, K. Jo, T. Kim, J. Lee, J. Yoon, Temporal and spatial distribution of pH in flow-mode capacitive deionization and membrane capacitive deionization, *Desalination* 439 (2018) 188–195. <https://doi.org/10.1016/j.desal.2018.04.011>.
- [177] D. Ma, Y. Wang, X. Han, S. Xu, J. Wang, Electrode configuration optimization of capacitive deionization cells based on zero charge potential of the electrodes, *Sep. Purif. Technol.* 189 (2017) 467–474. <https://doi.org/10.1016/j.seppur.2017.08.025>.
- [178] A.G. El-Deen, R.M. Boom, H.Y. Kim, H. Duan, M.B. Chan-Park, J.-H. Choi, Flexible 3D Nanoporous Graphene for Desalination and Bio-decontamination of Brackish Water via Asymmetric Capacitive Deionization, *ACS Appl. Mater. Interfaces* 8 (2016) 25313–25325. <https://doi.org/10.1021/acsami.6b08658>.
- [179] O. ul Haq, D.-S. Choi, J.-H. Choi, Y.-S. Lee, Carbon electrodes with ionic functional groups for enhanced capacitive deionization performance, *J. Ind. Eng. Chem.* 83 (2020) 136–144. <https://doi.org/10.1016/j.jiec.2019.11.021>.
- [180] X. Gao, A. Omosebi, N. Holubowitch, A. Liu, K. Ruh, J. Landon, K. Liu, Polymer-coated composite anodes for efficient and stable capacitive deionization, *Desalination* 399 (2016) 16–20. <https://doi.org/10.1016/j.desal.2016.08.006>.
- [181] J.S. Kang, S. Kim, D.Y. Chung, Y.J. Son, K. Jo, X. Su, M.J. Lee, H. Joo, T.A. Hatton, J. Yoon, Y. Sung, Rapid Inversion of Surface Charges in Heteroatom-Doped Porous Carbon: A Route to Robust Electrochemical Desalination, *Adv. Funct. Mater.* 30 (2020) 1909387. <https://doi.org/10.1002/adfm.201909387>.
- [182] Y. Li, Z. Ding, J. Li, J. Li, T. Lu, L. Pan, Highly efficient and stable desalination via novel

hybrid capacitive deionization with redox-active polyimide cathode, *Desalination*. 469 (2019) 114098. <https://doi.org/10.1016/j.desal.2019.114098>.

- [183] B. Shapira, E. Avraham, D. Aurbach, Side Reactions in Capacitive Deionization (CDI) Processes: The Role of Oxygen Reduction, *Electrochim. Acta*. 220 (2016) 285–295. <https://doi.org/10.1016/j.electacta.2016.10.127>.
- [184] D. Li, X. Ning, Y. Huang, S. Li, Nitrogen-rich microporous carbon materials for high-performance membrane capacitive deionization, *Electrochim. Acta*. 312 (2019) 251–262. <https://doi.org/10.1016/j.electacta.2019.04.172>.
- [185] W. Shi, C. Ye, X. Xu, X. Liu, M. Ding, W. Liu, X. Cao, J. Shen, H.Y. Yang, C. Gao, High-Performance Membrane Capacitive Deionization Based on Metal–Organic Framework-Derived Hierarchical Carbon Structures, *ACS Omega*. 3 (2018) 8506–8513. <https://doi.org/10.1021/acsomega.8b01356>.
- [186] Y. Li, X. Xu, S. Hou, J. Ma, T. Lu, J. Wang, Y. Yao, L. Pan, Facile dual doping strategy via carbonization of covalent organic frameworks to prepare hierarchically porous carbon spheres for membrane capacitive deionization, *Chem. Commun.* 54 (2018) 14009–14012. <https://doi.org/10.1039/C8CC06855K>.
- [187] P. Shi, C. Wang, J. Sun, P. Lin, X. Xu, T. Yang, Thermal conversion of polypyrrole nanotubes to nitrogen-doped carbon nanotubes for efficient water desalination using membrane capacitive deionization, *Sep. Purif. Technol.* 235 (2020) 116196. <https://doi.org/10.1016/j.seppur.2019.116196>.
- [188] P. Shi, C. Wang, J. Sun, P. Lin, X. Xu, T. Yang, Thermal conversion of polypyrrole nanotubes to nitrogen-doped carbon nanotubes for efficient water desalination using membrane capacitive deionization, *Sep. Purif. Technol.* 235 (2020) 116196. <https://doi.org/10.1016/j.seppur.2019.116196>.